Fakultät für Maschinenwesen
Lehrstuhl für Carbon Composites

Characterisation and simulation of adhesively bonded joints with laminated adherends for crash applications

Johannes Sebastian Neumayer

Vollständiger Abdruck der von der Fakultät für Maschinenwesen der Technischen Universität München zur Erlangung des akademischen Grades eines

Doktor-Ingenieurs (Dr.-Ing.)

genehmigten Dissertation.

Vorsitzender:	Prof. Dr.-Ing. Markus Lienkamp
Prüfer der Dissertation:	Prof. Dr.-Ing. Klaus Drechsler
	Assoc. Prof. Dr. Albert Turon Travesa (University of Girona)

Die Dissertation wurde am 12.10.2016 bei der Technischen Universität München eingereicht und durch die Fakultät für Maschinenwesen am 24.04.2017 angenommen.

Dedicated to my parents.

Acknowledgement

The following thesis would not have been possible without the help of many people. I would like to thank the Institute of Carbon Composites chaired by Prof. Drechsler and the administrative staff, who provided the position to work in this highly interesting research field and providing a pleasant and positive working environment. The funding of most parts of this work shall be mentioned at this point by the German Federal Ministry of Education and Research under the project "Hybrid-Fügetechnologien für Leichtbauweisen bei Transportanwendungen (TransHybrid)" (Nr. 13N11993). Moreover, I would like to thank the Volkswagen AG for providing the experimental results of the T-joint substructure.

I would like to say special thanks to Dr. tech. Roland Hinterhölzl and Dr. Hannes Körber for the supervision of my work. They helped me to find a good start and gave inspiring ideas at important points of this thesis. I would like to thank my colleagues of the team "Material Modeling and Structural Analysis" for the fruitful discussions. This is namely Dr. Jörg Cichosz, Philipp Fahr, Ulrich Mandel, Natalie Mayer, Robin Taubert and Tobias Wehrkamp-Richter. Luciano Avila-Gray, Peter Kuhn and Marina Plöckl helped with their experience in the design and set-up of the experiments.

Special thanks belong to Prof. Lucas F.M. daSilva. He gave me the opportunity to discuss parts of my work with colleagues and other researchers in the field at the Chair for Adhesive Bonding at the University of Porto. In this context, I would like to thank the TUM Graduate school for the financial support staying abroad.

Finally, I would like to thank my wife for her patience and supporting me in my work and during the time of writing.

Abstract

The successful application of fibre reinforced plastics in load bearing structures depends on the weight saving and on the reliability during the lifetime of the products. An adequate joining technique for fibre reinforced parts is crucial to enable both aspects. Adhesive joining can play a key role due to many advantages. High confidence in the joining technique is, however, still necessary. This confidence can be gained by an increase of the knowledge about adhesively bonded joints, but it also needs time and successful applications. The later can be guaranteed by a robust design process, a repeatable manufacturing process, high quality assurance and a reliable service inspection.

In this thesis, the design and verification of bonded joints with fibre reinforced adherends by finite element crash simulations is addressed. The challenges lie in the accurate and efficient modelling of the joints. This is a current issue in the automotive industry, where crash scenarios are most relevant for the design process. But also in the aviation industry or wind craft industry standardised crash scenarios like bird strike or drop tests exist.

The prediction of the strength of the bonded joints is the most critical aspect. Hereby, the failure modes play an important role. They can be divided into a cohesive failure of the adhesive and a failure of the adherend. The failure of the adhesive-adherend-interface is not investigated. In this thesis, an approach is presented to model the adhesive by a mixed-mode rate-dependent cohesive behaviour. This is calibrated and validated by quasi-static experiments and high-rate experiments on a tensile split-Hopkinson bar test set-up. Moreover, a T-joint substructure is taken for the validation of a three-dimensional simulation showing cohesive failure of the adhesive. To efficiently model the adherend failure with acceptable accuracy, a new cohesive zone approach is presented in this thesis. The delamination failure is integrated into the cohesive zone by an adaptation of the cohesive law during the simulation. This approach makes it possible to represent the fibre reinforced adherends by shell structures and the adhesive bondline with only one cohesive zone over the complete thickness.

A progress has been achieved through this work in the field of high-rate characterisation of adhesives, rate-dependent modelling of cohesive failure and efficient modelling of delamination failure. The methods were developed for usage by original equipment manufacturers as well as engineering service providers. Using these methods can contribute to a reliable design of bonded joints with fibre reinforced laminated adherends and enable weight savings in modern engineering structures.

Kurzfassung

Der erfolgreiche Einsatz von Faserverbundwerkstoffen in lasttragenden Strukturen hängt von der Gewichtsersparnis sowie der Verlässlichkeit in der Produktnutzungsphase ab. Eine materialgerechte Verbindungstechnik für faserverstärkte Bauteile ist essentiell für beide Aspekte. Wegen zahlreicher Vorteile spielt die Klebetechnik eine wichtige Rolle. Großes Vertauen in die Klebtechnik ist jedoch immer noch erforderlich. Dieses Vertrauen kann durch Wissensfortschritte gewonnen werden, aber auch Zeit und erfolgreiche Anwendungen sind notwendig. Letzteres kann durch einen robusten Auslegungsprozess, einen reproduzierbaren Herstellungsprozess, eine gute Qualitätskontrolle sowie eine verlässliche Serviceinspektion garantiert werden.

In dieser Arbeit wird die Auslegung und Nachweisführung von Klebeverbindungen mit faserverstärktern Fügepartnern in Finite Elemente Crash Simulationen adressiert. Die Herausforderungen liegen in der genauen und effizienten Modellierung. Dies ist ein gegenwärtiges Thema in der Automobilindustrie, wo Crashszenarien große Relevanz im Auslegungsprozess besitzen. Aber auch in der Luftfahrt oder bei Windkraftanlagen existieren standardisierte Crashszenarien wie Vogelschlag oder Falltests.

Die Festigkeit von Klebeverbindungen vorherzusagen ist der wichtigste Aspekt. Dabei spielen die Versagensarten eine wichtige Rolle. Diese können in ein kohäsives Versagen der Klebschicht und ein Versagen im Fügepartner eingeteilt werden. Das Versagen der Fügepartner-Klebschicht-Grenzfläche wird nicht betrachtet. In dieser Arbeit wird ein Ansatz präsentiert in dem die Klebschicht durch ein ratenabhängiges Mixed-Modus-Kohäsivzonenverhalten modelliert wird. Dieses wird durch quasistatische Versuche und hochdynamische Versuche an einer Zug-Split-Hopkinson-Bar Vorrichtung kalibriert und validiert. Außerdem wird eine T-Stoß-Substruktur verwendet, um eine dreidimensionale Simulation des kohäsiven Klebschichtversagens zu validieren. Um effizient das Versagen im Fügepartner mit akzeptabler Genauigkeit zu modellieren, wird in dieser Arbeit ein neuer Kohäsivzonenansatz vorgestellt. Das Delaminationsversagen wird dabei in die Kohäsivzone durch eine Anpassung des Kohäsivzonengesetzes während der Simulation integriert. Dieser Ansatz ermöglicht es, die Fügepartner über Schalenstrukturen und die Klebschicht mit nur einer Schicht Kohäsivzonenelemente über die gesamte Dicke darzustellen.

Auf dem Gebiet der hochdynamischen Charakterisierung von Klebschichten, der ratenabhängigen Modellierung des kohäsiven Klebschichtversagens und der effizienten Modellierung von Delaminationsversagen wurde durch diese Arbeit ein Fortschritt erreicht. Die Methoden wurden für den Einsatz bei Herstellern der Originalausstattung sowie bei Ingenieursdientleistern entwickelt. Die Anwendung dieser Methoden

kann zu einer zuverlässigen Auslegung von Klebeverbindung mit faserverstärkten laminierten Fügepartnern beitragen und Gewichtseinsparungen in modernen Strukturbauteilen ermöglichen.

Contents

Nomenclature **xi**

Abbreviations **xv**

List of Figures **xvii**

List of Tables **xxiii**

1 Introduction **1**

1.1 Objectives of the thesis 3

1.2 Structure of the thesis 4

2 Theory and state-of-the-art **7**

2.1 Adhesive bonding 7

2.1.1 Adhesion and cohesion 7

2.1.2 Mechanical behaviour of bonded FRP structures 8

2.2 Theory of cohesive zone modelling 11

2.2.1 Basics of the dynamic Finite Element Method (FEM) 11

2.2.2 Cohesive zone modelling (CZM) 14

2.2.3 Cohesive laws for the simulation of the cohesive behaviour of adhesives 16

2.3 Testing of adhesive joints 19

2.3.1 Adhesive testing for cohesive laws 19

2.3.2 Test methods for high-rate testing 21

2.3.3 Theory of split-Hopkinson Bar (SHB) testing 23

2.3.4 SHB testing of adhesive joints 25

2.4 Summary of the chapter 26

3 Characterisation of the adhesive **29**

3.1 Quasi-static testing of the adhesive with butt joint and lap shear tests 30

3.1.1 Specimen manufacturing and testing 30

3.1.2 Results and discussion 31

3.2 Quasi-static testing of the adhesive by the DCB test 34

3.2.1 Specimen manufacturing and testing 35

3.2.2 Results and discussion 36

3.3 Quasi-static testing of the adhesive by the ENF test 39

3.3.1 Specimen manufacturing and testing 39

3.3.2 Results and discussion 40

3.4 Testing of the adhesive under combined loading 42

3.4.1 Specimen manufacturing and testing 42

3.4.2 Results and discussion 43
3.5 Intermediate-rate testing of the adhesive with butt joint tests 45
3.6 High-rate testing of the adhesive with butt joint and lap shear specimen 46
3.6.1 Specimen manufacturing and testing 47
3.6.2 Results and discussion 49
3.7 Summary of the chapter 52

4 Characterisation of the adherends 55
4.1 Characterisation of the FRP adherend 55
4.2 Characterisation of the aluminium adherend 57
4.2.1 Quasi-static testing of the aluminium 57
4.2.2 High-rate testing of the aluminium 59
4.3 Summary of the chapter 60

5 Simulation of cohesive failure in bonded joints 63
5.1 Modelling of the adhesive 63
5.1.1 Mixed-mode rate-dependent cohesive law 63
5.1.2 Calibration of the cohesive law 67
5.2 Testing and simulation of a single lap joint (SLJ) 71
5.2.1 Specimen manufacturing and testing 71
5.2.2 Numerical evaluation 76
5.2.3 Results 78
5.2.4 Discussion 82
5.3 Testing and simulation of a T-joint sub-component 88
5.3.1 Specimen geometry and testing 88
5.3.2 Numerical evaluation 89
5.3.3 Results 91
5.3.4 Discussion 93
5.4 Summary of the chapter 95

6 Simulation of delamination failure in bonded joints 99
6.1 Element formulation 101
6.2 Numerical evaluation 107
6.2.1 Numerical model 107
6.2.2 Results and discussion 109
6.3 Summary of the Chapter 114

7 Conclusion and outlook 117
7.1 Characterisation of the adhesive 117
7.2 Simulation of cohesive failure in composite bonded joints 118
7.3 Simulation of delamination failure in composite bonded joints . . . 119

Bibliography **121**

A Publications **133**

B Supervised student theses **135**

Nomenclature

Mathematical notation, domains, general indices and operators

a	Scalar value
$\boldsymbol{a}$	Vector variable
$\boldsymbol{A}$	Matrix or tensor variable
$\dot{\boldsymbol{u}}$	First derivative towards time
$\ddot{\boldsymbol{u}}$	Second derivative towards time
Ω	Arbitrary body
Γ_c	Crack surface
Γ_τ	Traction boundary
Γ_u	Displacement boundary
$(\cdot)^*$	Estimated value
$(\cdot)^0$	Allowable value/ strength
$(\cdot)^k$	Index of k-th separation rate
$(\cdot)^T$	Transpose of a vector or matrix/tensor
$(\cdot)^{(el)}$	Element property
$(\cdot)^\pm$	±-side of the crack
$(\cdot)_0$	Initial value
$(\cdot)_b$	Bar property of a split-Hopkinson bar
$(\cdot)_p$	Index for ply numbering in a laminate
$(\cdot)_{1,2,u}$	Index for the onset of degradation, onset of softening and ultimate value of the cohesive law
$(\cdot)_{del}$	Delamination property
$(\cdot)_{I,II,III}$	Mode I, II and III
$(\cdot)_{inc,ref,tra}$	Incident, reflected and transmitted signal of a split-Hopkinson bar
$(\cdot)_{N,S,m}$	Normal, shear and mixed-mode direction
$(\cdot)_{nom,true}$	Nominal and true quantity
$(\cdot)_{spe}$	Specimen property
$\frac{d(\cdot)}{dt}$	Derivation towards time
$\hat{(\cdot)}$	Prescribed boundary value
$\delta(\cdot)$	Virtual quantity
$\frac{\partial(\cdot)}{\partial x}$	Partial derivation towards the coordinate x
$div(\cdot)$	Divergence operator

Scalars

α	Exponent for rate-dependent logarithmic interpolation
A	Area
a,b,d	Inverse stiffness matrix components of a composite beam

β	Mixed-mode ratio
χ	Transverse shear stiffness factor
c	Wave speed
Δ	Bondline deformation
δ	Scalar separation value
d	Degradation
ϵ	Scalar strain value
E	Young's modulus
E_a	Apparent Young's modulus
ϵ^0	membrane strain of composite beam
ϵ_F	Strain of the spew fillet
F	Force
γ	Shear strain
G	Shear modulus
h	Height of the adherend
$\mathbb{J}$	J-integral
J	Energy released
J_c	Fracture energy
κ	Curvature
Δl	Distance
l	Length
l_{el}	Characteristic element length
μ	Exponent of mixed-mode interaction of the cohesive law
m	Moment load per width
ν	Poisson ratio
n	Normal load per width
q	Shear load per width
ρ	Mass density
σ	Scalar stress value
Δt	Time-step
θ_{ld}	Rotation of the load introduction point
$\theta_{sup1}, \theta_{sup2}$	Rotation of the points at support 1 and 2
t	Time
T_{coh}	Cohesive or bondline thickness
Δt_{crit}	Critical time-step
T_F	Thickness of the spew fillet
u	Deformation
$\dot{u}$	Particle velocity

V_0	Striker bar velocity
w	Width
η, ξ	Curvilinear coordinates on the crack interface

Vectors

$\boldsymbol{b}$	Body force vector
$\boldsymbol{d}$	Global displacement vector
$\boldsymbol{\delta}$	Local displacement jump/ separation vector
$\boldsymbol{f_{ext}}$	Global external force vector
$\boldsymbol{f_{int}}$	Global internal force vector
$\boldsymbol{n}$	Surface normal vector
$\boldsymbol{\tau}$	Traction vector
$\bar{\boldsymbol{\tau}}$	Global traction vector at the interface
$\boldsymbol{u}$	Displacement vector
$[\![\boldsymbol{u}]\!]$	Global displacement jump vector
$\boldsymbol{v}$	Vector on the crack interface
$\boldsymbol{v}_n$, $\boldsymbol{v}_s$, $\boldsymbol{v}_t$	Orthonormal basis on the crack interface
$\boldsymbol{x}$	Coordinates of a local point
$\bar{\boldsymbol{x}}$	Coordinates of the crack interface.

Tensors, matrices

$\mathbb{C}$	Forth-order stiffness tensor
$\boldsymbol{\epsilon}$	Strain tensor
$\boldsymbol{L}$	Spatial derivatives matrix
$\boldsymbol{M}$	Global mass matrix
$\boldsymbol{N}$	Shape function matrix
$\boldsymbol{\sigma}$	Cauchy stress tensor
$\boldsymbol{S}$	Stiffness matrix for local displacement jump/ cohesive law
$\boldsymbol{\Theta}$	Mapping operator matrix
$\boldsymbol{\Xi}$	Metric matrix

Abbreviations

1D One-dimensional

2D Two-dimensional

3D Three-dimensional

CFRP Carbon fibre reinforced plastic

CZ Cohesive zone

CZM Cohesive zone modelling

DCB Double cantilever beam

DIC Digital image correlation

DOF Degree of freedom

ENF End-notched flexural

FE Finite element

FEM Finite Element Method

fps Frames per second

FRP Fibre reinforced plastic

ILSS Interlaminar shear strength

ILTS Interlaminar tensile strength

SHB Split-Hopkinson bar

SHBA Split-Hopkinson bar analysis

SLJ Single lap joint

TAST Thick adherend shear test

UD Unidirectional

VUEL Vector explicit user element

VUMAT Vector explicit user material

List of Figures

1-1 Global demand on carbon fibres. 2

1-2 Influence of delamination failure on the mechanical behaviour of a bonded joint. 4

2-1 Adhesion and cohesion. 8

2-2 Failure modes of a bonded joint with FRP adherends. 9

2-3 Failure modes for delamination failure. 10

2-4 Arbitrary body Ω with displacement and traction boundary conditions. 12

2-5 Dynamic structural boundary value problem with a crack. 14

2-6 Triangular, non-linear and trapezoidal cohesive law. 17

2-7 Different formulations for a trapezoidal cohesive law: reversible (left), elastic-degradation (middle) and elastic-plastic-degration (right). . . 17

2-8 Classical compression SHB set-up. 23

3-1 Specimen geometry of the butt joint (left) and the lap shear specimen (right). 30

3-2 Representative specimen for the butt joint test (left) and the lap shear test (right). 31

3-3 Quasi-static test set-up with a butt joint specimen. 32

3-4 Stress-deformation curves of the butt joint test at quasi-static loading ($3.0 \mu m/s$). 32

3-5 Stress-deformation curves of the lap shear test at quasi-static loading ($3.0 \mu m/s$). 33

3-6 Fracture surface of a representative butt joint specimen. 33

3-7 Fracture surface of a representative lap shear specimen. 34

3-8 DCB specimen geometry. 35

3-9 Application of adhesive (left) and shims to guarantee the adhesive thickness (right). 36

3-10 Representative DCB specimen. 36

3-11 Testing of a DCB specimen in the electromechanical testing machine (left) and DIC post-processing (right). 36

3-12 Cohesive law of the adhesive in mode I at a deformation rate of $1.0 \mu m/s$. 37

3-13 Fracture surface of a DCB specimen. 37

3-14 Comparison between the curves from the butt joint tests (BJ) at a deformation rate of $3.0 \mu m/s$ and the spline fitted DCB tests (DCBf) at a deformation rate of $1.0 \mu m/s$. 38

3-15 Comparison of secant stiffness, maximum stress and energy absorbed per bonding area between quasi-static butt joint tests (BJ) and raw and spline fitted DCB tests (DCB/ DCBf). 38
3-16 Geometry of an ENF specimen. 39
3-17 Representative ENF specimen. 40
3-18 Testing of an ENF specimen in the electromechanical testing machine (left) and DIC post-processing (right). 40
3-19 Cohesive law of the adhesive in mode II at a deformation rate of $3.0 \mu m/s$. 41
3-20 Fracture surface of an ENF specimen. 41
3-21 Comparison between the curves from the lap shear tests (LS) and the spline fitted ENF tests (ENFf) at a deformation rate of $3.0 \mu m/s$. 41
3-22 Comparison of secant stiffness, maximum stress and energy absorbed per bonding area between quasi-static lap shear tests (LS) and raw and spline fitted ENF tests (ENF/ ENFf). 42
3-23 Geometry of the combined loading specimen. 42
3-24 Representative specimen of the combined loading test. 43
3-25 Stress-deformation curves of the combined loading tests at a deformation rate of $1.0 \mu m/s$. 44
3-26 Crack surface of the combined loading specimen. 44
3-27 Comparison of secant stiffness, maximum stress and energy absorbed per bonding area between quasi-static butt joint (BJ), scarf joint (SJ) and lap shear (LS) specimen. 45
3-28 Stress-deformation curves of the butt joint tests at intermediate-rate loading ($0.2 mm/s$). 46
3-29 Comparison of secant stiffness, maximum stress and energy absorbed per bonding area between quasi-static (QS) and intermediate-rate (IR) butt joint tests. 46
3-30 Set-up of the tensile SHB system. 48
3-31 DIC measurement of adhesive deformation: butt joint test (left) and lap shear test (right). 48
3-32 Bar strain gauge signals (raw): butt joint test (left) and lap shear test (right). 48
3-33 Filtered and shifted bar strain gauge signals: butt joint test (left) and lap shear test (right). 49
3-34 Force signals: butt joint test (left) and lap shear test (right). 49
3-35 Speckle pattern and DIC deformation field of a butt joint specimen (left) and a lap shear specimen (right). 49
3-36 Deformation measurement based on SHBA and DIC: butt joint test (left) and lap shear test (right). 50

3-37 Stress-deformation curves of the butt joint test at high-rate loading ($1.0m/s$). 50
3-38 Stress-deformation curves of the lap shear test at high-rate loading ($3.0m/s$). 50
3-39 Comparison of secant stiffness, maximum stress and energy absorbed per bonding area between quasi-static (QS), intermediate-rate (IR) and high-rate butt joint tests using DIC (HR) and SHBA (HR*). . . 51
3-40 Comparison of secant stiffness, maximum stress and energy absorbed per bonding area between quasi-static (QS) and high-rate lap shear tests using DIC (HR) and SHBA (HR*). 52

4-1 Geometry of the aluminium specimen (left) and a representative specimen (right). 57
4-2 Nominal strain in x-direction of a representative aluminium specimen. 58
4-3 True stress-strain curves of the aluminium sheet at a strain rate of $0.001s^{-1}$. 58
4-4 Filtered and shifted strain signals (left) and force signals (right). . . 59
4-5 Stress-strain curve of a representative aluminium high-rate test (left) and strain rate signals based on SHBA and DIC (right). 60
4-6 Stress-strain curves the aluminium high-rate tests at a strain rate of $800s^{-1}$. 60

5-1 Trapezoidal cohesive law. 63
5-2 Trapezoidal cohesive law in normal direction (left) and in shear direction (right) for a deformation rate of $\dot{\delta} = 3\mu m/s$. 68
5-3 Trapezoidal cohesive law in normal direction (left) and in shear direction (right) for a deformation rate of $\dot{\delta} = 3m/s$. 68
5-4 Mixed-mode behaviour of the cohesive law for $\dot{\delta} = 3\mu m/s$ (left) and $\dot{\delta} = 3m/s$ (right) for various loading ratios ϕ. 69
5-5 Comparison of the cohesive law at $\phi = 15°$ for $\dot{\delta} = 3\mu m/s$ with the experimental results of the scarf joint tests. 69
5-6 Cohesive laws in mode N for linear ($\alpha = 1$) and quadratic ($\alpha = 2$) logarithmic interpolation of the tractions compared to the butt joint experiments at the deformation rate $\dot{\delta} = 0.2mm/s$. 70
5-7 Cohesive laws for quadratic interpolation ($\alpha = 2$) in normal direction (left) and shear direction (right) for various deformation rates $\dot{\delta} = 3.0 \cdot 10^i \mu m/s$. 70
5-8 Specimen geometry of the CFRP-CFRP SLJ (left) and the CFRP-aluminium SLJ (right). 71
5-9 Sketch of the custom made fixture for curing the SLJ specimen with a constant bondline thickness. 72

5-10 Representative CFRP-CFRP (top) and CFRP-aluminium (bottom) SLJ specimen for quasi-static testing. 72
5-11 Set-up of the quasi-static testing of a SLJ. 73
5-12 Side view of the broken CFRP-CFRP SLJ specimen (left) and fracture surfaces (middle and right). 73
5-13 Side view of the broken CFRP-aluminium SLJ specimen (left) and fracture surfaces (middle and right). 73
5-14 Filtered and shifted strain gauge signals (left) and force signals (right) of an high-rate CFRP-CFRP SLJ. 74
5-15 Side view of an CFRP-aluminium SLJ initially (top) and at the time of failure (bottom) for a CFRP-aluminium SLJ. 75
5-16 Force-displacement curve (left) and displacement rate signals (right) of a representative CFRP-CFRP SLJ comparing SHBA and DIC. . 75
5-17 Fracture surfaces of a CFRP-CFRP SLJ. 75
5-18 Fracture surfaces of a CFRP-aluminium SLJ. 76
5-19 Geometry and mesh of the CFRP-CFRP SLJ (top) and the CFRP-aluminium SLJ (bottom). 76
5-20 Definition of the quasi-static aluminium properties in the simulation compared to the experiments at a strain rate of $0.001s^{-1}$. 77
5-21 Definition of the high-rate aluminium properties in the simulation compared to the experiments at a strain rate of $800s^{-1}$. 77
5-22 Force-displacement curve of the quasi-static experiments of the CFRP-CFRP SLJ (left) and the CFRP-aluminium SLJ (right) at a loading rate of $1.5\mu m/s$. 78
5-23 Force-displacement curve of the high-rate experiments of the CFRP-CFRP SLJ (left) and the CFRP-aluminium SLJ (right) at a loading rate of $2.0m/s$. 79
5-24 Stress distribution in the high-rate CFRP-CFRP SLJ at the maximum loading. 80
5-25 Stress distribution in the high-rate CFRP-aluminium SLJ at the maximum loading. 81
5-26 Force-displacement curve of the SLJ tests with varying the boundary conditions for the quasi-static CFRP-CFRP SLJ ($1.5\mu m/s$). 82
5-27 Force-displacement curve of CFRP-aluminium SLJ tests with purely elastic modelling of the aluminium material in the quasi-static case at $1.5\mu m/s$ (left) and the high-rate case at $2.0m/s$ (right). 83
5-28 Comparison between the simulation of the CFRP-CFRP SLJ and the corresponding experiments that have low amount of voids at the quasi-static loading rate ($1.5\mu m/s$). 84

5-29 Comparison of the maximum forces of the simulation with experiments in the quasi-static case (left) and the high-rate case (right). . 84

5-30 Sensitivity of the simulation on the cohesive law properties at the quasi-static loading rate ($1.5\mu m/s$): Ultimate traction τ_u (left) and J_c (right). 85

5-31 Variation of the mixed-mode exponent μ and experimental results of the combined loading test. 86

5-32 Simulation of the CFRP-CFRP SLJ (left) and the CFRP-aluminium SLJ (right) with mixed-mode exponent $\mu = 2.0$ and $\mu = 1.4$ compared to experiments at the quasi-static loading rate ($1.5\mu m/s$) . . . 86

5-33 Simulation of the CFRP-CFRP SLJ (left) and the CFRP-aluminium SLJ (right) with mixed-mode exponent $\mu = 2.0$ and $\mu = 1.4$ compared to experiments at the high-rate loading ($2.0m/s$) 86

5-34 Assembly of the T-joint subcomponent. 88

5-35 Modelling of the spew fillets and the adhesive bondlines. 90

5-36 Mesh of the adhesive bondline. 91

5-37 Mesh and boundary conditions of the T-joint model. 92

5-38 Force-displacement curve of the T-joint experiments and simulation for quasi-static loading ($10mm/min$). 93

5-39 Force-rotation curve of the T-joint experiments and simulation for dynamic loading ($1.2m/s$). 93

5-40 Influence of the aluminium material properties on the simulation of the T-joint for the quasi-static loading rate of $10mm/min$ (left) and the high-rate loading of $1.2m/s$ (right). 94

5-41 Influence of the ultimate traction of the cohesive law on the simulation results of the T-joint for the quasi-static loading rate of $10mm/min$ (left) and the high-rate loading of $1.2m/s$ (right). . . . 94

5-42 Influence of the fracture energy on the simulation results of the T-joint for the quasi-static loading rate of $10mm/min$ (left) and the high-rate loading of $1.2m/s$ (right). 94

5-43 Influence of the spew fillet on the simulation results of the T-joint for the quasi-static loading rate of $10mm/min$ (left) and the high-rate loading of $1.2m/s$ (right). 95

5-44 Influence of the loading amplitude on the simulation results of the T-joint for the high-rate loading of $1.2m/s$. 96

6-1 a) Conventional CZ model: The adherend is modelled by continuum elements with optional delamination interfaces for the simulation of dynamic crack growth in the adherend; b) Model reduction with one CZ over the complete adhesive thickness including delamination failure. 101
6-2 Degrees of freedom for the cohesive element. 102
6-3 Infinitesimal section of the laminated beam subjected to surface tractions. 103
6-4 Solution process of the boundary value problem with the new CZ approach. 106
6-5 Geometry of the numerical model. 107
6-6 Mesh of the detailed model at the right edge of the overlap. 107
6-7 Mesh of the reduced model at the right edge of the overlap. 108
6-8 Cohesive law of the adhesive in normal and shear direction. 108
6-9 Force-displacement curve using the "DelStrong" delamination properties. 109
6-10 Location of delamination initiation in the detailed model. 109
6-11 Force-displacement curve using the "DelWeak" delamination properties. 110
6-12 Tensile stresses in x_2-direction at the overlap edge at a load level of $3.21kN$ and position of the through thickness stress evaluation (white line). 110
6-13 Comparison of the through thickness shear stresses for a joint load of $3.21kN$. 111
6-14 Comparison of the through thickness tensile stresses for a joint load of $3.21kN$. 111
6-15 Convergence study of the reduced model. 112
6-16 Convergence study of the detailed model. 113
6-17 Force-displacement curve for the "DelWeak" delamination properties with the mixed-mode fracture criterion of eq. (6-19). 114

List of Tables

3-1 Mean properties (± standard deviation) of the butt joint and lap shear tests at quasi-static loading ($3.0 \mu m/s$). 33
3-2 Mean properties (± standard deviation) of the butt joint and lap shear experiments at high-rate loading using DIC measurement. . . 51

4-1 Quasi-static mechanical properties of the CRFP prepreg IM7-8552. 55
4-2 Quasi-static out-of plane mechanical properties of the CRFP prepreg IM7-8552. 56

5-1 Properties of the trapezoidal cohesive law of the adhesive for a deformation rate of $\dot{\delta} = 3 \mu m/s$. 67
5-2 Mechanical properties for the trapezoidal cohesive law of the adhesive for a deformation rate of $\dot{\delta} = 3m/s$. (*) indicates estimated values. 68
5-3 Maximum stress (stress exposure) in the adherends of the high-rate CFRP-CFRP SLJ at the maximum load. 80
5-4 Maximum stress (stress exposure) in the adherends of the high-rate CFRP-aluminium SLJ at the maximum load; (*) only for CFRP; (**) only for aluminium 81
5-5 Sensitivity of the simulation on the cohesive law properties τ_u and J_c. 85
5-6 Sensitivity of the maximum force in the high-rate T-joint simulation on the cohesive law properties τ_u and J_c. 95

6-1 Delamination properties “DelStrong” and “DelWeak”. 108
6-2 Estimation of the minimum critical time-step in thickness direction. 113

1 Introduction

In many industries, the objective of a design engineer is to reduce weight of parts or assemblies. The reason is e.g. in the automotive industry, that the CO_2 emission of new cars have to be reduced according to European government [1]. A weight reduction is also attractive to customers since it decreases the fuel consumption of combustion engines or increases the cruising range of electric vehicles for a given capacity of the battery. By reducing the weight of individual parts, secondary effects arouse which increase the weight saving. In the aviation industry, the weight reduction is also motivated by the reduction of CO_2 emissions. Additionally, the payload of freight or passengers can be increased making flights more profitable to the airlines. In the space flight industry, the weight has a significant influence on the cost of space programs [2]. Another example for weight reduction being a significant cost reduction factor are wind power plants. Reducing the weight of the blades, can lead either to a cheaper design of the plant's tower or enabling larger blades which make the power plant more efficient. Generally, the reduction of weight is strongly correlated with an increase in the performance of engineering products or a reduction of operating costs.

In order to save weight, an optimal lightweight design is necessary. Fibre reinforced plastics (FRPs) bear a high lightweight potential due to their high stiffness and strength in fibre direction related to their density. FRPs are increasingly used in many industries. Complete car bodies made of carbon fibre reinforced plastics (CFRPs) are a well known example for a high usage of FRPs [3]. In the aviation industry, the Airbus A350 XWB as well as the Boeing 787 bear more than 50% FRPs in their fuselage. In wind power plants, not only the blades but also the towers, foundations and transition pieces are taken into consideration for the application of FRP materials [4]. Many other examples, can be found in sports equipment or medical devices. But not only the lightweight potential is an argument for the usage of FRP materials. High energy absorption like for axial crash absorbers in cars, vibration damping, noise absorption and heat insulation can play a big role as well. The tendency of increasing usage of FRP materials can be seen in Fig. 1-1. The demand on carbon fibres within 2012 to 2020 is estimated to increase about 15% per year [5].

With the increasing application of FRP materials, there is a growing demand on adequate joining technologies. Firstly, FRP is not the perfect material for all design cases and only by combining different materials an optimal lightweight design can be achieved. This leads to so called hybrid material structures, which include e.g. joints between metal and FRP substrates. Secondly, an integral manufacturing of parts is generally not possible on the one hand due to the geometric complexity

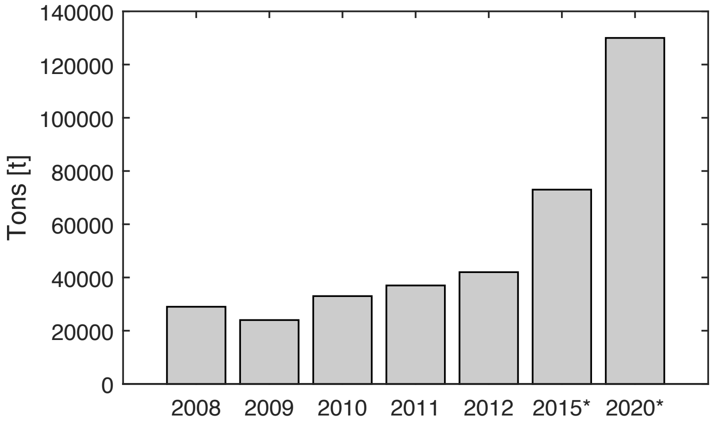

Figure 1-1 Global demand on carbon fibres according to [5] with estimated values (*).

and on the other hand not profitable since reworking costs and costs of production rejects increase. However, the joining technology itself adds some weight to the structure and additional manufacturing and assembling steps come up. The complex loading situation in joining regions, moreover, leads to an increase in the wall thickness that correlates with an increase in weight. These disadvantages of the joining technology decrease the lightweight potential of FRP materials significantly. In the worst case, the structure can even become heavier using FRP parts than using conventional materials due to the joining technology. An optimal lightweight design requires, therefore, also an optimal joining technology for the corresponding materials and application cases.

An important joining technology in the context of FRP materials is the adhesive bonding. The loads in bonded joints can be transferred over large areas and local stress concentration like in welded, bolted or riveted joints can be avoided. Compared to welding, the bonding technology enables a connection of dissimilar or non-meltable substrates. Compared to bolted or riveted joints, no wholes need to be drilled in the substrates that damage the fibres and cause additional manufacturing steps and costs. Adhesive bonding avoids stress concentrations at the notch which is particularly important regarding the anisotropic nature of continuous FRPs. Additionally, a damping of the structure can be realised, manufacturing tolerances can be compensated and a sealing against gases and liquids can be integrated. On the other hand, many challenges have to be overcome. The quality and the mechanical behaviour of an adhesive joint depends on many factors e.g. manufacturing conditions, surface treatment, direction of loading, loading rate and environmental influences. The reliability of the joining technology is nowadays not sufficient to trust purely bonded joints in a primary aircraft structure and the certification process is very difficult. Anyway, in many application cases in the aviation, automotive, space or other industries, bonded joints are increasingly used.

More confidence in the bonding technology can be gained when the qualification methods like non-destructive testing as well as the robustness of the design process are improved. The crash scenario plays an important role in many structural design processes. Especially in the automotive industry, a considerable amount of regulations are defined by the governments according to the Economic Commission for Europe or the Federal Motor Vehicle Safety Standard in the United States. But in the aviation industry, the crashworthiness is relevant as well like in bird strike scenarios or drop tests [6]. Since full scale crash tests require a high experimental effort, simulation models reduce the amount of experiments by enabling a virtual testing. In this field, the Finite Element Method (FEM) has become a common tool in industrial applications.

The challenges for the simulation of bonded joints in crash scenarios are the rate-dependent behaviour of bondlines but also the effort to set up accurate computational models and to solve them in adequate time. The representation of rate-dependency is necessary since the loading rate of a joint is difficult to define a priori. Since the bondline mechanical behaviour can influence the joint failure mode, the structural response can depend strongly on the bondline properties mutually influencing the loading rate of other joints. This creates a dilemma, which can be overcome by a rate-dependent modelling of the bondline. Another difficulty is, that bondlines can have a thickness of a tenth of a millimetre. This usually requires highly refined finite element (FE) meshes in the joining region leading to increased simulation times. Since approximately the year 2000, the cohesive zone modelling (CZM) has proven to efficiently represent adhesive bondlines on a full scale structural level [7].

Since FRP substrates can be laminates consisting of individual plies, the delamination of plies is an issue that changes the structural behaviour of a bonded joint with FRP substrates. Fig. 1-2 shows the effect of the delamination failure qualitatively on the force-displacement curve of a tensile loaded single lap joint (SLJ). It can be seen, that the joint strength as well as the displacement to failure can be significantly reduced. This implies a reduction of the energy absorbed by the structure which is defined by the area covered by the force-displacement curve. Including delamination failure in full-scale crash simulations is currently difficult if at all feasible due to the modelling effort and the computational costs.

1.1 Objectives of the thesis

The simulation can be a powerful tool to make use of the lightweight potential of FRP materials and reduce weight in structures with FRP parts. In this thesis, the

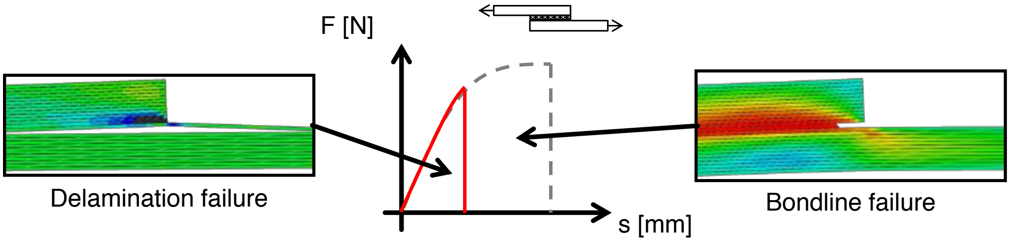

Figure 1-2 Influence of delamination failure on the mechanical behaviour of a bonded joint.

following central aspects have been focused to improve the design of bonded joints with laminated adherends in crash applications:

1. In order to set up valid simulation models, possible ways have to be found to create adequate input data. For the representation of the bondline, cohesive zone laws need to be calibrated for a wide range of loading rates. The question is, how the bondline can be characterised to gain input data for rate-dependent simulation of the bonded joint?
2. An important failure mode of bonded joints is the cohesive failure of the bondline. It is therefore investigated in this thesis, how the rate-dependent behaviour of the bondline can be efficiently represented in full scale crash simulations by cohesive zone modelling?
3. For laminated adherends, the delamination failure must be represented in crash simulations of bonded joints. But how is it possible to model delamination failure in bonded joints with laminated adherends in a full scale crash simulation? A cohesive zone approach is hereby required, that uses the mechanical properties of standardised test methods as input parameters.

Experimental methods and simulation tools will be presented in this thesis to address the mentioned objectives. Regarding the simulations, adequate validation methods will be outlined to estimate the error that is associated with the presented simulation tool.

1.2 Structure of the thesis

In **chapter 2** the theoretical background and the state-of-the-art for the topic is outlined. Firstly, the basics about adhesive joining are explained. Secondly, the theoretical framework of the CZM is presented. Thirdly, an overview and the state-of-the-art about testing adhesives corresponding to the parameter identification for cohesive zones (CZs) is given. The later section includes an overview and the state-of-the-art about high-rate testing of adhesive joints.

Chapter 3 describes the experimental work performed to characterise the mechanical behaviour of an adhesive bondline. This is done with state-of-the-art methods for quasi-static loading rates. For high-rate loading, new methods for the evaluation of the adhesive behaviour on a split-Hopkinson bar (SHB) system are presented.

Chapter 4 provides mechanical properties for the simulation of the adherends. This is done by a literature review as well as quasi-static and high-rate tests.

In **chapter 5** the cohesive law for the simulation of bondline failure is formulated and calibrated. A mixed-mode rate-dependent implementation is provided. The approach is validated under quasi-static and high-rate loading conditions on the coupon level by a SLJ geometry and on a subcomponent level by a T-joint assembly.

Chapter 6 addresses the efficient simulation of delamination failure in a bonded joint with laminated FRP adherends. The approach is formulated and implemented for the two-dimensional (2D) case. The validation of the approach is done in a numerical study comparing it with a conventional modelling of a SLJ.

Chapter 7 gives a conclusion of the thesis and an outlook for further research ideas.

2 Theory and state-of-the-art

In this chapter, the theory and stat-of-the-art of the different research fields associated to the topic are outlined. The relevant theory on adhesive bonding is given in section 2.1. In section 2.2 the basics on the FEM and the state-of-the-art of CZM is presented. The chapter concludes with an overview of testing methods to characterise adhesive bondlines and the basics of high-rate testing in section 2.3.

2.1 Adhesive bonding

According to the definition of Kinloch [8], an adhesive is “ (...) a material which when applied to surfaces of materials can join them together and resist separation”. This definition involves many materials tracing back almost to the beginning of mankind. In this work, the focus lies on materials that are based on an organic polymeric network, which became popular during the 20th century. Among these kind of adhesives, this thesis addresses mainly the structural adhesives which are defined as adhesives “ (...) used when the load required to cause separation is substantial such that the adhesive provides for the major strength and stiffness of the structure” [9]. The substrates that are joined together are referred to as “adherends”.

Adhesives have to be in a liquid state before bonding. They are usually provided as a paste with high viscosity being applied by a glue gun or as a film on a textile carrier. The liquid adhesive consists usually of one or two parts that harden under certain conditions [10]:

- hardening by a loss of solvent
- hardening by a loss of water
- hardening by cooling
- hardening by chemical reaction

A very common adhesive group for structural applications are Epoxides. They can be mixed with hardeners and can react either at room temperature after mixing or need to be cured at elevated temperatures.

2.1.1 Adhesion and cohesion

After curing, the adhesive sticks to the adherend surface through “adhesion”. Under adhesion, physical and chemical connections of the molecules between the adherend and the adhesive polymer is understood [10]. The adhesion interface is shown in Fig. 2-1. The goal of a surface treatment is usually to increase adhesion, i.e. the force that can be transferred from the adherends to the adhesive and vice versa. The results of the surface treatment depend on the adherend materials, the adhesive material and process parameters. Several studies exist about the effect of different surface treatments. They can be separated into chemical treatments like washing processes, mechanical treatments like grinding, milling, sanding or into radiation treatments like laser, plasma or ultraviolet treatment.

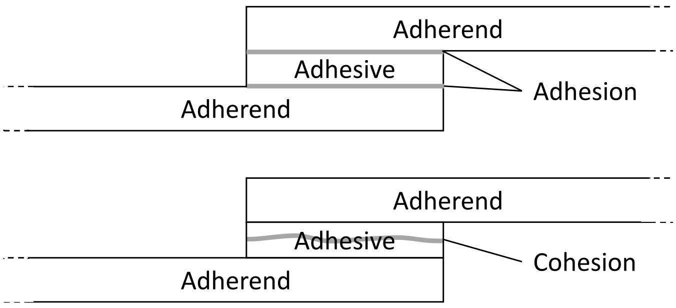

Figure 2-1 Adhesion and cohesion according to [11].

The forces that hold the polymeric network of the adhesive together are called “cohesion”. Physical as well as chemical bonds are responsible for the cohesion of the adhesive. The mechanical properties of the adhesives are dependent on the chemical basis of the polymeric network, the degree of polymerisation, the additives, the environmental aspects like temperature or humidity, the rate of deformation and the stress state.

2.1.2 Mechanical behaviour of bonded FRP structures

In a crash simulation, the mechanical behaviour of a bonded structure in terms of a force-displacement curve must be represented correctly. The mechanical behaviour depends on the joint design and the material properties of the adherends and adhesive. In many cases, the compliance of a bonded structure is dominated by the compliance of the adherends because the overlap region is significantly stiffer than the rest of the structure. This is however not the case, if the adherends are stiff compared to a ductile adhesive and the ratio of overlap length to adhesive thickness is small at the same time [12]. Then the mechanical behaviour of a structure can be dominated by the adhesive mechanical behaviour.

The strength of a bonded joint is strongly dependent on the location of failure. Firstly, the adherends can break which is called adherend failure. If adhesion between the adhesive and the adherend fails, the failure is called adhesion failure.

If the failure occurs within the adhesive, the failure is called cohesive or cohesion failure. If the adherends are made out of FRP laminates, the adherend failure can be subdivided into an in-plane failure of single plies or into an out-of-plane failure. The out-of-plane failure can be either intralaminar transverse failure or interlaminar failure which is also called delamination failure. Fig. 2-2 illustrates the failure modes of an FRP bonded joint. For simplicity, the adhesion failure is neglected in the following, since in automotive, aviation, space and power plant design processes this failure mode is to avoid by surface preparation and quality assurance.

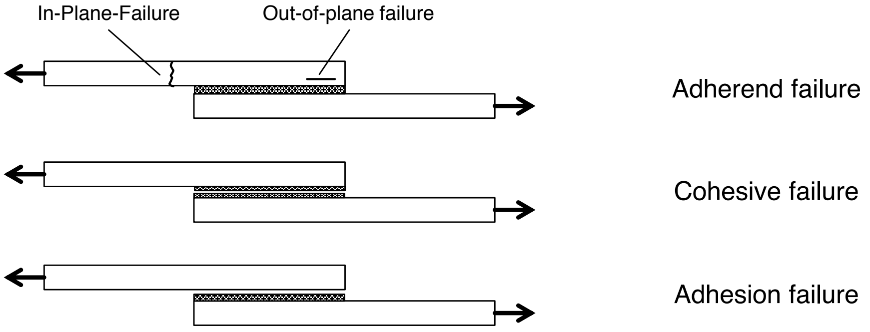

Figure 2-2 Failure modes of a bonded joint with FRP adherends.

The influences on the cohesive failure depend on the joint design and material properties of the adhesive and adherends. If the adherends are stiff compared to a ductile adhesive and the ratio of overlap length to adhesive thickness is small, the adhesive strength dominates the strength of the joint [12]. For joints with rather compliant adherends and sufficiently long overlap length, the fracture energy of the adhesive bondline is most relevant [13, 14].

The cohesive failure can be evaluated by a stress-strain analysis of the bonded joint or by using fracture mechanics criteria. DaSilva [15] summarised the most relevant analytical approaches to calculate the stress-strain distribution in adhesive joints. The numerical analysis e.g. by the FEM is another approach for stress-strain assessment. A detailed review of numerical methods on modelling bonded joints has been recently given by Sauer [16]. Generally, there is the modelling of adhesive bondlines with continuum elements or with cohesive elements which are also called interface elements [17]. The continuum modelling or a combination of continuum modelling and CZM is usually used for detailed simulations or submodels of the joining region. A detailed resolution of the stress-strain distribution over the adhesive bondline can be the result of such an analysis. The evaluation of this stress distribution can be done based on e.g. the maximum stress criterion, von-Mises criterion or a Tsai-Wu criterion [11].

Analytical approaches based on fracture mechanics exist as well. Then, the failure criteria from fracture mechanics can be applied to predict joint failure [11]. A mere

CZM of the adhesive bondline is usually taken, if a full scale structural simulation is performed. An advantage of the CZM is, that it efficiently simulates dynamic crack propagation using fracture mechanics, which makes the approach attractive for crash simulations. In section 2.2 the theory will be outlined in detail.

For the prediction of failure in the FRP adherend, the classical lamination theory or FE continuum models can be used to determine the stress distribution. Several mechanisms can contribute to an in-plane failure [18]:

- Fibre direction: Tensile failure
- Fibre direction: Compressive failure
- Transverse direction: Tensile failure
- Transverse direction: Compressive failure
- In-plane shear failure

The failure of FRP-single layers can be evaluated by failure criteria. In the literature several criteria have been proposed. The failure criteria can be divided into independent criteria like the maximum-stress-criterion, maximum-strain-criterion, into fully dependent criteria like Tsai-Wu, Hoffman or into partly dependent criteria like Hashin, Cuntze, Puck etc. [19].

The out-of-plane failure of the laminate is considered in this work as a delamination failure. This can occur due to a normal loading or shear loading of the resin layer between two adjacent plies. The strength of two neighboured plies against normal debonding is denoted interlaminar tensile strength (ILTS). The strength against shear loading is called interlaminar shear strength (ILSS). The most popular strength based delamination failure criteria are the maximum-stress criterion or a quadratic interaction criterion [20]. From fracture mechanics, the modes of delamination can be separated into a mode I failure, or two shearing mode failure (mode II and mode III) according to Fig. 2-3. The resistance against delamination crack growth is called fracture toughness and is defined in each mode I, II and III. Well-known criteria from fracture mechanics for delamination are the power-law formulation [21] or the Benzeggagh-Kenane criterion [22].

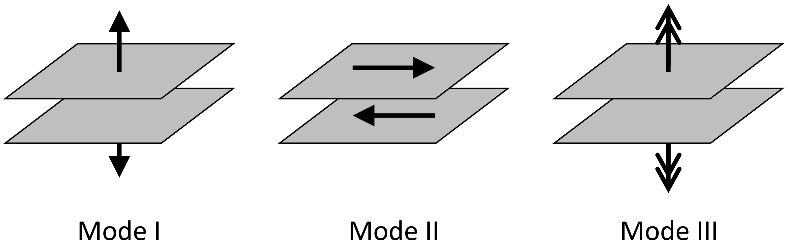

Figure 2-3 Failure modes for delamination failure.

2.2 Theory of cohesive zone modelling

In this thesis, bonded joints are modelled using the CZ approach for the representation of the adhesive bondline. The theory on CZM in the framework of the FEM is described in this section firstly. The section concludes with a short review on CZM used to model adhesive bondlines.

2.2.1 Basics of the dynamic Finite Element Method (FEM)

The FEM has turned out over the last decades as a powerful tool to analyse the mechanical behaviour of structures. It is a numerical tool to solve partial differential equations of various forms. The method became popular in the 1960s with the application to problems in mathematics, physics and engineering [23]. Nowadays several open source and commercial FEM software packages are available. The FE solvers can generally divided into implicit and explicit solvers. To simulate crash scenarios, explicit solvers are currently preferred in industrial use.

A structural problem can be described as a body Ω subjected to boundary conditions and body forces according to Fig. 2-4. The governing equation of the dynamic structural boundary value problem in local form is the momentum equation [24].

$$div(\boldsymbol{\sigma}) + \boldsymbol{b} = \rho \ddot{\boldsymbol{u}} \qquad in \qquad \Omega \tag{2-1}$$

where $\boldsymbol{\sigma}$ denotes the Cauchy stress tensor, $\boldsymbol{b}$ denotes the body force vector, ρ the mass density and $\ddot{\boldsymbol{u}}$ the acceleration of a local point within the body Ω. A reference and a deformed configuration of the body Ω are defined, which are related by the displacements $\boldsymbol{u}$.

$$\boldsymbol{x} = \boldsymbol{x}_0 + \boldsymbol{u} \qquad in \qquad \Omega \tag{2-2}$$

Here, $\boldsymbol{x}$ defines the coordinates of a local point in the deformed configuration, $\boldsymbol{x}_0$ are the coordinates of a local point in the reference configuration. The displacement boundary conditions subjected to the body can generally be described by

$$\boldsymbol{u} = \hat{\boldsymbol{u}} \qquad on \qquad \Gamma_u \tag{2-3}$$

where $\hat{\boldsymbol{u}}$ are the displacements subjected to the boundary Γ_u. The traction boundary conditions are generally described by

$$\hat{\boldsymbol{\tau}} = \boldsymbol{\sigma} \cdot \boldsymbol{n} \qquad on \qquad \Gamma_\tau \tag{2-4}$$

where $\hat{\boldsymbol{\tau}}$ are the tractions subjected to the boundary Γ_τ and $\boldsymbol{n}$ is the surface normal vector. Furthermore, initial conditions are defined according to

$$\boldsymbol{u}(\boldsymbol{x},0) = \boldsymbol{u}_0(\boldsymbol{x}) \qquad \dot{\boldsymbol{u}}(\boldsymbol{x},0) = \dot{\boldsymbol{u}}_0(\boldsymbol{x}) \qquad on \qquad \Omega \tag{2-5}$$

where $\dot{\boldsymbol{u}}$ denotes the velocity and $\boldsymbol{u}_0$ and $\dot{\boldsymbol{u}}_0$ denote the initial displacement and the initial velocity of a local point within the body Ω, respectively.

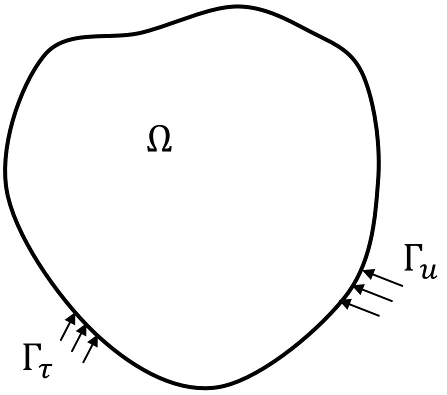

Figure 2-4 Arbitrary body Ω with displacement and traction boundary conditions.

The kinematic relation between displacements $\boldsymbol{u}$ and the strain tensor $\boldsymbol{\epsilon}$ is given by

$$\epsilon_{ij} = \frac{1}{2}\left(\frac{\partial u_i}{\partial x_i} + \frac{\partial u_i}{\partial x_j}\right). \tag{2-6}$$

The relation between stress tensor $\boldsymbol{\sigma}$ and strain tensor $\boldsymbol{\epsilon}$ is given by the constitutive law

$$\boldsymbol{\sigma} = \mathbb{C} : \boldsymbol{\epsilon} \tag{2-7}$$

where $\mathbb{C}$ is the forth-order stiffness tensor. A weak form of the boundary value problem can be formulated by integration of eq. (2-1) over the complete body Ω. Using the principle of weighted residuals with the virtual displacements $\delta\boldsymbol{u}$ as weights yields

$$\int_\Omega \left[\rho\ddot{\boldsymbol{u}} - div(\boldsymbol{\sigma}) - \boldsymbol{b}\right]\delta\boldsymbol{u}d\Omega + \int_{\Gamma_\tau}[\boldsymbol{\sigma}\boldsymbol{n} - \hat{\boldsymbol{\tau}}]\delta\boldsymbol{u}d\Gamma_\tau = 0. \tag{2-8}$$

Applying the Gauss divergence theorem and inserting eqs. (2-7) and (2-6), the weak form can be written in matrix notation as

$$\int_\Omega \delta\boldsymbol{u}^T\rho\ddot{\boldsymbol{u}}d\Omega + \int_\Omega \delta\boldsymbol{\epsilon}^T\boldsymbol{\sigma}d\Omega - \int_\Omega \delta\boldsymbol{u}^T\boldsymbol{b}d\Omega - \int_{\Gamma_\tau}\delta\boldsymbol{u}^T\hat{\boldsymbol{\tau}}d\Gamma_\tau = 0. \tag{2-9}$$

Here, $\delta\boldsymbol{\epsilon}$ denotes the virtual strain matrix. In order to solve the problem numerically, the body Ω is spatially discretised into regularly shaped subsections called finite elements. Then, the displacement field is given as discrete displacements $\boldsymbol{d}$ of the nodes of an element. Between the nodes, the displacements are interpolated by shape functions $\boldsymbol{N}$.

$$\boldsymbol{u}^{(el)} \approx \boldsymbol{N}^{(el)}\boldsymbol{d}^{(el)} \tag{2-10}$$

Applying the spatial discretisation to the weak form yields

$$\begin{split}0 = \sum_{el} \Bigg[\delta \boldsymbol{d}^T \Bigg(\int_{\Omega^{(el)}} \boldsymbol{N}^T \rho \boldsymbol{N} d\Omega \ddot{\boldsymbol{d}} + \int_{\Omega^{(el)}} (\boldsymbol{L}\boldsymbol{N})^T \mathbb{C} (\boldsymbol{L}\boldsymbol{N}) d\Omega \boldsymbol{d} - \\ \int_{\Omega^{(el)}} \boldsymbol{N}^T \boldsymbol{b} d\Omega - \int_{\Gamma_\tau^{(el)}} \boldsymbol{N}^T \hat{\boldsymbol{\tau}} d\Gamma_\tau \Bigg) \Bigg]\end{split} \tag{2-11}$$

where $\boldsymbol{L}$ denotes the spatial derivation matrix and $\delta\boldsymbol{d}$ denotes the virtual nodal displacements. Spatial integration of the weak form e.g. with the Gauss integration, and assembling the contribution of each element to a global set of equations, yields the differential equation

$$\boldsymbol{M}\ddot{\boldsymbol{d}} + \boldsymbol{f}_{int} = \boldsymbol{f}_{ext}. \tag{2-12}$$

where $\boldsymbol{M}$ is the global mass matrix, $\ddot{\boldsymbol{d}}$ is the global acceleration vector, $\boldsymbol{f}_{int}$ is the global internal force vector and $\boldsymbol{f}_{ext}$ is the global external force vector.

The problem can be solved in time by implicit or explicit integration schemes. Here, the explicit time integration by the central difference scheme is explained, since it is most common in commercial explicit FE software packages [25].

$$\dot{\boldsymbol{d}}_{i+0.5} = \dot{\boldsymbol{d}}_{i-0.5} + \frac{\Delta t_{i+1} + \Delta t_i}{2} \boldsymbol{M}^{-1} (\boldsymbol{f}_{ext} - \boldsymbol{f}_{int}) \tag{2-13}$$

$$\boldsymbol{d}_{i+1} = \boldsymbol{d}_i + \Delta t_{i+1} \dot{\boldsymbol{d}}_{i+0.5} \tag{2-14}$$

The central difference integration calculates explicitly the global displacement rate vector $\dot{\boldsymbol{d}}$ between the discrete time-steps Δt_i. The critical timestep Δt_{crit} can be conservatively approximated by an element-wise evaluation according to

$$\Delta t_{crit} = \frac{l_{el}}{c} \qquad with \qquad c = \sqrt{\frac{E}{\rho}} \tag{2-15}$$

where l_{el} is the characteristic element length and E is the Young's modulus of the element's material. For a body Ω with a continuous distribution of displacements, the weak form of eq. (2-1) is valid. However, if discontinuities in structures have to be solved, principles from fracture mechanics can become necessary. In the following, the weak form of the body Ω with a crack are formulated and combined with the spatial discretisation and time integration.

2.2.2 Cohesive zone modelling (CZM)

An efficient method to model cracks in solid structures is the CZM. The method is based on the concept of equilibrium forces at crack surfaces published by Barenblatt [26] and Dugdale [27] in the 1960s. In the CZM the arbitrary body Ω is divided by a crack surface Γ_c into two parts Ω^+ and Ω^- according to Fig. 2-5. The momentum equation according to eq. (2-1) and boundary conditions according to eqs. (2-3) and (2-4) still hold for both parts of the body Ω^+ and Ω^-. For the crack surfaces, an equilibrium condition must be fulfilled.

$$\bar{\boldsymbol{\tau}}^+ = \boldsymbol{\sigma} \cdot \boldsymbol{n} = -\bar{\boldsymbol{\tau}}^- \qquad on \qquad \Gamma_c \tag{2-16}$$

where $\bar{\boldsymbol{\tau}}^+$ and $\bar{\boldsymbol{\tau}}^-$ denote the global tractions on the $+$-side and $-$-side of the crack Γ_c.

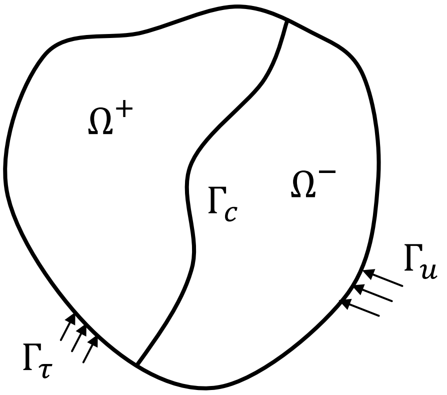

Figure 2-5 Dynamic structural boundary value problem with a crack.

The structural boundary value problem is now formulated in weak form. Using the principal of weighted residuals with the virtual displacements $\delta\boldsymbol{u}$ as weights, the weak form for each body can be written as [28]

$$\begin{aligned} 0 = \int_{\Omega^\pm} \delta\boldsymbol{u}^T \rho \ddot{\boldsymbol{u}} d\Omega^\pm + \int_{\Omega^\pm} \delta\boldsymbol{\epsilon}^T \boldsymbol{\sigma} d\Omega^\pm - \int_{\Omega^\pm} \delta\boldsymbol{u}^T \boldsymbol{b} d\Omega^\pm - \\ \int_{\Gamma_\tau^\pm} \delta\boldsymbol{u}^T \hat{\boldsymbol{\tau}} d\Gamma_\tau^\pm - \int_{\Gamma_c^\pm} (\delta\boldsymbol{u}^\pm)^T \bar{\boldsymbol{\tau}}^\pm d\Gamma_c^\pm \end{aligned} \tag{2-17}$$

Summarising over both parts of the body and using eq. (2-16) yields

$$\begin{aligned} 0 = \int_{\Omega} \delta\boldsymbol{u}^T \rho \ddot{\boldsymbol{u}} d\Omega + \int_{\Omega} \delta\boldsymbol{\epsilon}^T \boldsymbol{\sigma} d\Omega - \int_{\Omega} \delta\boldsymbol{u}^T \boldsymbol{b} d\Omega - \\ \int_{\Gamma_\tau} \delta\boldsymbol{u}^T \hat{\boldsymbol{\tau}} d\Gamma_\tau - \int_{\Gamma_c} (\delta[\![\boldsymbol{u}]\!])^T \bar{\boldsymbol{\tau}} d\Gamma_c \end{aligned} \tag{2-18}$$

This is the weak form of the complete body Ω which includes a crack Γ_c. The crack is kinematically described by a virtual global displacement jump vector $\delta[\![\boldsymbol{u}]\!]$.

$$\delta[\![\boldsymbol{u}]\!] = \delta\boldsymbol{u}^+ - \delta\boldsymbol{u}^- \tag{2-19}$$

where $\delta\boldsymbol{u}^+$ and $\delta\boldsymbol{u}^-$ denote the virtual displacements of the surfaces on Γ_c.

The global displacement jump $[\![\boldsymbol{u}]\!]$ can be transferred into the local displacement jump $\boldsymbol{\delta}$ by

$$\boldsymbol{\delta} = \boldsymbol{\Theta}[\![\boldsymbol{u}]\!] \tag{2-20}$$

where $\boldsymbol{\Theta}$ denotes the mapping tensor, which is defined by the following considerations [28, 29]: The crack interface $\bar{\boldsymbol{x}}$ is defined in the deformed configuration by

$$\bar{\boldsymbol{x}} = \boldsymbol{x}_0 + 0.5(\boldsymbol{u}^+ + \boldsymbol{u}^-) \qquad on \qquad \Gamma_c \tag{2-21}$$

Two tangential vectors are now defined on the interface by coordinate gradients.

$$v_{\eta_i} = \frac{\partial \bar{x}_i}{\partial \eta} \tag{2-22}$$

$$v_{\xi_i} = \frac{\partial \bar{x}_i}{\partial \xi} \tag{2-23}$$

η and ξ denote curvilinear coordinates on the interface, here. The interface orthonormal vector can then be defined by

$$\boldsymbol{v}_n = \frac{\boldsymbol{v}_\xi \times \boldsymbol{v}_\eta}{||\boldsymbol{v}_\xi \times \boldsymbol{v}_\eta||}. \tag{2-24}$$

An orthonormal basis is then defined by

$$\boldsymbol{v}_s = \frac{\boldsymbol{v}_\xi}{||\boldsymbol{v}_\xi||} \tag{2-25}$$

and

$$\boldsymbol{v}_t = \boldsymbol{v}_n \times \boldsymbol{v}_s \tag{2-26}$$

Then, the mapping tensor $\boldsymbol{\Theta}$ consists of the components of $\boldsymbol{v}_n$, $\boldsymbol{v}_s$ and $\boldsymbol{v}_t$. The mapping tensor can be also used to map the global tractions on the local interface surface tractions.

$$\boldsymbol{\tau} = \boldsymbol{\Theta}\bar{\boldsymbol{\tau}} \tag{2-27}$$

The constitutive law connecting the local displacement jump vector $\boldsymbol{\delta}$ and local surface traction vector $\boldsymbol{\tau}$ is given via a cohesive law matrix $\boldsymbol{S}$, which defines a traction-separation relation.

$$\boldsymbol{\tau} = \boldsymbol{S}\boldsymbol{\delta} \tag{2-28}$$

Insertion of eqs. (2-20) and (2-28) into the weak form of eq. (2-18) yields

$$\begin{aligned} 0 = \int_{\Omega} \delta \boldsymbol{u}^T \rho \ddot{\boldsymbol{u}} d\Omega + \int_{\Omega} \delta \boldsymbol{\epsilon}^T \boldsymbol{\sigma} d\Omega - \int_{\Omega} \delta \boldsymbol{u}^T \boldsymbol{b} d\Omega - \\ \int_{\Gamma_\tau} \delta \boldsymbol{u}^T \hat{\boldsymbol{\tau}} d\Gamma_\tau - \int_{\Gamma_c} (\delta [\![\boldsymbol{u}]\!])^T \boldsymbol{\Theta}^T \boldsymbol{S} \boldsymbol{\Theta} [\![\boldsymbol{u}]\!] d\Gamma_c \end{aligned} \tag{2-29}$$

After discretisation of the body Ω, the displacement field on each side of the body $\Omega^{\pm}$ is approximated by interpolation functions $\boldsymbol{N}$ according to eq. (2-10). For the displacement jump, the shape functions on each side of the crack Γ_c have to be considered with different signs.

$$[\![\boldsymbol{u}]\!]^{(el)} \approx (\boldsymbol{N}^{\pm})^{(el)} \boldsymbol{d}^{(el)} \quad with \quad (\boldsymbol{N}^{+})^{(el)} = -(\boldsymbol{N}^{-})^{(el)} \quad on \quad \Gamma_c \tag{2-30}$$

The contribution of the crack to the weak form of eq. (2-18) is separated from the whole body Ω using cohesive elements. The cohesive element is subsequently integrated to get the components of the element's internal force vector.

$$\boldsymbol{f}_{int}^{(el)} \approx \int_{\Gamma_c} (\boldsymbol{N}^{\pm})^T \boldsymbol{\Theta}^T \boldsymbol{S} \boldsymbol{\Theta} \boldsymbol{N}^{\pm} d\Gamma_c \boldsymbol{d} \tag{2-31}$$

A Newton- Cotes integration is chosen for the surface integral of eq. (2-31) [29]. Assembling the contributions of every element to the global degrees of freedom leads to the second order differential equation according to eq. (2-12) which can be subsequently integrated in time by the central difference scheme.

2.2.3 Cohesive laws for the simulation of the cohesive behaviour of adhesives

Various shapes for the cohesive law have been proposed. The first works, used reversible cohesive laws of triangular, non-linear or trapezoidal shape as shown in Fig. 2-6 for the crack growth in brittle or ductile materials [30–32]. The cohesive laws were defined as boundary conditions and a different behaviour in normal or shear opening - i.e. a mode mixity - was not accounted for at this stage. Irreversible, mixed-mode cohesive laws of the same shapes were proposed later, and the idea was embedded into finite cohesive elements [33, 34]. Other shapes of the cohesive law were proposed later like linear-parabolic, polynomial, exponential, etc. [35–37].

Cohesive elements have been used for modelling the cohesive behaviour of adhesives either in addition to continuum elements to account for failure in the bondline or as one CZ over the complete bondline thickness [7]. The later case is focused in this

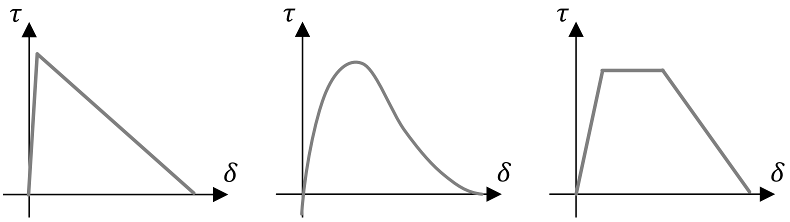

Figure 2-6 Triangular, non-linear and trapezoidal cohesive law.

thesis to keep the modelling and computational effort as small as possible. Yang et al. were the first, who simulated the complete adhesive cohesive behaviour with one layer of cohesive elements in pure mode I [38], in pure mode II [39] and for mixed-mode loading conditions [40]. They used a trapezoidal shape of the cohesive law. Campilho et al. [41] used a triangular mixed-mode cohesive law for the simulation of SLJs.

Both triangular and trapezoidal cohesive laws became most common to simulate the cohesive behaviour of adhesives. The triangular cohesive laws are more suitable for brittle behaviour and trapezoidal cohesive laws are more suitable for ductile behaviour. The requirements on the accuracy of the cohesive law shape increase the stiffer the adherends and the shorter the overlap length is [12]. While triangular irreversible cohesive laws usually use a degradation variable to define the cohesive law, the irreversible trapezoidal cohesive law can be defined solely by a degradation variable [42] or by definition of plasticity and degradation [43]. A sketch of a reversible, a elastic-degradation and an elastic-plastic-degration cohesive law is shown in Fig. 2-7.

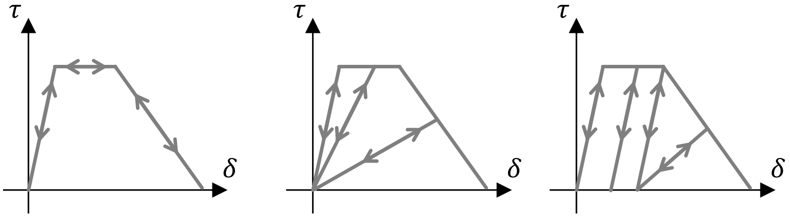

Figure 2-7 Different formulations for a trapezoidal cohesive law: reversible (left), elastic-degradation (middle) and elastic-plastic-degration (right).

Ductile adhesive materials used in automotive application can show a significant rate-dependency. Marzi et al. [44] and Matzenmiller et al. [45] implemented an elastic-plastic cohesive law accounting for rate-dependency in the yield stresses and the fracture energies in normal and shear mode. The authors found that rate-dependency is essential for the simulation of crash structures. A rate-dependency on the stiffness has not been taken into account without any consequences for the bonded joints simulated. Other studies used visco-elastic formulations to account for rate-dependency. Musto and Alfano [46] realised visco-elasticity by a Maxwell model and a Hookean spring in parallel and found a good approximation of the rate-dependent behaviour of a double cantilever beam (DCB) test and simulation with a constant definition of the degradation variable. In the work of Rauh [47], bonded joints with thick adhesive bondlines of several millimetres are experimentally investigated and modelled by a visco-elastic cohesive law with a rate-dependent yield stress and rate-dependent degradation. The characterisation of the cohesive law in the later work was done with the time-temperature-shift method [48]. This method was applied to hyper-elastic adhesives.

2.3 Testing of adhesive joints

An overview on test methods to calibrate cohesive laws for adhesive bonds is provided in section 2.3.1. Then, an overview on test methods for high-rate loading is given in section 2.3.2. The theoretical background for the SHB test set-up with the classical data reduction scheme will be described in section 2.3.3. Finally, a literature review on SHB testing of adhesive joints is done in section 2.3.4.

2.3.1 Adhesive testing for cohesive laws

The cohesive behaviour of an adhesive bondline can be found by three methods. In the inverse method, the cohesive law is found by an iterative search using simulations and experimental findings. Usually a shape of the cohesive law is assumed before starting the search [7]. Another method to find the cohesive law is to deduce relevant properties directly from the tests. If the results of several tests are combined, the method is described as “property determination technique”. A third method is the direct measurement of the cohesive law from one test.

Commonly used test methods for direct characterisation of the cohesive law will be explained in the following. Firstly, it is worth noticing that for quantitatively testing the mechanical behaviour of an adhesive, tests in normal direction, in shear direction and in combined loading directions are relevant. Since the CZM is an approach coming from the field of fracture mechanics, the loading directions are also referred to as normal mode (or mode I) or shear mode (or mode II and mode III) as shown in Fig. 2-3 and mixed-mode loading.

To directly test the normal behaviour of an adhesive material, the uniaxial tension test according to ASTM D 638 or EN ISO 527-2 is adequate [49]. In this test, a state of uniaxial stress is present. The Young’s modulus, the Poisson ratio as well as the strength under uniaxial stress condition can be quantified from this test. Many organic polymers can show, however, a dependency in their strength on the hydrostatic stress state. This stress state arouses when thin layers confined by two adherends are deformed, which is generally the case for adhesive bonds. It is, therefore, difficult to transfer the mechanical data from the uniaxial tension test to the mechanical behaviour of adhesive bonds [50, 51]. The transformation of the stiffness is possible if in the test of the bond a Poisson effect of the adhesive can be assumed negligible. Then the stiffness of the uniaxial test can be converted to the stiffness of the bond by [52]

$$\frac{E_a}{E} = \frac{1-\nu}{(1+\nu)(1-2\nu)} \tag{2-32}$$

where ν is the Poisson ratio and E is the Young's modulus from the uniaxial tension test. E_a is the apparent stiffness of a perfectly constrained adhesive bondline by the adherends. The strength in normal direction of the adhesive bondline with a certain thickness can be found by a butt joint test according to ASTM D 897 [49]. A conversion of the strength from the uniaxial tension test and the butt joint test is not suggested [50].

The fracture energy of an adhesive bondline can be determined by fracture mechanics tests. Most commonly, the DCB test or the tapered DCB test are used. The standards are ASTM D 3433 or the British standard ISO 25217 [49]. Some authors used the "property determination method" and performed uniaxial tension tests, optionally butt joint tests and DCB tests to calibrate a triangular or trapezoidal cohesive law of an adhesive bondline and found a good correlation between simulation and experiments of a SLJ [7, 12, 39, 53]. Sørensen [54] and Stigh et al. [55] proposed a method to get the complete behaviour of an adhesive bondline directly, using a DCB specimen. This was done by the derivation of an analytical J-integral expression towards the measured crack tip opening.

In shear direction the thick adherend shear test (TAST) according to ASTM D 3983 or ISO 11003-2 is widely used to get the stiffness and stress-strain curve of an adhesive bondline up to the maximum strength [49]. The TAST can be performed with most quasi-static tensile testing machines. But it has the disadvantage, that a pure shear deformation of the adhesive is not present during the test since peel stresses at the edge of the overlap occur depending on the mechanical properties of the adherends and the adhesive. The butt torsion test according to ASTM E 229 is considered a better approach to a pure shear deformation [49]. However, a torsional testing machine is necessary, which is not the standard in many testing labs. Since adhesives are generally isotropic materials, a conversion of the Young's modulus E to the shear modulus G is possible by

$$G = \frac{E}{2(1+\nu)}. \tag{2-33}$$

Inserting eq. (2-32) into eq. (2-33) leads to

$$\nu = \frac{E_a - 2G}{2(E_a - G)}. \tag{2-34}$$

Eq. (2-34) is useful to check the plausibility of the tests in normal direction like the butt joint test and the test in shear direction like the TAST. The Poisson ratio of most engineering adhesives has to be in the range of 0.3 to 0.5 [11]. The shear strength of adhesives is, however, difficult to calculate from normal mode testing. It is however worth noticing that the shear failure of an adhesive is usually a tensile failure, since the principle stress state of a shear loading is that of an tensile loading in approximately 45° direction [56].

No standardised fracture mechanics test for a characterisation of an adhesive bondline in shear direction is available. Many test geometries have been proposed, but most commonly the end-notched flexural (ENF), the tapered ENF or the end-loaded-split specimen are used [11]. The cohesive law according to the “property determination method” in shear direction can be defined combining the test results of TAST or butt torsion test and the fracture energy from fracture mechanics tests. In shear direction Leffler et al. [56] and Stigh et al. [55] proposed methods to deduce the complete cohesive law directly from the ENF test by the derivation of a closed form J-integral expression towards the crack tip opening.

For combined loading or mixed-mode loading conditions of an adhesive bondline the Arcan test method can be applied to find the strength of adhesives [49]. Similarly, by tensile testing of a bonded joint that has an inclined bondline, i.e. a scarf joint, a combined loading stress state can be achieved during the test. It is, however, difficult to get a defined combined loading condition, because the normal or shear components can vary spatially over the overlap distance and over time of testing. Therefore, the butt torsion test can be combined with a tensile loading to achieve better accuracy in the mixed-mode loading [57, 58]. This method requires however special testing machines, which are rarely available.

The mixed-mode fracture energy of an adhesive bondline can be found by fracture mechanics specimen varying the adherend thicknesses [59]. Another method is to vary the supports and point of load introduction [60]. Thereby, it has been found out that for many adhesives the fracture energy is linearly dependent on the mixed-mode ratio [39, 60, 61]. Also for mixed-mode loading conditions a direct measurement of the cohesive law has been proposed by the derivation of a J-integral expression [62].

Since adhesives can show a rate-dependent mechanical behaviour, it can be necessary to test at varying loading rates. Test methods for the characterisation of adhesives in the high-rate loading range will be outlined in the next section.

2.3.2 Test methods for high-rate testing

Materials can be mechanically tested at various deformation rates which are provided by different test set-ups. Standard testing machines like electro-mechanical and servo-hydraulic testing rigs provide a testing range of $0.001 mm/s$ up to several $100 mm/s$ [63]. These machines offer the possibility to test the quasi-static and intermediate-rate properties of materials. The strain rate can be defined as the derivation of the material's strain towards time.

$$\dot{\epsilon} = \frac{d\epsilon}{dt} \tag{2-35}$$

The strain rates in electro-mechanical and servo-hydraulic testing rigs are in the range of $10^{-5}s^{-1}$ up to $10^{-1}s^{-1}$. Special servo-hydraulic testing rigs offer testing speeds for the intermediate strain rate range up to $10^{2}s^{-1}$ [64].

Drop tower tests, pendulum impact tests or rotating wheel tests are very common for high-rate testing. The testing speeds can reach several meters per second. An impactor is accelerated in the tests e.g. by gravity or by a motor, that hits the specimen at one end, while the other end of the specimen is fixed. The specimen displacements are measured by evaluation of the recorded force-time signal at the fixed end and the impactor mass. The drop tower tests are suitable to test specimens from coupon size up to component level. Problematic in the high-rate testing of bigger specimen is, that a uniform deformation of the specimen is not present during the test [64]. This can cause large oscillations and errors in the measured signals, when the results are directly related to the material behaviour of the specimen.

Another testing set-up for high-rate testing is the SHB. The advantage compared to the drop tower test and similar high-rate tests is, that a uniform deformation of the specimen is possible at high strain rates up to $10^{4}s^{-1}$. Additionally, a constant deformation rate can be achieved with special techniques like pulse shaping [65]. In the classical compression set-up as shown in Fig. 2-8, an impactor called striker bar hits a second bar called incident bar. The striker bar is accelerated by a pressure gun up to a velocity V_0. Through the impact, an elastic wave is created in the incident bar that propagates to the other end of the incident bar where the specimen is located. The elastic wave gets reflected at the bar specimen interface and transferred over the specimen to the transmission bar. The specimen's mechanical behaviour is measured through the change of the shapes of the elastic waves that travel through the incident and transmission bar and are measured by strain gauges [66].

The specimen size used in a SHB set-up is at the coupon level and usually smaller than the standardised specimen geometry. The reason is that the relative displacements of the bar ends are in the range of a few millimetres, which is usually not enough to load a standard specimen size up to failure. A small specimen size additionally promotes a dynamic force equilibrium which is important to minimize errors in the determination of material properties.

In the following the SHB testing is focused since the achieved loading rates are relevant for crash scenarios in automotive and aviation industries and quantitative

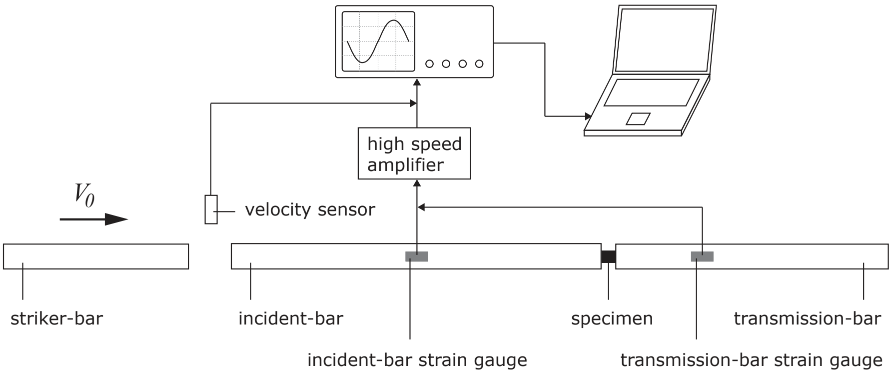

Figure 2-8 Classical compression SHB set-up [65].

material properties can be gained. The basics of the classical SHB analysis (SHBA) procedure are outlined in the next section.

2.3.3 Theory of split-Hopkinson Bar (SHB) testing

The Hopkinson bar set-up is named after its inventors John and Bertram Hopkinson. A major contribution on the development of the set-up had Kolsky [67]. That is why the set-up is also referred to as Kolsky bar set-up. A modern compression SHB set-up like in Fig. 2-8 consists of the striker, incident and transmission bar, a velocity sensor for measurement of the striker bar impact speed, strain gauge terminals on the incident and transmission bar for the measurement of the elastic strain waves, a high-speed amplifier, an oscilloscope and finally a computer for the storage and evaluation of the measured data.

During an SHB experiment, the strain wave signal on the strain gauge terminal of the incident bar $\epsilon_{0,inc}$ and the transmission bar $\epsilon_{0,tra}$ is measured. For the evaluation of the specimen mechanical behaviour, strain gauge signals are shifted in time to get the strain signals directly at the specimen.

$$t_{\epsilon_{inc}} = t_0 \tag{2-36}$$

$$t_{\epsilon_{ref}} = t_0 - 2\frac{\Delta l_{inc}}{c_b} \tag{2-37}$$

$$t_{\epsilon_{tra}} = t_0 - \frac{\Delta l_{inc}}{c_b} - \frac{\Delta l_{tra}}{c_b} \tag{2-38}$$

Here, t_0 denotes the starting time of the original data record at the incident bar and transmission bar. Δl_{inc} and Δl_{tra} are the distances of the strain gauge terminals from the incident and transmission bar to the specimen, respectively. c_b is the propagation speed of an elastic wave in the bars, which can be calculated using eq. (2-15). $t_{\epsilon_{inc}}$, $t_{\epsilon_{ref}}$ and $t_{\epsilon_{tra}}$ denote the shifted starting times of the incident wave signal ϵ_{inc}, the reflected wave signal ϵ_{ref} and the transmitted wave signal ϵ_{tra}, respectively [65].

The data reduction of a compression SHB experiment bases on the second-order differential equation of the one-dimensional (1D) wave propagation [66]. After shifting the raw strain gauge signals in time, the particle velocity of the incident bar end $\dot{u}_{inc}$ and the particle velocity of the transmission bar end $\dot{u}_{tra}$ can be calculated by

$$\dot{u}_{inc} = c_b(-\epsilon_{inc} + \epsilon_{ref}) \tag{2-39}$$

$$\dot{u}_{tra} = -c_b\epsilon_{tra} \tag{2-40}$$

Then, the specimen deformation rate $\dot{u}_{spe}$ can be calculated by

$$\dot{u}_{spe} = \dot{u}_{inc} - \dot{u}_{tra}. \tag{2-41}$$

Inserting eqs. (2-39) and (2-40) into eq. (2-41) leads to an equation for the specimen deformation rate depending on the measured strain signals ϵ_{inc}, ϵ_{ref} and ϵ_{tra}.

$$\dot{u}_{spe} = c_b(-\epsilon_{inc} + \epsilon_{ref} + \epsilon_{tra}) \tag{2-42}$$

If the strain is uniformly distributed over the free length of the specimen l_{spe}, the specimen strain rate $\dot{\epsilon}_{spe}$ can be calculated by

$$\dot{\epsilon}_{spe} = \frac{\dot{u}_{spe}}{l_{spe}} = \frac{c_b}{l_{spe}}(-\epsilon_{inc} + \epsilon_{ref} + \epsilon_{tra}) \tag{2-43}$$

Integration of eqs. (2-42) and (2-43) in time yields the specimen deformation or the specimen strain, respectively.

$$u_{spe} = c_b \int (-\epsilon_{inc} + \epsilon_{ref} + \epsilon_{tra})dt \tag{2-44}$$

$$\epsilon_{spe} = \frac{c_b}{l_{spe}} \int (-\epsilon_{inc} + \epsilon_{ref} + \epsilon_{tra})dt \tag{2-45}$$

The reaction forces at the incident bar end F_{inc} and at the transmission bar end F_{tra} caused by the deformation of the specimen can be calculated by [66]

$$F_{inc} = -A_bE_b(\epsilon_{inc} + \epsilon_{ref}) \tag{2-46}$$

and

$$F_{tra} = -A_bE_b\epsilon_{tra}. \tag{2-47}$$

Here, A_b denotes the cross sectional area of the bars. If both forces are equal ($F_{inc} = F_{tra}$), a dynamic force equilibrium is apparent during the test. Then, the following relation between the strain signals can be stated:

$$\epsilon_{inc} + \epsilon_{ref} = \epsilon_{tra} \tag{2-48}$$

Using eq. (2-48) in eq. (2-43) to eliminate the transmission strain wave signal ϵ_{tra}, the strain rate $\dot{\epsilon}_{spe}$ in the specimen can be calculated by

$$\dot{\epsilon}_{spe} = 2\frac{c_b}{l_{spe}}\epsilon_{ref}. \tag{2-49}$$

This is called a one-wave analysis of the strain rate. Using eq. (2-48) in eq. (2-43) to eliminate the reflected strain wave signal ϵ_{ref}, yields

$$\dot{\epsilon}_{spe} = 2\frac{c_b}{l_{spe}}(-\epsilon_{inc} + \epsilon_{tra}). \tag{2-50}$$

This is called two-wave analysis. Accordingly, eq. (2-43) is called three-wave analysis.

Eqs. (2-39) to (2-50) represent the equations of the classical SHBA for compression SHB systems. The equations are accurate, if the assumptions for the second-order differential equation of 1D-wave-propagation are fulfilled. These are [65]

1. The strain waves in the incident and transmission bar are elastic.
2. The wave propagation in the bars is 1D.
3. The bar interfaces of incident and transmission bar remain plane.
4. The specimen is in a dynamic force equilibrium.
5. Inertia and friction can be neglected.

The equations can easily be adopted to a tensile SHB system by changing the sign of the strain gauge signals in eqs. (2-39) to (2-50).

2.3.4 SHB testing of adhesive joints

This section is partly taken from a previous publication of the author [68]. The SHB set-up has turned out to be an appropriate technique to test adhesive joints at high loading rates [69, 70]. Keisler and Lataillade [71] were the first who tested bonded joints on a SHB system. They investigated the influence of surface roughness and surface treatment on the shear strength of a single lap specimen with rigidly supported adherends. This concept has been used by several other authors to test the shear strength properties of bonded joints [72–76]. Other specimen geometries have also been used to find high-rate effects on bonded joints shear stress. Yokoyama [77] used a pin collar arrangement on a compression SHB and evaluated the shear strength of the joint. Kihara [78] bonded an adherend tangentially on an incident bar with an hexagonal cross-section of an compressive SHB set-up. Raykhere [79] used a torsional SHB to test the shear behaviour of bonded joints.

Other studies have addressed the tensile strength of bonded joints. Martinez et al. [80] were the first to test the compressive properties of a butt joint on a compressive SHB. Yokoyama [70] evaluated the tensile strength and energy absorbed of butt joints on a tensile SHB. Wang [81] evaluated the tensile strength of modified butt joints on a tensile SHB to compensate large stress gradients at the joint edges. Yokoyama [82] used a hat shaped specimen to evaluate the joint tensile strength on a compressive SHB.

A combined loading set-up was presented by Sato and Ikegami [57]. They used a tension-torsion SHB to test the tensile, the shear and mixed loading conditions. Zhao [83] used a tensile SHB set-up to test a SLJ and evaluated the complete force-displacement curve to find the energy absorbed of the joint. Challita [84] used a double lap joint to find the shear maximum stress- maximum strain curves and joint failure strain of a bonded joint. They used correction factors from FE simulations to improve the accuracy of SHBA results.

Recently, the strain measurement in the compression and tensile SHB has been validated by strain gauges applied on metallic specimens and high-speed imaging with subsequent visual evaluation of the specimen strain [85, 86]. It has been found out that for compressive SHB systems, the SHBA gives accurate results. For the tensile SHB set-up, the strain measurement based on SHBA can bear errors depending on the geometry and properties of the specimen's material. Therefore, high-speed imaging and digital image correlation (DIC) came into use for the evaluation of the specimen deformations [87].

2.4 Summary of the chapter

It has been shown in this chapter, that many fields of research are involved with the characterisation and simulation of adhesively bonded joints with laminated adherends in crash applications. From the experimental point of view, the characterisation of the mechanical behaviour of the bondline and the adherend for FE crash models has open questions. Especially, the characterisation at elevated loading rates requires further research.

The research in this thesis focuses on the characterisation of the adhesive bondline, since it has usually a stronger dependence on the loading rate than the adherend and a stronger influence on the joint strength. The characterisation of an adhesive bondline at high loading rates gives still room for further research. Firstly, the characterisation of a bondline on a SHB system for cohesive zone modelling has not yet been addressed by other authors. It will be outlined, which sample geometry can be used and which data reduction scheme is preferable to gain adequate input data. In this context, the characterisation for mixed-mode high-rate loading conditions is a topic with few experience. Secondly, the literature misses validation tests like a single lap joint on a SHB system. Other high-rate test set-ups have been used with a standard sample size. However at high-rate loadings, a dynamic force equilibrium is difficult to obtain in these cases.

For the adherends, e.g. the effect of high loading rates on the fracture energies of delaminations is still an open question [65, 88]. Moreover the dependence of interlaminar properties on the strain rate, fibre volume fraction and fibre orientation lacks for experimental work and deeper understanding. In this thesis, a literature review will be given to identify the most important input parameters for the simulation and validation.

For the simulation of adhesive joints in crash applications, various loading conditions as well as loading rates can occur. Additionally, the behaviour of an adhesive bondline in a crash structure can influence the loading conditions as well as loading rates of other bondlines in the remaining structure and vice versa. To solve this dilemma, a modelling based on the loading condition as well as the loading rate is necessary. Concerning the simulation of bondlines with the CZM, the state-of-the-art cohesive laws have one of the following shortcomings:

- The cohesive law is rate-independent [42, 61].
- The cohesive law does not account for visco-elastic effects, i.e. rate-dependence in elastic part is missing [44].
- The calibration is difficult to perform or not applicable to some adhesives like the time-temperature principle [47].

Therefore a mixed-mode rate-dependent cohesive law is formulated, calibrated and validated in this thesis.

In the literature, many works deal with the simulation of delamination failure and others with bondline failure using CZM. The simulation of bonded joints with laminated adherends, however, requires both failure modes. Modelling both failure modes independently adds modelling effort and computational cost to the simulation engineer while computationally efficient methods would be desired. In this thesis, an approach will be presented to tackle this problem.

3 Characterisation of the adhesive

The adhesive mechanical properties have a crucial influence on the mechanical behaviour of an adhesively bonded joint. In this chapter, the experimental work for the characterisation of the adhesive is described. For all experiments, the toughened epoxy adhesive Betamate™ 1480 V203 (DOW Chemicals, Midland/Michigan, United States) was used with a bondline thickness of $T_{coh} = 0.3mm \pm 0.05mm$. Experiments to measure the stiffness and strength were performed using a butt joint and a lap shear test with thick adherends. This is done for quasi-static loading in section 3.1. Additionally, fracture mechanics tests were performed and evaluated to directly to find the cohesive law in terms of a traction-separation relation for quasi-static loading rates in section 3.2 and 3.3.

The adhesive was tested quasi-statically in a scarf joint in section 3.4. This was done to validate the CZ law for combined loading conditions in section 5.1.2. For the validation of adhesive's cohesive behaviour at intermediate-rate loading, experiments with butt joint specimen were done and are outlined in section 3.5. Finally, the adhesive tested at high-rate loading on a tensile SHB system is described in section 3.6. The influence of the deformation measurement by means of SHBA and DIC measurement is hereby investigated.

The results of the butt joint, lap shear and scarf joint test are presented in terms of an average stress σ which is defined as

$$\sigma = \frac{F}{A_0}. \tag{3-1}$$

where F denotes the force signal divided by the initial bonding area A_0. The deformation Δ of the adhesive bondline has been evaluated in $[mm]$. The reason is that a comparison of the measured quantities with a cohesive law from the fracture mechanics tests and with the calibration of the cohesive law in section 5.1.2 is straightforward. Accordingly, the unit $[N/mm^3]$ is used instead of $[MPa]$ for the stiffness of the bondline.

The tensile strain ϵ or shear strain γ in the adhesive can be evaluated dividing the deformation Δ through the bondline thickness T_{coh}.

$$\epsilon = \frac{\Delta}{T_{coh}} \qquad (for\ butt\ joint\ specimen) \tag{3-2}$$

$$\gamma = \frac{\Delta}{T_{coh}} \qquad (for\ lap\ shear\ specimen) \tag{3-3}$$

This measure must be, however, interpreted with caution. For the butt joint test, it would assume that the strain is equally distributed over the bondline thickness. Moreover, it bears the danger to assume an uniaxial strain state. This is, however, not true due to the bounding effect of the adherends. The same accounts for the stress measure. It should not be interpreted as the stress in the adhesive seen as a continuum but rather as the stress that the adhesive applies to the adherend surfaces i.e. adherend surface tractions.

3.1 Quasi-static testing of the adhesive with butt joint and lap shear tests

3.1.1 Specimen manufacturing and testing

Some contents in this section are taken from a previous publication of the author [68]. The geometry of the butt joint and lap shear specimen can be seen in Fig. 3-1. Both specimen are designed based on the standards ASTM D 897 and ASTM D 3983, respectively, but modified to enable an insertion in the SHB high-rate testing set-up (see section 3.6). Each specimen consisted of two stainless steel adherends joined with the adhesive. The adherends were grit-blasted with glass spheres with a diameter of $180\mu m$ to $200\mu m$ before bonding. All specimens were cured in an oven at $180^{\circ}C$ for $30min$ in accordance with the manufacturer's guidelines [89], being held together using a custom-made fixture ensuring proper alignment. The bonding area in the butt joint tests was circular with a diameter of $10.5mm$. In the lap shear specimens, the bonding area was rectangular with a size of $10.5mm$ x $10mm$.

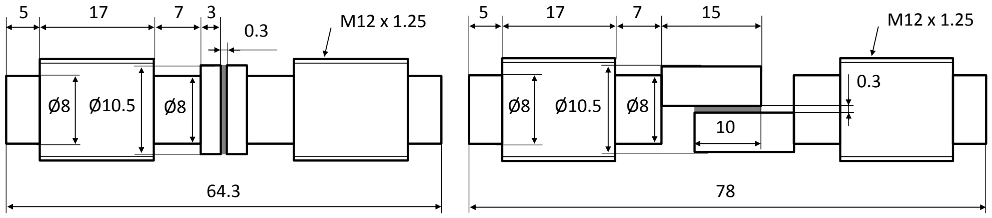

Figure 3-1 Specimen geometry of the butt joint (left) and the lap shear specimen (right) [68].

After curing, the adhesive thickness was found to be within $0.3mm \pm 0.05mm$. In total, four butt joint and five lap shear specimens were quasi-statically tested. For the deformation measurement of the butt joint specimen, two markers were bonded on the adherend surface for visual measurement of the deformations. For the deformation measurement of the lap shear specimen a black-on-white speckle pattern was sprayed on the specimens for DIC measurement. Representative specimen are shown in Fig. 3-2.

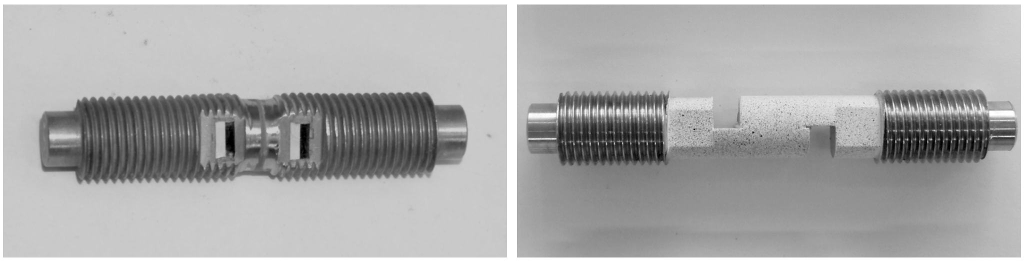

Figure 3-2 Representative specimen for the butt joint test (left) and the lap shear test (right).

The quasi-static tests were performed at a constant testing speed of $0.2mm/min$ using a standard electromechanical testing machine (Inspect table 100, Hegewald& Peschke, Nossen/ Germany). The deformation of the adhesive in the butt joint tests was evaluated via a videoextensometer system (DCP 2.0, Limess, Krefeld/ Germany) with a resolution of about 600 x 200 pixels. Compared to an earlier publication of the author [68] the videoextensometer was found to give better results than the Aramis system (Version 6.3.0, GOM, Braunschweig/ Germany). Moreover, the clamping of the specimen in the butt joint test fixture was released. It was found, that the short free length of the butt joint specimen and a rigid clamping leads to an initial pre-stressing of the specimen. By releasing the clamping, better results in the quasi-static butt joint tests were found. The quasi-static test set-up with a butt joint specimen is shown in Fig. 3-3. Since the lap shear specimen had a greater free length, the clamping of the specimens in the test fixture did not show any influence for these specimens and the results are taken from [68]. The deformation in the lap shear tests was evaluated via DIC using a 4M Aramis system, with a resolution of 1728 x 2352 pixels. The frame rate to record the adhesive deformation in the butt joint test was 50 frames per second (fps) and in the lap shear test was 1 fps.

3.1.2 Results and discussion

The resulting stress-deformation curves of the quasi-static butt joint experiments are shown in Fig. 3-4 and of the quasi-static lap shear experiments in Fig. 3-5, respectively. The rate of deformation was approximately $3.0\mu m/s$ up to the specimen failure in both experiments. The values of mean stiffness, mean maximum stress and mean energy absorbed per bonding area are shown in table 3-1 with standard deviations. The stiffness has been evaluated in terms of a secant modulus up to half of the mean maximum stress for the butt joint and lap shear experiments. This method has been chosen in order to minimise inaccuracies at the origin of the

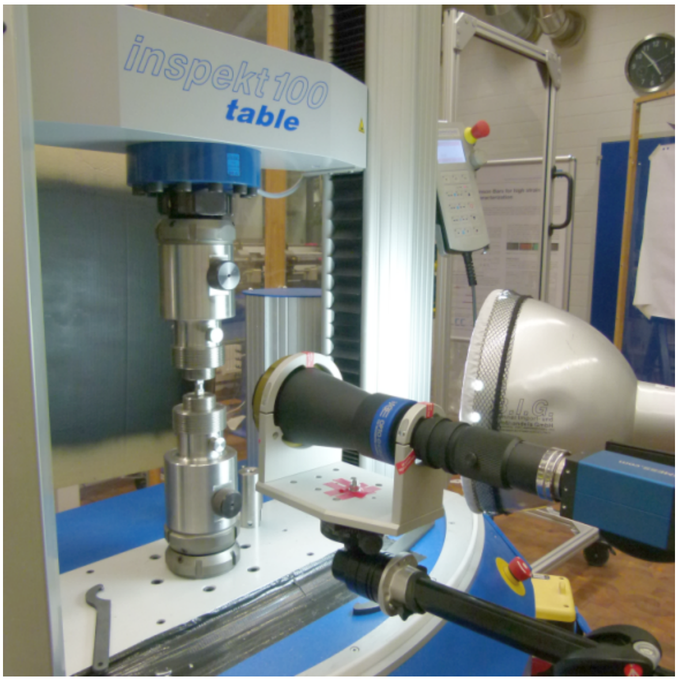

Figure 3-3 Quasi-static test set-up with a butt joint specimen.

stress-deformation curves and inaccuracies from non-linear effects at higher stress levels.

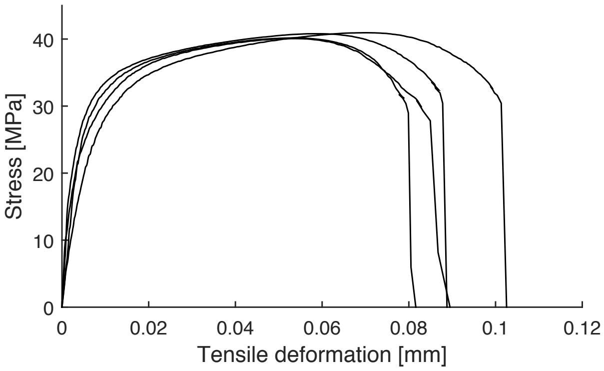

Figure 3-4 Stress-deformation curves of the butt joint test at quasi-static loading ($3.0 \mu m/s$) [68].

The fracture surface of a representative butt joint and lap shear specimen is shown in Figs. 3-6 and 3-7, respectively. It can be seen that a cohesive failure occurred in the adhesive bondline since the adherend surfaces are covered with adhesive material. The failure in the lap shear specimen occurred close to the adherend surface jumping from one adherend to the other in the middle of the overlap. Still a cohesive failure was assumed. Since cohesive failure was observed, the stress-deformation curves can be directly related to the cohesive behaviour of the adhesive.

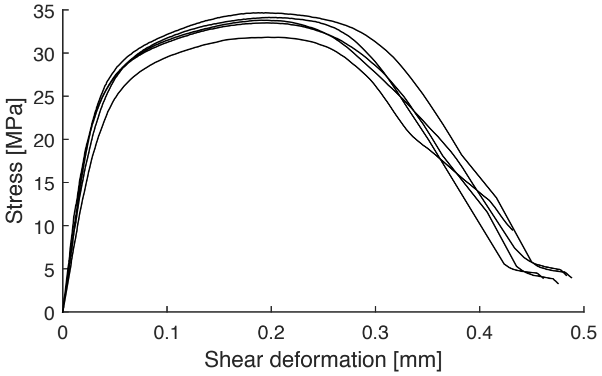

Figure 3-5 Stress-deformation curves of the lap shear test at quasi-static loading ($3.0 \mu m/s$) [68].

	Butt joint	Lap shear
Mean stiffness $[N/mm^3]$	6156 ± 1849	801 ± 93
Mean maximum stress $[MPa]$	40.49 ± 0.44	33.59 ± 1.07
Mean energy absorbed $[mJ/mm^2]$	3.21 ± 0.34	11.44 ± 0.63

Table 3-1 Mean properties (± standard deviation) of the butt joint and lap shear tests at quasi-static loading ($3.0 \mu m/s$).

The quasi-static butt joint tests showed good results in terms of the maximum stress of the adhesive. A high standard deviation was measured for the stiffness though. Additionally, the rate of deformation was not constant in the range of the stiffness evaluation. The measured mean value of the energy absorbed per bonding area is less affected by this inaccuracy since the main contribution is due to the stress plateau in the middle of the stress-deformation curves.

The lap shear tests showed that the stiffness as well as the maximum stress could be well determined. In the degradation part of the curves friction effects could imply some errors. Multiplying the stiffness measured in the butt joint and lap shear experiments by the bondline thickness, yields the apparent modulus E_a and

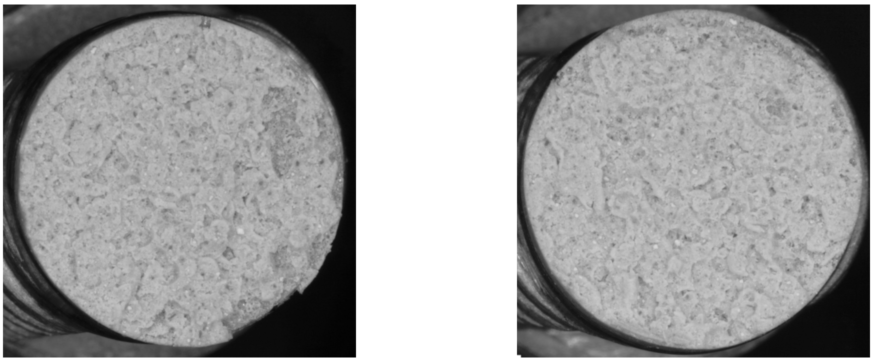

Figure 3-6 Fracture surface of a representative butt joint specimen.

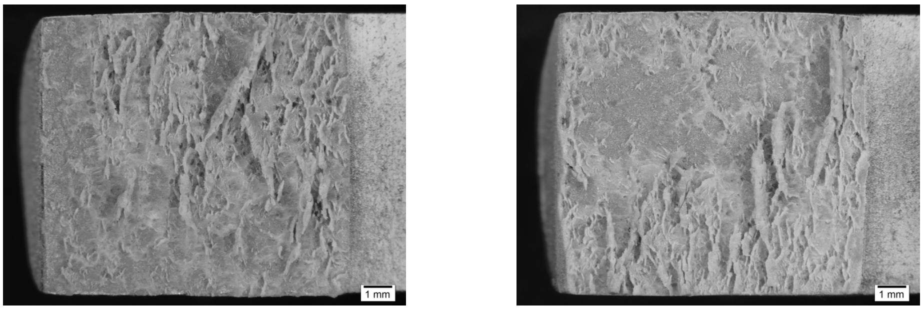

Figure 3-7 Fracture surface of a representative lap shear specimen.

shear modulus G. Then the Poisson ratio of both tests according to eq. (2-34) leads to $\nu = 0.42$ which is an appropriate value [11]. The quasi-static butt joint and lap shear tests will be used as a reference for other quasi-static and higher loading rate tests in section 3.5 and 3.6.

3.2 Quasi-static testing of the adhesive by the DCB test

The quasi-static characterisation of an adhesive bondline can be done by fracture mechanics tests evaluated with the J-integral introduced by Rice [90]. The J-integral is derived towards the crack opening displacement. The method was first published by Olsson and Stigh [91] using a DCB specimen to directly find the cohesive law in mode I. Sørensen [54] adapted this method for moment loading conditions. Andersson and Stigh [51] developed a theory called “thin layer theory” and applied it with success to some adhesives.

In this section, the mode I behaviour of the adhesive bondline is evaluated by DCB specimen. Using the derivation of Andersson and Stigh [51], the J-integral for the DCB specimen is given by

$$\mathbb{J}_I = 2\frac{F sin(\theta_{ld})}{w}. \tag{3-4}$$

where F denotes the force and θ_{ld} the rotation at the loading point during the test. w denotes the width of the specimen. The cohesive law $\tau_I(\delta_I)$ can be found by derivation

$$\tau_I(\delta_I) = \frac{d\mathbb{J}_I}{d\delta_I}. \tag{3-5}$$

where δ_I denotes the crack tip opening in mode I, which corresponds to the separation in mode I. The restriction to this data reduction scheme is, that the free bending arms of DCB specimen must obey the kinematics of a Bernoulli beam i.e.

the shear deformation of the beams must be negligible. Additionally, the deformation of the adherends needs to stay reversible.

3.2.1 Specimen manufacturing and testing

The specimen geometry is illustrated in Fig. 3-8. The adherends had a thickness of 2.0mm and were made out of the unidirectional (UD) prepreg Hexply® IM7-8552 (Hexcel, Stamford/Connecticut, United States) with a plane weave peel ply of 95g/m^2 (R&G, Waldenbuch, Germany) on the top and bottom surface. The adherends were manufactured stacking 20 plies with the same orientation adding the peel plies at the top and bottom. The laminate was cured in a hot press according to the manufacturer's guideline for 60min at 120°C and 120min at 180°C [92].

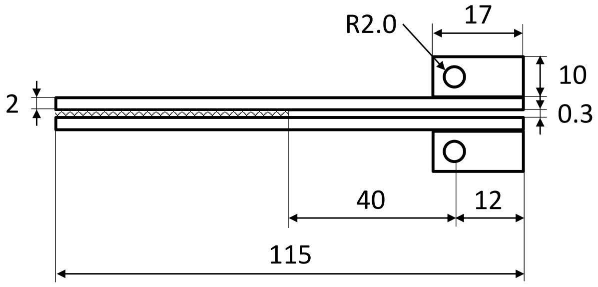

Figure 3-8 DCB specimen geometry.

The plates were cut after curing with a water cooled diamond blade saw to remove the poured out resin. For bonding, the peel plies were removed and the adhesive was applied to the bonding surface by a glue gun according to Fig. 3-9. The adhesive thickness of 0.3$mm \pm 0.05mm$ was guaranteed by sharpened steel shims which were coated with Loctite® Freekote 770NC (Henkel, Düsseldorf, Deutschland) to enable the removal of the shim after curing. The fixation of the plates and the shims was done with the help of short pins inserted into the plate. The initial crack length was defined to be 20mm.

The adhesive was cured in an hot press according to the manufacturers guideline for 30min at 180°C. Then, the pins and shims were removed. With the water cooled diamond blade saw, the bonded plates were cut perpendicular to the crack front into strips of nominally 20mm width. Then aluminium loading blocks were bonded on the top and bottom of the loading arms. A representative DCB specimen is shown in Fig. 3-10. Before testing, a speckle pattern was sprayed on the specimen. The speckle pattern was used for later post-processing via DIC to measure the rotation θ_{ld} of the loading point and the normal separation δ_I.

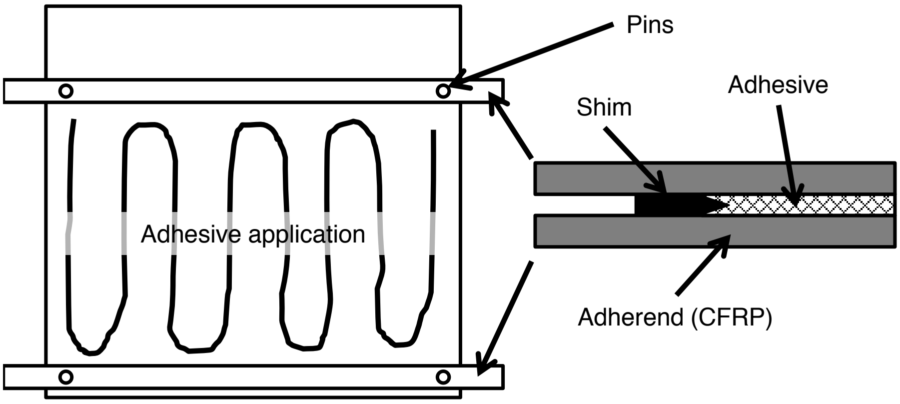

Figure 3-9 Application of adhesive (left) and shims to guarantee the adhesive thickness (right).

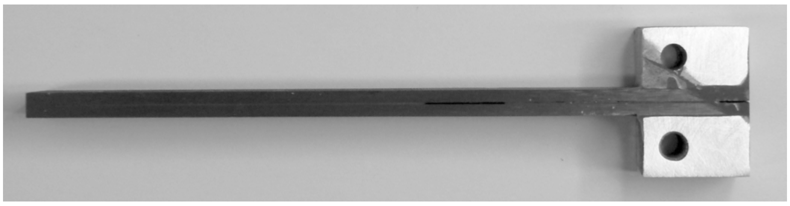

Figure 3-10 Representative DCB specimen.

The specimen were tested in the electromechanical testing machine as shown in Fig. 3-11 (left). In order to constantly deform the adhesive layer at the crack tip, the speed of the testing machine was defined decreasing. Four DCB specimen were tested. Fig. 3-11 (right) illustrates the DIC post-processing of a representative DCB specimen via the Aramis system.

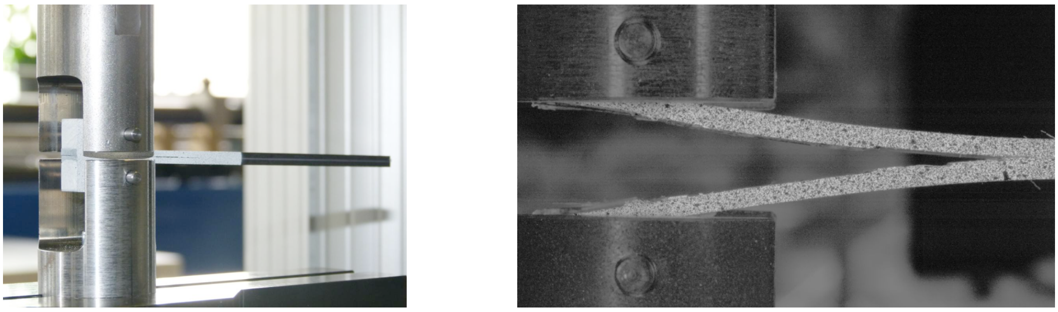

Figure 3-11 Testing of a DCB specimen in the electromechanical testing machine (left) and DIC post-processing (right).

3.2.2 Results and discussion

The results of the DCB tests in terms of a traction-separation relation are shown in Fig. 3-12. The deformation rate was found to be constant up to the maximum traction at a level of $1.0 \mu m/s$. In the degradation part of the cohesive law the deformation rate increased up to about $4.0 \mu m/s$. The stiffness of the curve was evaluated in terms of a secant stiffness at half of the mean maximum stress. This method has been chosen in order to minimise inaccuracies at the origin of the cohesive laws and inaccuracies from non-linear effects. The mean secant stiffness of the cohesive law resulted in $9206 N/mm^3$ with a standard deviation of $3164 N/mm^3$. The mean maximum traction was $45.32 MPa$ with a standard deviation of $2.26 MPa$. The mean maximum J-integral of the DCB specimen was $3.23 mJ/mm^2$ with a standard deviation of $0.18 mJ/mm^2$.

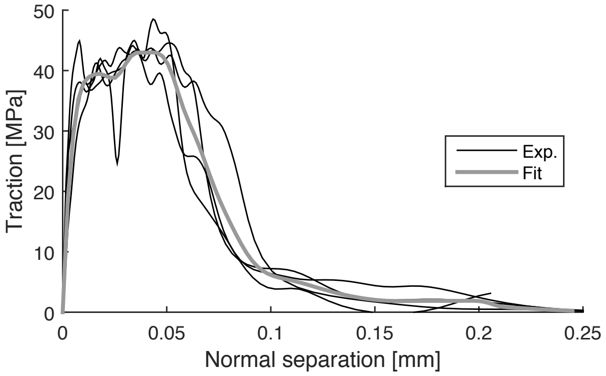

Figure 3-12 Cohesive law of the adhesive in mode I at a deformation rate of $1.0 \mu m/s$.

After testing, the fracture surfaces of the crack were investigated. Fig. 3-13 shows both adherend surfaces of a representative specimen. The measured cohesive laws are a representation of the crack tip of the fracture surfaces, since no crack propagation was accounted for in the evaluation. There, a cohesive failure was detected due to adhesive material on both sides of the crack. Moreover it is worth noticing, that the deformation of the CFRP adherends was in the elastic range.

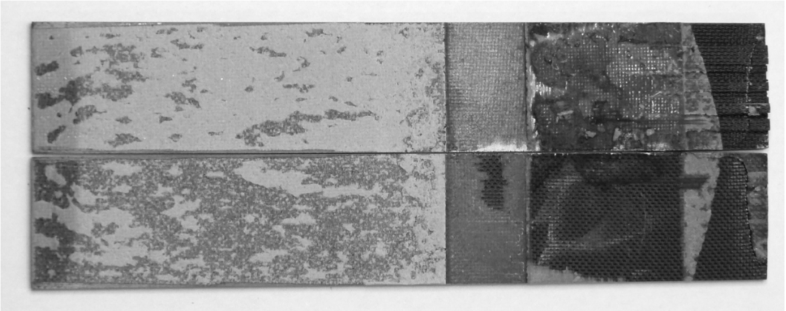

Figure 3-13 Fracture surface of a DCB specimen.

The results obtained from the DCB tests evaluated with the J-integral method lead to the complete definition of the cohesive law in mode I of the adhesive. Although the maximum tractions showed a low standard deviation, significant oscillations in the measured curves of Fig. 3-12 could be seen. These oscillations were due to the calculation of the J-integral derivation towards the normal separation according to eq. (3-5). The value of the J-integral was unaffected by these inaccuracies, however the maximum stress and stiffness of the adhesive bondline could bear errors. In order to reduce the oscillation effects, the experimental curves were fitted by a spline fit as shown in Fig. 3-12.

The results of the DCB specimen compared to the butt joint tests are shown in Fig. 3-14. Fig. 3-15 shows the evaluation of stiffness, strength and fracture energy including standard deviations. The mean stiffness of the DCB tests is higher than in the butt joint experiments but shows a large standard deviation. Using the spline fit, the oscillations can be compensated. The stiffness of the fitted DCB results within the standard deviation of the butt joints. The difference comparing the maximum stress and maximum traction is due to the oscillations in the cohesive law and the different stress state. Again, the spline fit compensates for the oscillations and shows that the results of butt joint and DCB test are better correlated. Sørensen

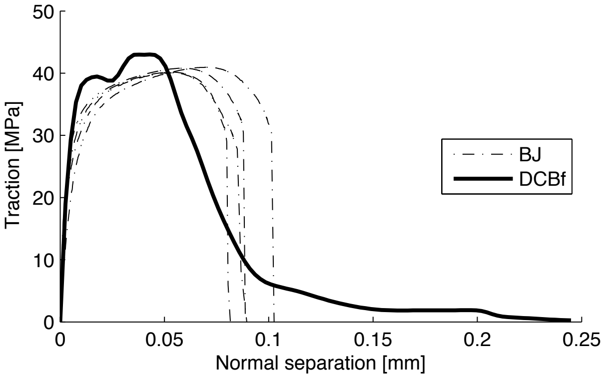

Figure 3-14 Comparison between the curves from the butt joint tests (BJ) at a deformation rate of $3.0\mu m/s$ and the spline fitted DCB tests (DCBf) at a deformation rate of $1.0\mu m/s$.

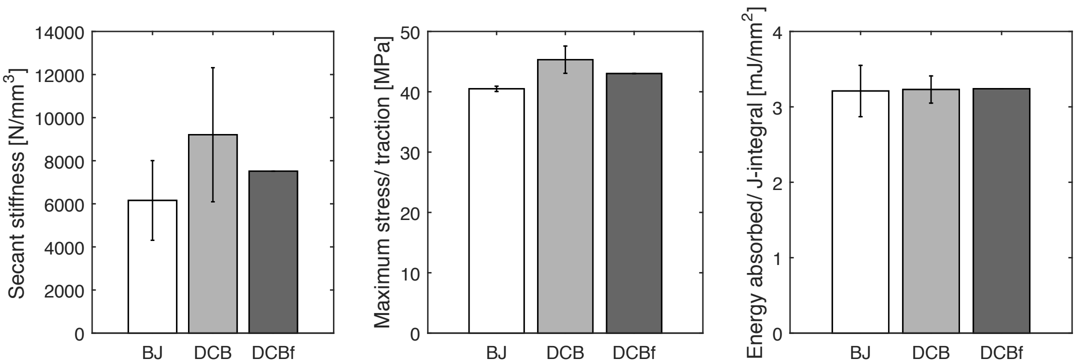

Figure 3-15 Comparison of secant stiffness, maximum stress and energy absorbed per bonding area between quasi-static butt joint tests (BJ) and raw and spline fitted DCB tests (DCB/ DCBf).

[54] also compared the strength of butt joint and the DCB test results and found a good correlation for the adhesive investigated. The energy absorbed per bonding area approximates well the maximum J-integral which corresponds to the fracture energy of the adhesive in mode I. The results of the DCB tests show, that the cohesive law found can well be approximated by the butt joint tests.

3.3 Quasi-static testing of the adhesive by the ENF test

For the ENF-specimen, Stigh et al. [55] found the following expression for the calculation of the J-integral.

$$\mathbb{J}_{II} = \frac{F}{2w} \left[sin(\theta_{sup1}) - 2sin(\theta_{ld}) + sin(\theta_{sup2}) \right] \tag{3-6}$$

Here, θ_{sup1} and θ_{sup2} are the clockwise rotations of the ENF specimen at the supports. θ_{ld} is the clockwise rotation of the ENF specimen at the load introduction point, which is in the middle between the supports. The cohesive law $\tau_{II}(\delta_{II})$ for the adhesive is calculated by derivation of the J-integral $\mathbb{J}_{II}$ towards the crack tip opening in shear direction, which is the separation in mode II δ_{II}.

$$\tau_{II}(\delta_{II}) = \frac{d\mathbb{J}_{II}}{d\delta_{II}} \tag{3-7}$$

3.3.1 Specimen manufacturing and testing

Fig. 3-16 shows the geometry of the ENF-specimen used for characterisation of the quasi-static behaviour of the adhesive bondline in shear direction. The specimens were manufactured by the same methodology as for the DCB specimen outlined in the section 3.2. The adherend thickness was $2.0mm$, the adhesive thickness $0.3mm$ ± $0.05mm$, the width of the specimen was $10mm$ and the initial crack length $20mm$, respectively. No loading blocks were attached to the adherends in this case. A representative specimen is shown in Fig. 3-17.

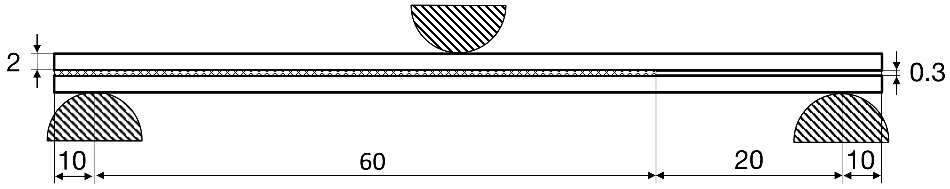

Figure 3-16 Geometry of an ENF specimen.

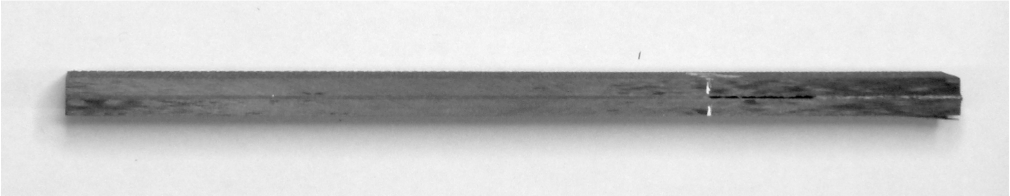

Figure 3-17 Representative ENF specimen.

The specimen were placed into a three-point bending device of the electromechanical testing machine as shown in Fig. 3-18 (left). The testing speed at the testing machine was defined decreasing to enable a constant loading of the adhesive at the crack tip. The DIC evaluation of the ENF specimen is shown in Fig. 3-18 (right).

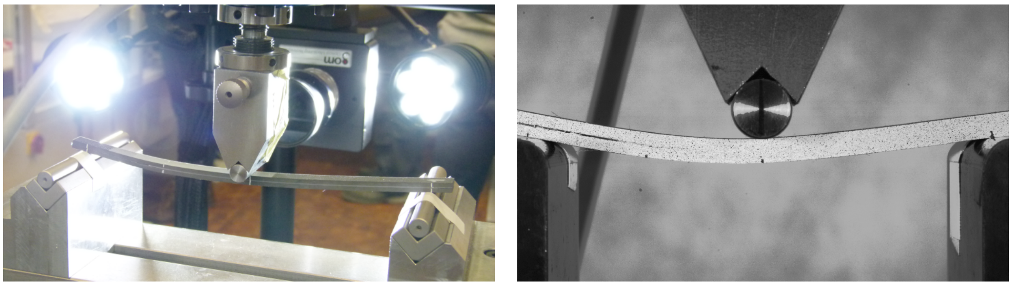

Figure 3-18 Testing of an ENF specimen in the electromechanical testing machine (left) and DIC post-processing (right).

3.3.2 Results and discussion

Five ENF specimen were tested. The cohesive laws are shown in Fig. 3-19. The secant stiffness evaluated at half of the mean maximum stress was $1428 N/mm^3$ with a standard deviation of $438 N/mm^3$. The mean maximum traction measured was $42.93 MPa$ with a standard deviation of $1.92 MPa$. The mean maximum J-integral was $9.27\ mJ/mm^2$ with a standard deviation of $0.40 mJ/mm^2$. The rate of crack tip opening displacement was $3.0 \mu m/s$ and approximately constant over the complete cohesive law. The fracture surface of a representative ENF specimen is shown in Fig. 3-20. At the crack tip, the failure occurred close to adherend surface but still cohesive failure is assumed since adhesive material was found on both surfaces.

The comparison between the lap shear tests and the ENF tests is shown in Fig. 3-21 while Fig. 3-22 gives a comparison between stiffness, strength and fracture energy with standard deviations. It can be seen, that the stiffness as well as the strength of the cohesive law is higher than the results of the lap shear tests while the mean maximum J-integral of the ENF tests is lower than the energy absorbed per bonding area in the lap shear tests. Problematic in the measurement of the crack

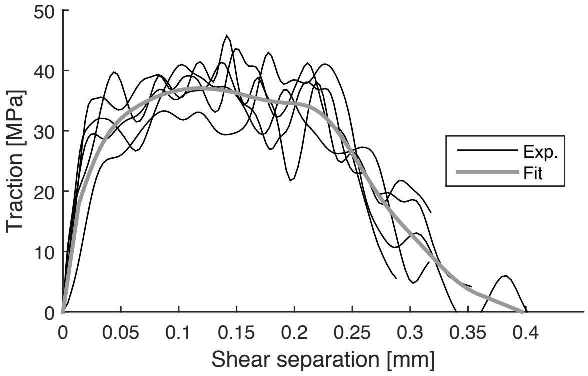

Figure 3-19 Cohesive law of the adhesive in mode II at a deformation rate of $3.0 \mu m/s$.

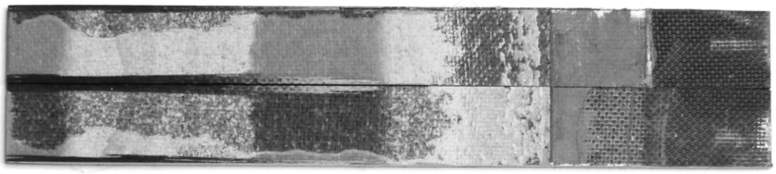

Figure 3-20 Fracture surface of an ENF specimen.

tip opening is, that the position of the crack front could not be defined precisely in the ENF specimen. This was found to strongly influence the stiffness and the magnitude of the tractions. Additionally, the derivation of the J-integral towards the crack tip opening according to eq. (3-7) lead to a large scatter in the cohesive laws, which can be seen in the standard deviation of the cohesive law stiffness. The mean maximum traction was therefore elevated using a spline fit of the measured curves. The maximum J-integral in the ENF tests could be affected by the short specimen length. Then the fracture process zone of the crack can grow under the loading point influencing the experimental results.

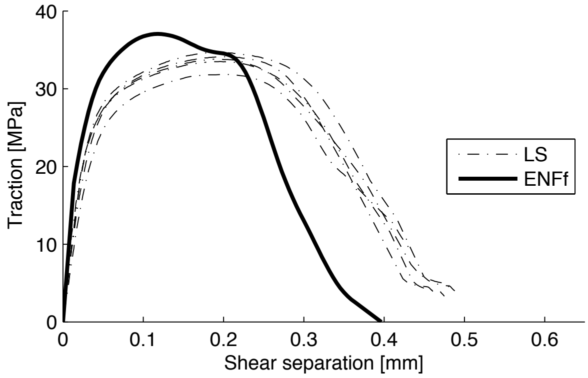

Figure 3-21 Comparison between the curves from the lap shear tests (LS) and the spline fitted ENF tests (ENFf) at a deformation rate of $3.0 \mu m/s$.

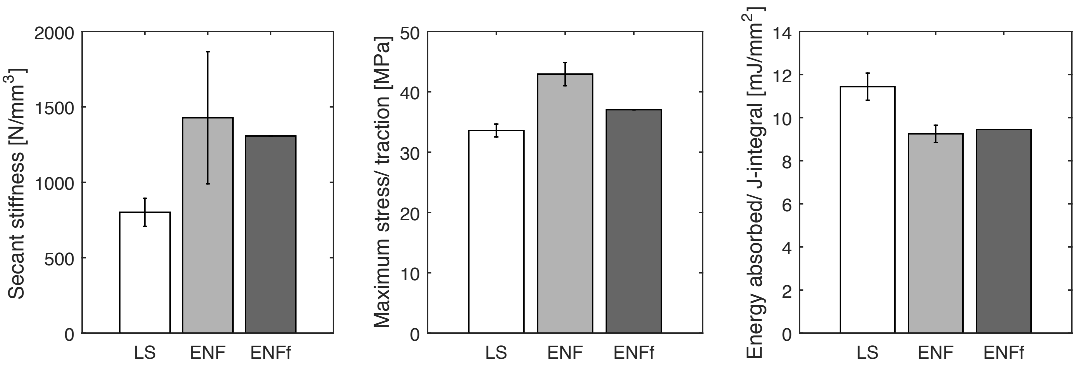

Figure 3-22 Comparison of secant stiffness, maximum stress and energy absorbed per bonding area between quasi-static lap shear tests (LS) and raw and spline fitted ENF tests (ENF/ ENFf).

3.4 Testing of the adhesive under combined loading

The quasi-static behaviour of the adhesive was characterised in normal mode loading by the butt joint and the DCB test and in shear mode loading by the lap shear and the ENF test. The combination of normal and shear loading is characterised in this section.

3.4.1 Specimen manufacturing and testing

The specimen geometry used is a tensile test of a bonded joint with inclined adhesive bondline i.e. a scarf joint. The geometry is shown in Fig. 3-23.

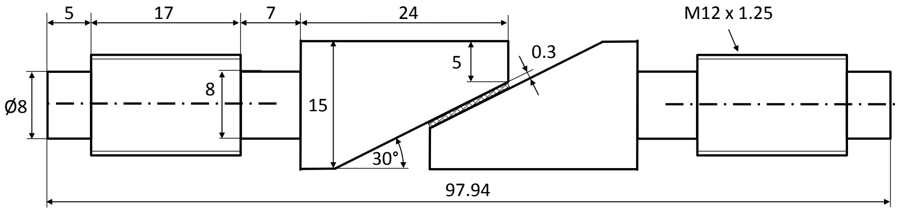

Figure 3-23 Geometry of the combined loading specimen.

The adherends were made of stainless steel and grit-blasted with glass spheres with a diameter of $180\mu m$ to $200\mu m$ before bonding. With the help of custom made shims and a bonding jig, the bondline thickness of $0.3mm \pm 0.05mm$ could be achieved. The bonding area was $9.2mm$ x $15mm$. All specimens were cured in an oven at $180°C$ for $30min$ in accordance with the manufacturer's guideline. For the deformation measurement of the combined loading specimen a black-on-white speckle pattern was sprayed on the specimens for later DIC measurement. Markers were attached additionally to enable a calibration of the distance-to-pixel ratio of the images. A representative specimen is shown in Fig. 3-24.

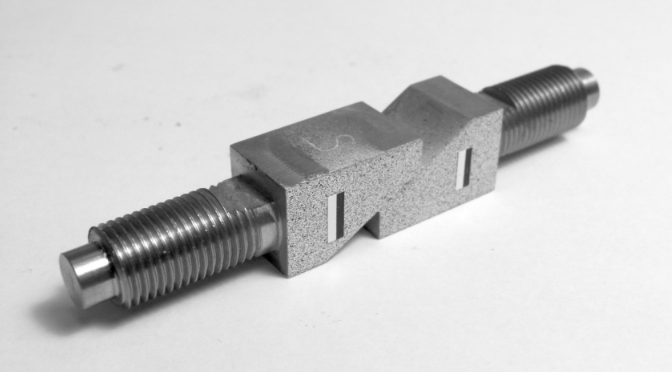

Figure 3-24 Representative specimen of the combined loading test.

Five quasi-static tests were performed at a constant testing speed of $0.2mm/min$ using the standard electromechanical testing machine. The deformation of the adhesive in the combined loading tests was evaluated via the 2D Aramis software. The rate of record was 2 fps with a resolution of 1232 x 472 pixels. With the help of the DIC analysis, it was found that the tested adhesive deformation was approximately 15° instead of 30° given from the design of the specimen. The adhesive stress was calculated according to eq. (3-1).

3.4.2 Results and discussion

The deformation rate of the adhesive was approximately constant at $1.0\mu m/s$ up to the maximum stress. Then the deformation rate increased up to $8.0\mu m/s$. Fig. 3-25 shows the stress-deformation curves of the combined loading tests. The secant stiffness was evaluated at the half of the mean maximum stress and resulted in a mean value of $733N/mm^3$ with a standard deviation of $127N/mm^3$. The mean maximum stress was $33.18MPa$ with a standard deviation of $0.70MPa$. The mean energy absorbed per bonding area was $8.75mJ/mm^2$ with a standard deviation of $0.63mJ/mm^2$.

A view of the crack surface of the combined loading test is shown in Fig. 3-26. It can be seen that most parts of the adherend surfaces are covered with adhesive material. A cohesive failure is, therefore, observed. Some amount of voids can also be seen within the bonding area reducing the strength of the bondline.

A comparison of the secant stiffness, the maximum stress and the energy absorbed per bonding area with the butt joint and lap shear tests can be seen in Fig. 3-27. The secant stiffness and maximum stress is lower in the scarf joint test than both other

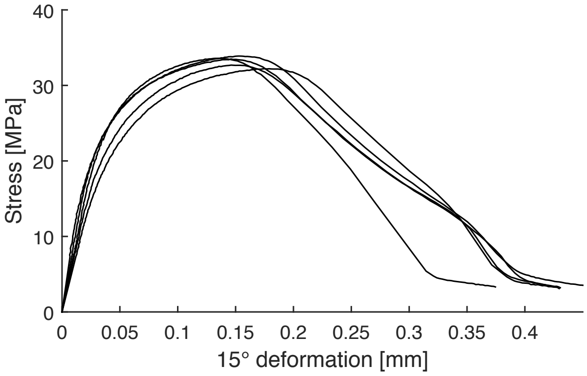

Figure 3-25 Stress-deformation curves of the combined loading tests at a deformation rate of $1.0\mu m/s$.

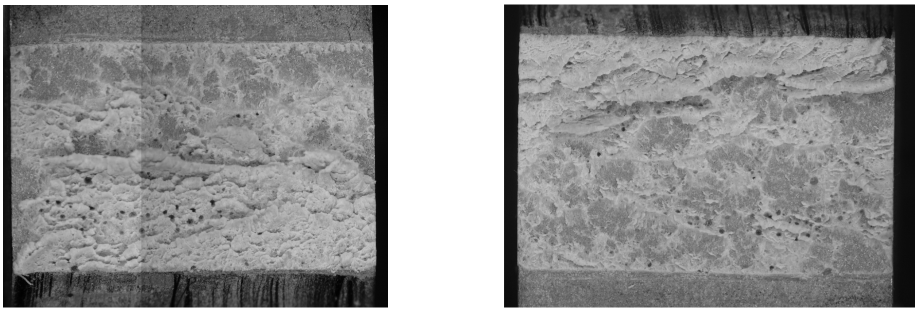

Figure 3-26 Crack surface of the combined loading specimen.

tests while similar to the lap shear test in each case. The energy absorbed is well in between the butt joint and the lap shear test. A linear variation of the fracture energies has been shown by many other publications [40, 60, 93]. Estimating the energy absorbed per bonding area for the scarf joint by a linear variation using the energy absorbed per bonding area of the butt joint and lap shear specimen yields

$$En.\ abs.^*_{BJ,LS} = \frac{3.21\frac{mJ}{mm^2} - 11.44\frac{mJ}{mm^2}}{90^\circ}15^\circ + 11.44\frac{mJ}{mm^2} = 10.07\frac{mJ}{mm^2}. \tag{3-8}$$

Using the fracture energies in terms of the maximum J-integral of the DCB and ENF specimen yields

$$En.\ abs.^*_{DCB,ENF} = \frac{3.23\frac{mJ}{mm^2} - 9.27\frac{mJ}{mm^2}}{90^\circ}15^\circ + 9.27\frac{mJ}{mm^2} = 8.26\frac{mJ}{mm^2} \tag{3-9}$$

The measured value of $8.65mJ/mm^2$ correlates well with the estimated values and agrees with the theory. The results are used in chapter 5 for the evaluation of the mixed-mode cohesive behaviour of the adhesive.

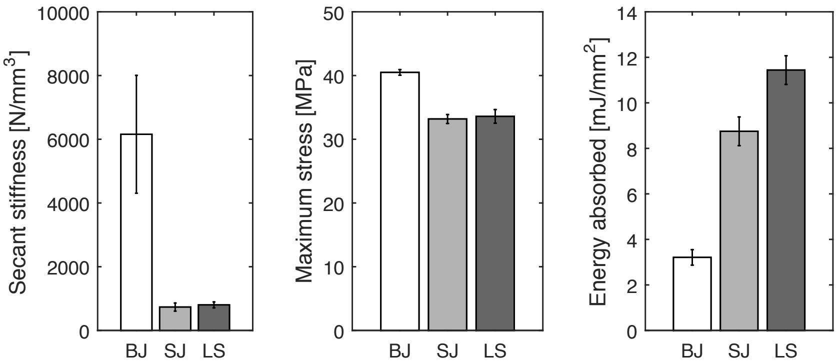

Figure 3-27 Comparison of secant stiffness, maximum stress and energy absorbed per bonding area between quasi-static butt joint (BJ), scarf joint (SJ) and lap shear (LS) specimen.

3.5 Intermediate-rate testing of the adhesive with butt joint tests

Five butt joint specimen described section 3.1 were tested by a speed of $20mm/min$ in the electromechanical testing machine. At this speed, inertia effects in the force measurement were found to be low and a proper data acquisition with the videoextensometer was possible. The record rate was 100 fps at a resolution of 536 x 88 pixels. About 80 data points could be measured during a single test.

Fig. 3-28 shows the stress-deformation curves of the intermediate-rate tests. The deformation rate measured by the videoextensometer resulted in approximately $0.2mm/s$. The mean secant stiffness measured at half of the mean maximum stress was $7821N/mm^3$ with a standard deviation of $3911N/mm^3$. The mean maximum stress was $47.58MPa$ with a standard deviation of $1.05MPa$. The mean energy absorbed per bonding area in the experiments was $3.00mJ/mm^2$ with a standard deviation of $0.32mJ/mm^2$. The inspection of the fracture surfaces lead to a similar surface like in Fig. 3-6. A cohesive failure of the bond was, therefore, assumed.

The deformation rate in the butt joint experiments was increased about a factor of 10^2. A comparison of the test results from quasi-static and intermediate-rate tests for the butt joint specimens is shown in Fig. 3-29. The secant stiffness increased by a factor of 1.27 with increasing deformation rate. The standard deviation is, however, very high for the intermediate-rate tests. The increase is not statistically significant. The mean strength increased by a factor of 1.18. The energy-absorbed per bonding area decreased by a factor of 0.93 but the difference is still within the standard deviations of both tests. A statistically significant rate effect can only be stated for the strength. The results are used in chapter 5 for the calibration of the rate-dependent cohesive behaviour of the adhesive.

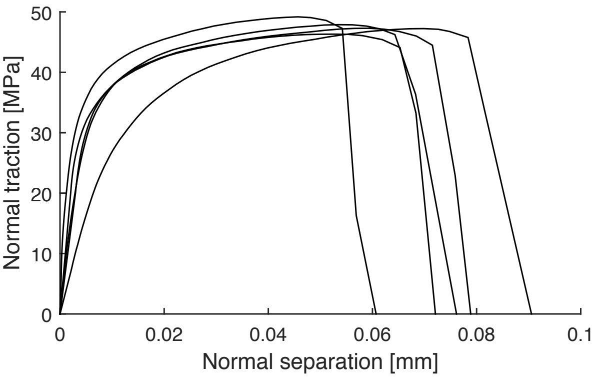

Figure 3-28 Stress-deformation curves of the butt joint tests at intermediate-rate loading ($0.2 mm/s$).

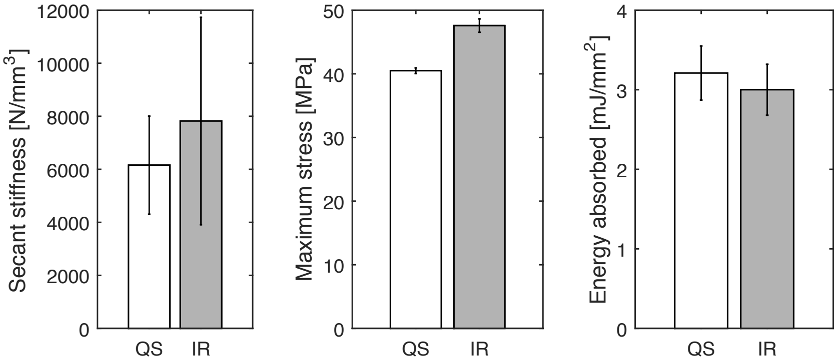

Figure 3-29 Comparison of secant stiffness, maximum stress and energy absorbed per bonding area between quasi-static (QS) and intermediate-rate (IR) butt joint tests.

3.6 High-rate testing of the adhesive with butt joint and lap shear specimen

The high-rate mechanical behaviour of the adhesive bondline is investigated in this section using a tensile SHB set-up. Furthermore, as outlined in section 2.3.4, it is investigated in how far the measurement of deformations can influence the test results. Some contents in this section have been taken from a previous publication of the author [68].

Generally, two sources of inaccuracies can arouse for measuring the bondline deformations in high-rate experiments with the tensile SHB set-up: Firstly, the deformation of the adherends must be taken into account and, secondly, the deformation of the bar ends calculated by SHBA can bear errors. Some studies did not account for the possibility of errors in the deformation measurement and used the classical SHBA for the evaluation of specimen deformations [94, 95]. Challita et al. [84] could compensate for the errors from the adherends' deformation. They simulated the specimens in FE studies and found correction factors. The errors coming from SHBA, however, still remained. Sugaya et al. [96] performed dynamic tests on adhesive bulk specimens and could measure the adhesive strain up to necking of the bulk material with strain gauges. However, strain gauges are difficult to apply to thin bondlines. Most recent studies used laser optical methods to measure the joints' displacement [97, 98]. Marzi et al. used a three-dimensional (3D) DIC method to measure the displacements of a dynamically loaded T-peel joint in a rotary impact device [99]. A comparison between a deformation measurement of bonded joints by SHBA and DIC for tensile SHB set-ups is outlined in the following.

3.6.1 Specimen manufacturing and testing

High-rate tests using the same specimen geometry as described in section 3.1 were conducted on a tensile SHB system (see Fig. 3-30). This set-up is based on a design proposed by Gerlach et al. [100] utilising a U-type striker bar with a length of 500 mm and a mass of $918.5g$. The striker bar was accelerated up to an average velocity of $V_0 = 4.45m/s$. A loading bar with a diameter of $20mm$ transferred the elastic wave to the incident bar. The incident bar had a length of $2800mm$ and the transmission bar had a length of $1800mm$. Both were made of titanium and had a diameter of $16mm$. A first strain gauge terminal on the incident bar was attached at a distance of $1600mm$ from the incident bar end, where the specimen was fixed. It captured the incident wave and the reflected wave. A second strain gauge terminal was attached to capture the transmitted wave at a distance of $200mm$ away from the specimen on the transmission bar. The wave signals were amplified and recorded by an oscilloscope. Additionally, the deformation of the adhesive was recorded using a Photron SA 5 high-speed camera (Photron, Tokyo, Japan) at a frame rate of 150 000 fps and a resolution of 156 x 144 pixels. The high-speed camera images were then post-processed to evaluate the deformation of the adhesive via DIC. The location of measurement in the butt joint and lap shear specimen is shown in Fig. 3-31.

In total, four butt joint specimens and five lap shear specimens were tested. Representative raw strain signals of the strain gauge terminal $\epsilon_{0,inc}$ and $\epsilon_{0,tra}$ are shown for an butt joint specimen in Fig. 3-32 (left) and an lap shear specimen in Fig. 3-32 (right), respectively. The rate of data record was $10^6 Hz$. All measured signals were subsequently filtered by a second order Butterworth filter to reduce digitalisation noise coming from the oscilloscope recording. Care was taken not to change the basic strain signal.

The strain signals were shifted according to eqs. (2-36) to (2-38) and are illustrated in Fig. 3-33. The forces acting on the end of incident F_{inc} and transmission bar F_{tra}

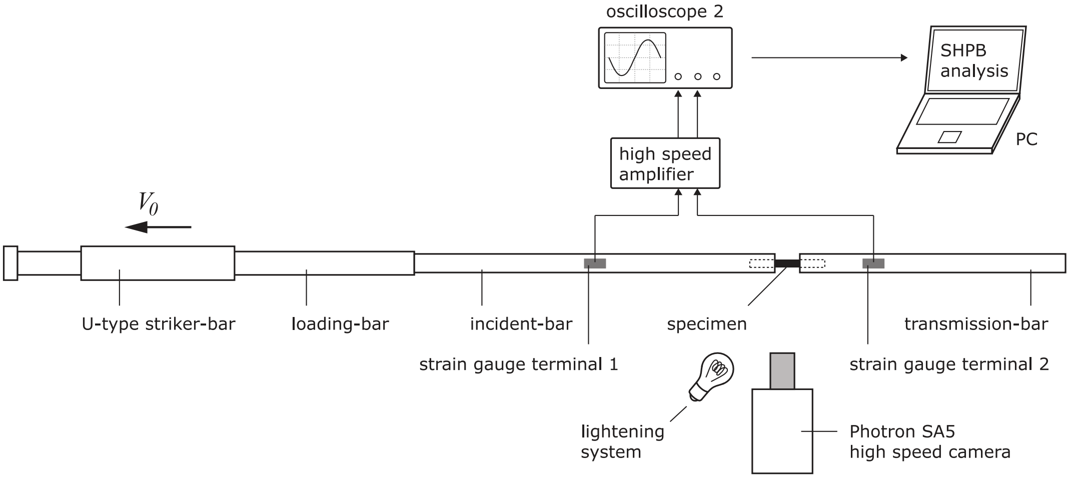

Figure 3-30 Set-up of the tensile SHB system [68].

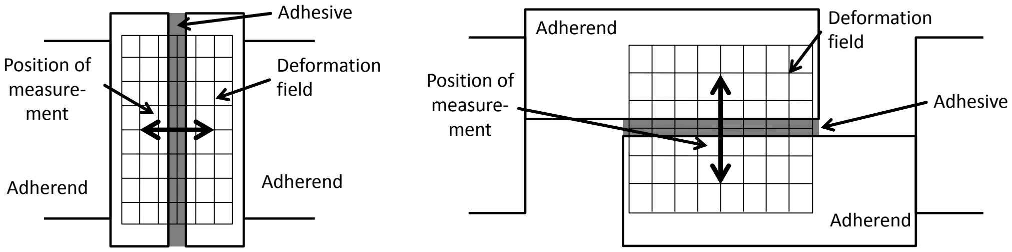

Figure 3-31 DIC measurement of adhesive deformation: butt joint test (left) and lap shear test (right) [68].

were calculated by eqs. (2-46) and (2-47) and are shown in Fig. 3-34. It can be seen that, for both specimen configurations, a dynamic force equilibrium is present. In order to get the stress in the adhesive, the clearer force signal F_{tra} is used in the following.

The DIC measurement of representative specimens from high-rate tests are shown in Fig. 3-35. It can be seen that the speckle pattern on the specimens was well identified by the DIC measurement system and the complete deformation field could be created by the software. Fig. 3-36 shows the resulting stress-deformation

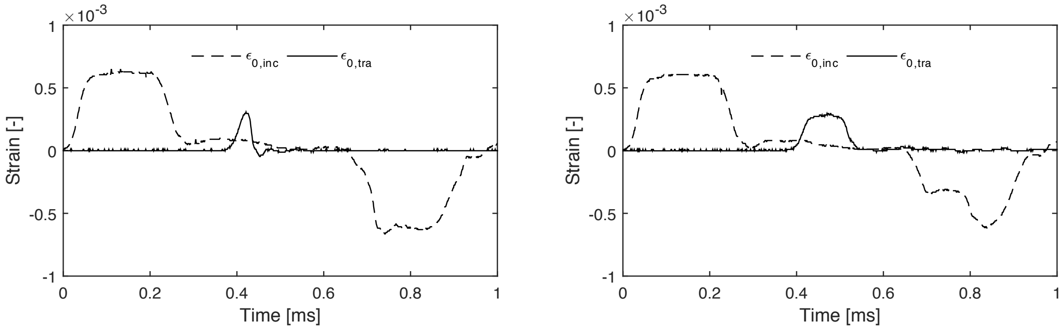

Figure 3-32 Bar strain gauge signals (raw): butt joint test (left) and lap shear test (right) [68].

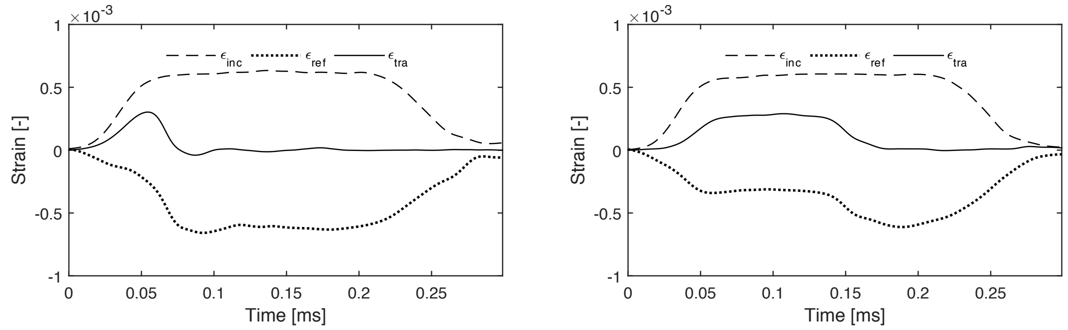

Figure 3-33 Filtered and shifted bar strain gauge signals: butt joint test (left) and lap shear test (right).

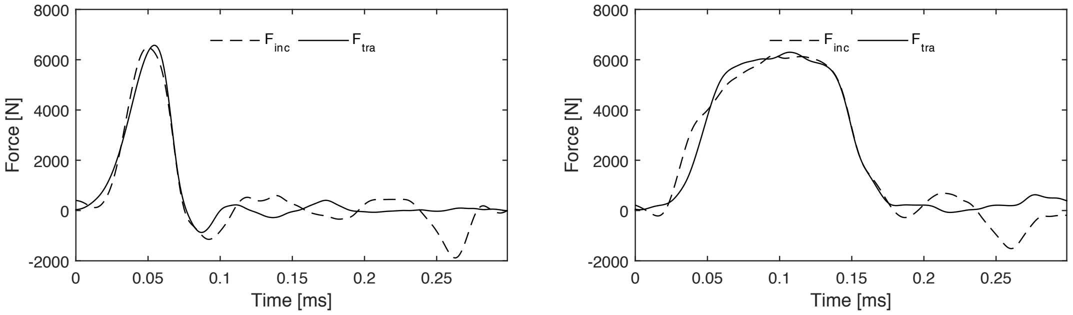

Figure 3-34 Force signals: butt joint test (left) and lap shear test (right) [68].

curves for butt joint and lap shear specimens showing the effect of deformation measurement by SHBA according to eq. (2-44) and DIC. It can be seen that the DIC measurement has a significant effect on the measurement of the deformation signal of the butt joint specimen and the lap shear specimen.

3.6.2 Results and discussion

The butt joint test results are shown in Fig. 3-37. The deformation was not constant during the test. At the point of maximum stress the deformation rate of the joint

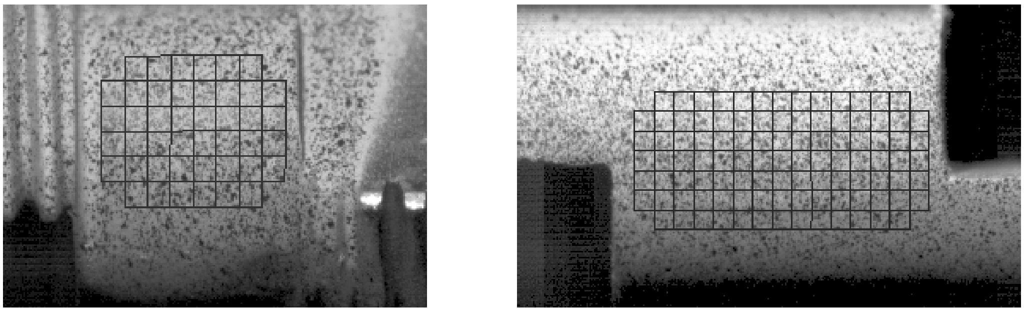

Figure 3-35 Speckle pattern and DIC deformation field of a butt joint specimen (left) and a lap shear specimen (right) [68].

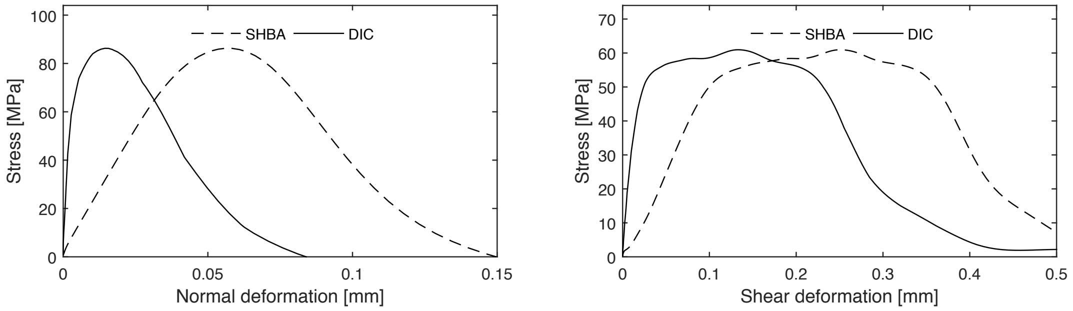

Figure 3-36 Deformation measurement based on SHBA and DIC: butt joint test (left) and lap shear test (right) [68].

was approximately $1.0 m/s$. In the lap shear tests, a constant rate of deformation of approximately $3.0 m/s$ could be observed up to the softening part of the stress-deformation curves. Then the deformation rate increased up to $8.0 m/s$. The test results are shown in Fig. 3-38. The mean secant stiffness, the mean maximum stress and the mean energy absorbed per bonding area are listed for both tests with standard deviations in table 3-2.

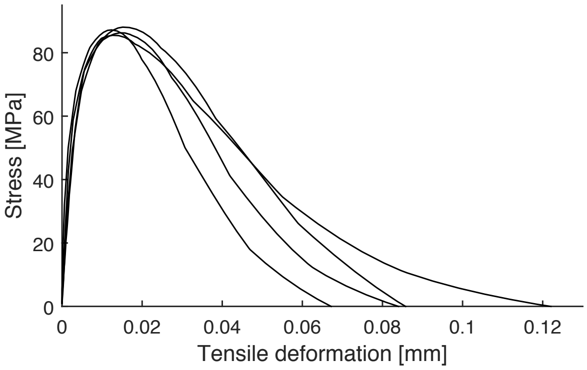

Figure 3-37 Stress-deformation curves of the butt joint test at high-rate loading ($1.0 m/s$) [68].

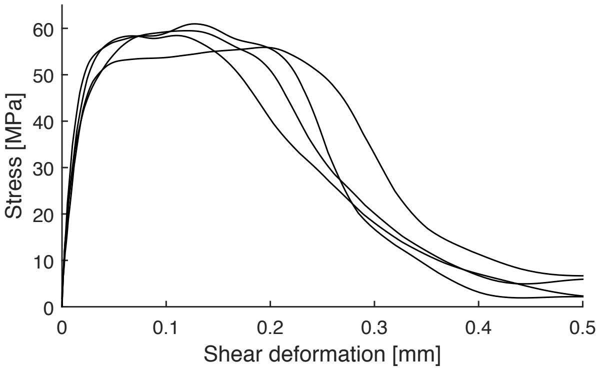

Figure 3-38 Stress-deformation curves of the lap shear test at high-rate loading ($3.0 m/s$) [68].

	Butt joint	Lap shear
Mean stiffness $[N/mm^3]$	25044 ± 8102	2925 ± 193
Mean maximum stress $[MPa]$	86.75 ± 1.12	58.70 ± 2.13
Mean energy absorbed $[mJ/mm^2]$	3.72 ± 0.62	16.13 ± 1.19

Table 3-2 Mean properties (± standard deviation) of the butt joint and lap shear experiments at high-rate loading using DIC measurement.

Now, the effect of deformation measurement in the high-rate tests is focused. Evaluating the deformation based on SHBA according to eq. (2-44) leads to a mean secant stiffness of $2026 N/mm^3 \pm 523 N/mm^3$ for the butt joint tests. This is lower than the secant stiffness obtained from quasi-static tests which is illustrated in Fig. 3-39. The secant stiffness evaluated using DIC is 12.4 times higher. The energy absorbed during the high-rate tests evaluated using SHBA is $6.85 mJ/mm^2 \pm 0.26 mJ/mm^2$. This means that the DIC measurement resulted in an absorbed energy of 0.55 times than that obtained by SHBA evaluation. Comparing the test results from quasi-static and high-rate tests for the butt joint specimens, the secant stiffness increased by a factor of 4.07 with increasing deformation rate. The mean strength increased by a factor of 2.14. The energy-absorbed per bonding area increased by a factor of 1.16. The deformation rate in the butt joint experiments was increased about a factor of 10^6.

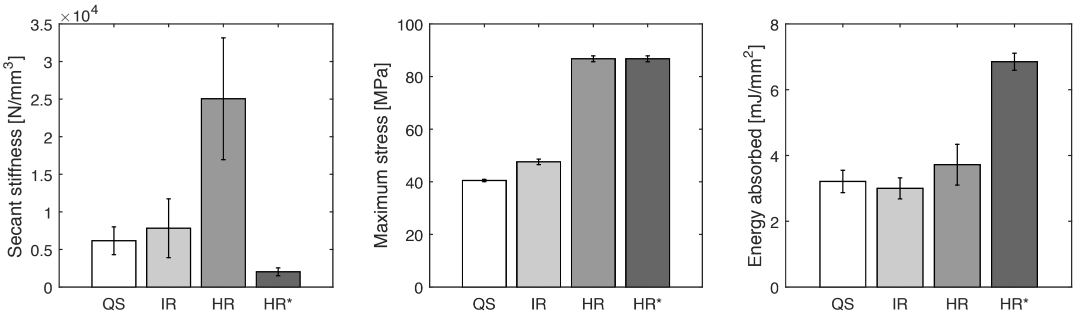

Figure 3-39 Comparison of secant stiffness, maximum stress and energy absorbed per bonding area between quasi-static (QS), intermediate-rate (IR) and high-rate butt joint tests using DIC (HR) and SHBA (HR*).

In the lap shear specimen the mean secant stiffness was $475 MPa \pm 40 MPa$ when SHBA was used for determination of the adhesive deformation. The secant stiffness evaluated using DIC is 6.16 times higher than that obtained using SHBA. The results are illustrated in Fig. 3-40. The mean energy absorbed by SHBA is $21.38 mJ/mm^2 \pm 1.50 mJ/mm^2$. This means the energy absorbed using DIC was 0.75 times the energy absorbed using SHBA. The approximate increase in deformation rate in the lap shear tests was about 10^6. The mean secant stiffness increased in the shear direction by a factor of 3.65 and the mean strength in the shear direction increased by a factor of 1.75 compared with the static experiments. The mean energy-absorbed in the lap shear tests increased by a factor of 1.41.

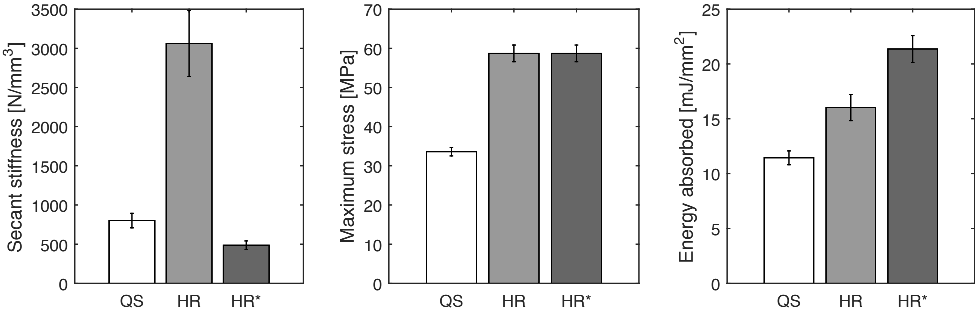

Figure 3-40 Comparison of secant stiffness, maximum stress and energy absorbed per bonding area between quasi-static (QS) and high-rate lap shear tests using DIC (HR) and SHBA (HR*).

A positive rate effect was shown on the mechanical properties in the tensile as well as the shear direction of adhesively bonded joints. These results are well in agreement with other publications [70, 75, 82]. However, inaccuracies in high-rate tests in the deformation measurement are apparent, which can be either due to the experimental set-up or the adherends' deformations. In [68], it was shown by a numerical study that the adherends used in this study have a minor influence on the stress-deformation relation measured in the high-rate tests of the butt joint and lap shear specimen. Inaccuracies in the deformation measurement could, therefore, be traced back to the experimental set-up. Those inaccuracies could be overcome by measuring the adherend deformation directly at the specimen by high-speed imaging and DIC. This means that using DIC significantly increases the accuracy of deformation measurement and makes it possible to correctly measure the stress-deformation relation of adhesives in tensile and shear directions under high-rate loading.

3.7 Summary of the chapter

The mechanical behaviour of the adhesive Betamate™ 1480 V203 with a bondline thickness of $0.3mm$ was characterised in this chapter at various deformation rates. Butt joint and DCB tests were performed to characterise the quasi-static normal mode behaviour. Lap shear and ENF tests were performed to characterise the quasi-static shear mode behaviour. Additionally, a scarf joint was tested to investigate the quasi-static behaviour of the bondline under a combined normal and shear loading. Intermediate-rate tests were performed with butt joint specimen and high-rate tests were performed with butt joint and lap shear specimen to investigate the bondline behaviour at elevated loading rates.

It was found that the quasi-static butt joint and DCB tests generally correlated well in the strength, energy absorbed and maximum J-integral value, respectively. The stiffness of the DCB specimen was slightly higher than the stiffness measured in the butt joint tests. A reason for this increase could be the different stress state of the bondline in both tests. Additionally, due to the data reduction of the DCB tests oscillations occurred in the measured DCB signals.

The correlation between lap shear and ENF tests was found not as good as between the normal mode tests. The ENF test results showed a significantly stiffer bondline behaviour and the strength was higher than in the lap shear tests. The maximum J-integral value of the ENF tests was lower than the energy absorbed by the bondline in the lap shear experiments. The reason for the difference could be that the stress state in the lap shear tests can be affected by normal stresses at the overlap edge. In the ENF tests, it turned out critical, that a large fracture process zone developed and it could not be excluded that it grew under the loading point of the specimen. This would give an explanation for a conservative measurement of the maximum J-integral. Additionally, the exact determination of the crack front and the crack tip opening displacement could bear errors.

Through a comparison of the strength test with fracture mechanics tests, the reliability of the measured quantities could be estimated. The results were used to estimate the high-rate behaviour of the bondline, which was only tested by the butt joint and lap shear tests (see chapter 5).

An analysis of the combined loading tests by DIC resulted in a loading state comparable to a 15° inclination of a lap shear test, i.e. a large shear deformation and a small normal deformation of the bondline. The stiffness and strength of the joint was therefore similar to the lap shear test. The energy absorbed of the bondline correlated well with a linear variation of corresponding pure mode values.

For the intermediate-rate and high-rate tests a positive rate effect on the stiffness, the maximum stress and the energy absorbed per bonding area could be measured. A study comparing the deformation measurement by DIC and SHBA was done for the experiments on a tensile SHB system. It was found, that the deformation measurement by DIC had a significant influence on the results namely the stiffness of the adhesive and the energy absorbed per bonding area. The results of this chapter will be used to calibrate the rate-dependent bondline behaviour in the simulations in chapter 5.

4 Characterisation of the adherends

In this chapter, the FRP and the aluminium material is characterised for the simulation of bonded joints in chapter 5. The FRP used is the prepreg system Hexply® IM7-8552. Experiments for the determination of quasi-static and high-rate mechanical data have been published by other authors. The mechanical properties are, therefore, taken from literature and outlined in section 4.1. A 6000 series aluminium material is used later in this thesis. To get the mechanical properties, quasi-static and high-rate experiments are described in section 4.2.

4.1 Characterisation of the FRP adherend

It has been outlined in section 2.1.1 that the out-of-plane failure is an important failure mode for a correct representation of bonded joints with FRP adherends. The mechanical properties responsible for out-of-plane failure are the transverse intralaminar failure and the interlaminar failure, which is called delamination failure. Table 4-1 lists the quasi-static mechanical intralaminar properties of the CFRP Hexply® IM7-8552. Assuming a transverse isotropy of the material, the transverse tensile and shear stiffness can be taken for the out-of-plane tensile and shear stiffness. The transverse tensile strength and in-plane shear strength can be used for the out-of-plane tensile strength and out-of-plane shear strength.

Table 4-1 Quasi-static mechanical properties of the CRFP prepreg IM7-8552 [65].

Density [kg/m^3]	1420
Modulus in fibre direction [MPa]	162953
Modulus in transverse direction [MPa]	9003
In-plane shear modulus [MPa]	5179
In-plane Poisson ratio [$-$]	0.32
Tensile strength in fibre direction [MPa]	2326
Compressive strength in fibre direction [MPa]	1017
Tensile strength in transverse direction [MPa]	62
Compressive strength in transverse direction [MPa]	255
In-plane shear strength [MPa]	100

The interlaminar properties can be different from the out-of-plane intralaminar properties. Special testing methods for their determination are standardised and currently discussed. The test methods can be separated in a mode I characterisation, i.e. the ILTS, and a mode II characterisation, i.e. the ILSS. A standard for the quantitative ILTS measurement is the curved beam test according to ASTM D 6415 and the tensile test according to ASTM D 7291. It has been found out, that the ILTS for a UD-layup of IM7-8552 is $76.12MPa$ with a standard deviation of $7.92MPa$ with the curved beam test [101]. Other authors found an ILTS of $77.2MPa$ with a standard deviation of $16.52MPa$ [102]. However, the authors stated in the later study, that the measured values suffered significantly under porosities. Therefore, a three point bending of flat specimens according to ASTM D 2344 was proposed to measure the ILTS property. Using this method which was named “short beam method”, the ILTS property of IM7-8552 has been determined to $116.5MPa$ with a standard deviation of $3.49MPa$.

Test methods for ILSS measurement are standardised according to ASTM D 2344 and EN 2563. The tests described in these standards are the “short curved beam” or the “short flat beam” specimen under three point bending. According to the manufacturer’s data sheet of IM7-8552, the ILSS according to the short beam shear test is $137MPa$ [92]. Makeev [103] and Makeev [104] did these tests too and found a mean ILSS value of $113MPa$ and $97.6MPa$, respectively.

The delamination fracture toughness of composite materials can be found in mode I by DCB specimen according to ASTM D 5528. In the mode II direction, the ENF or four point ENF specimen are widely used. The CFRP system IM7-8552 was tested according to DCB and ENF tests and a mode I fracture toughness value $J_{Ic,del}$ of $0.277J/m^2$ and a mode II fracture toughness value $J_{IIc,del}$ of $0.788J/m^2$ was found [105]. The quasi-static delamination properties used for simulation are shown in table 4-2.

Table 4-2 Quasi-static out-of plane mechanical properties of the CRFP prepreg IM7-8552.

$ILTS\ [MPa]$	116.5	$J_{Ic,del}\ [J/m^2]$	0.277
$ILSS\ [MPa]$	137.0	$J_{IIc,del}\ [J/m^2]$	0.788

The out-of-plane failure of CFRP laminates is dominated by the mechanical behaviour of the matrix system. It can therefore show a rate-dependency. Koerber [87] summarised the rate effect on different CFRP properties. An increase in the stiffness and strength at strain rates starting at $100s^{-1}$ in tensile direction and at $1000s^{-1}$ in the shear direction has been observed by different researchers. Several publications on the rate-dependence of the fracture toughness have been reviewed by Jacob et al. [88]. It was found that positive as well as invariant effects on the delamination fracture toughness have been measured.

For a conservative prediction of the delamination failure, the quasi-static properties are used for simulation since the mechanical properties are assumed to either increase or be approximately constant with increasing strain rate.

4.2 Characterisation of the aluminium adherend

In chapter 5 bonded joints consisting of CFRP-CFRP and CFRP-aluminium adherends are simulated for quasi-static as well as high-rate loading conditions. The aluminium material was, therefore, characterised to gain adequate mechanical properties. The material was a 6000 series sheet aluminium of $2.0mm$ thickness.

4.2.1 Quasi-static testing of the aluminium

The specimen geometry for the characterisation of the aluminium material is shown in Fig. 4-1 (left). Five specimen were milled for quasi-static testing. A black-on-white speckle pattern was sprayed on the specimen for a subsequent DIC evaluation of the specimen strains. Additionally, markers were attached to the specimen for the calibration of the pixel-to-distance ratio. A representative specimen is shown in Fig. 4-1 (right).

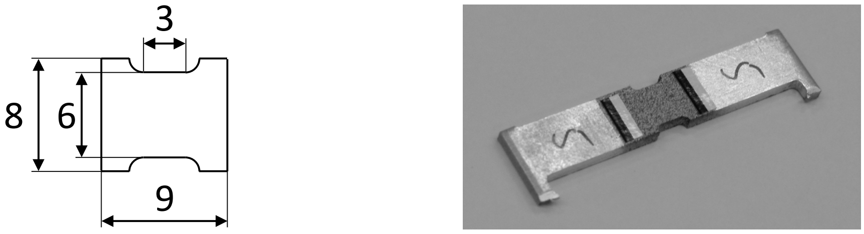

Figure 4-1 Geometry of the aluminium specimen (left) and a representative specimen (right).

Tests were performed on the electromechanical testing machine. The traverse speed was set to $1.0mm/min$. The DIC data record rate was 2 fps at an approximate resolution of 850 x 350 pixels. The nominal strain distribution in x-direction of a representative specimen is shown in Fig. 4-2. The mean nominal strain ϵ_{nom} of the red marked area in the centre of Fig. 4-2 was taken for subsequent evaluation. The true strain was calculated by

$$\epsilon_{true} = ln(1 + \epsilon_{nom}). \tag{4-1}$$

The true stress was determined from the nominal stress σ_{nom} assuming an incompressible deformation of the specimen.

$$\sigma_{true} = \sigma_{nom}(1 + \epsilon_{nom}). \tag{4-2}$$

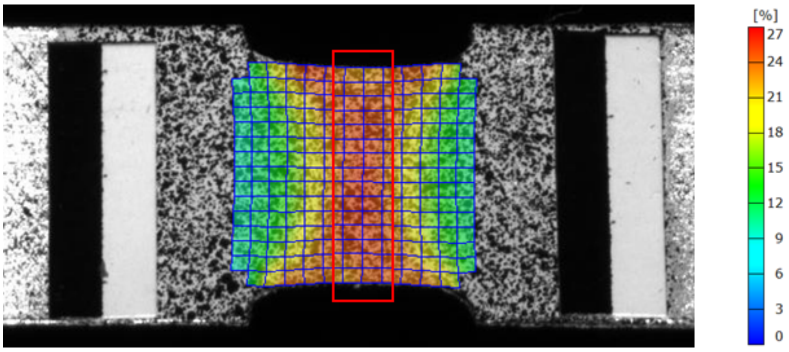

Figure 4-2 Nominal strain in x-direction of a representative aluminium specimen.

The true stress-strain curves of the five quasi-static aluminium specimen are shown in Fig. 4-3. The strain rate based on the DIC measurement was approximately $0.001s^{-1}$. The mean ultimate strength was $371MPa$ with a standard deviation of $8.1MPa$. The Young's modulus has been measured as a tangent modulus between $30MPa$ and $80MPa$ of each test. The mean Young's modulus was $43.3GPa$ with a standard deviation of $3.19GPa$. The yield stress was approximately at $165MPa$. The strain to failure can be visually approximated at 42%.

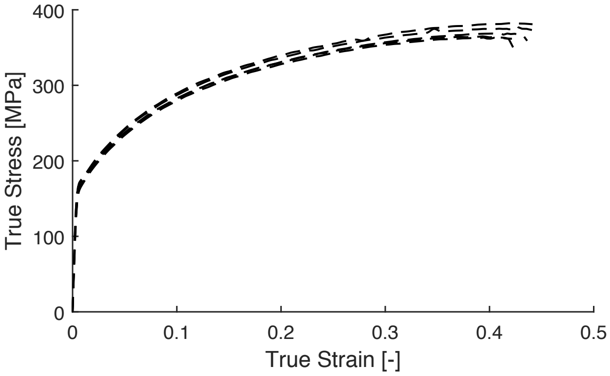

Figure 4-3 True stress-strain curves of the aluminium sheet at a strain rate of $0.001s^{-1}$.

The value of the Young's modulus measured was below the value of $69800MPa$ that can be found in the literature [106]. Due to the short free length of the specimen of $3.0mm$ the strain distribution as shown in Fig. 4-2 indicated that an uniaxial straining was not present during the tests. This can be a source of error in the tests. The Young's modulus is therefore taken from literature, while the plastic hardening curve is taken from the test.

4.2.2 High-rate testing of the aluminium

Five specimen of the same geometry were manufactured for high-rate testing. The specimen were bonded into adapters that allow a fixation in the tensile SHB as described in section 3.6. The striker bar velocity in the high-rate tests was approximately $7.0m/s$. Fig. 4-4 (left) shows the filtered and shifted strain signals according to eqs. (2-36) to (2-38). Filtering was performed with a second order Butterworth filter to reduce the digitalisation noise. The forces measured at the incident bar F_{inc} and at the transmission bar F_{tra} are shown in Fig. 4-4 (right). A dynamic force equilibrium cannot be stated. This is due to an interference of the incident and reflected strain signal on the incident bar strain gauge. The evaluation of the DIC strain distribution, however, showed a uniform strain distribution which is directly related to a dynamic equilibrium during the test. The transmission bar force signal F_{tra} is used for further evaluation.

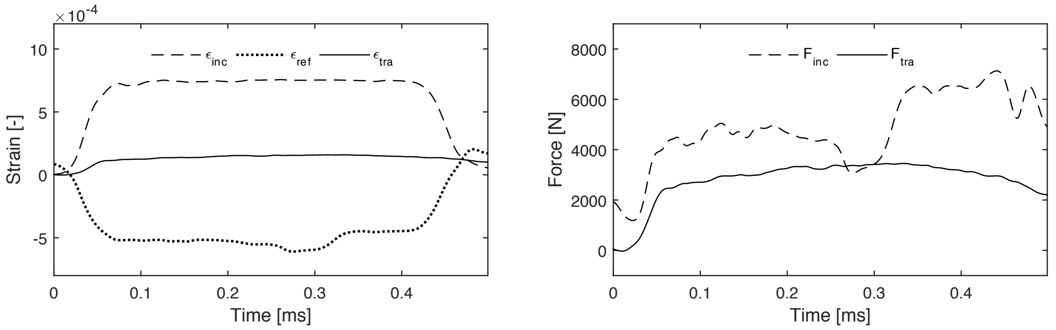

Figure 4-4 Filtered and shifted strain signals (left) and force signals (right).

The stress-strain curve for the representative specimen is shown in Fig. 4-5 (left). The stresses were determined dividing the force signal F_{tra} through the width and thickness of the specimen. The strain rates according to the two-wave evaluation of SHBA according to eq. (2-50) and DIC are shown in Fig. 4-5 (right) for a representative specimen.

The true strains and stresses were subsequently calculated using eqs. (4-1) and (4-2). The true stress-strain curves of all five high-rate aluminium specimen are shown in Fig. 4-6. The strain rate was approximately $800s^{-1}$. The mean ultimate strength in the high-rate tests was $366MPa$ with a standard deviation of $29.7MPa$. The stiffness evaluation of the tests did not lead to proper results due to ringing up effects in the test set-up [87]. The yield stress was visually approximated at $220MPa$. The strain to failure was approximated at 25%.

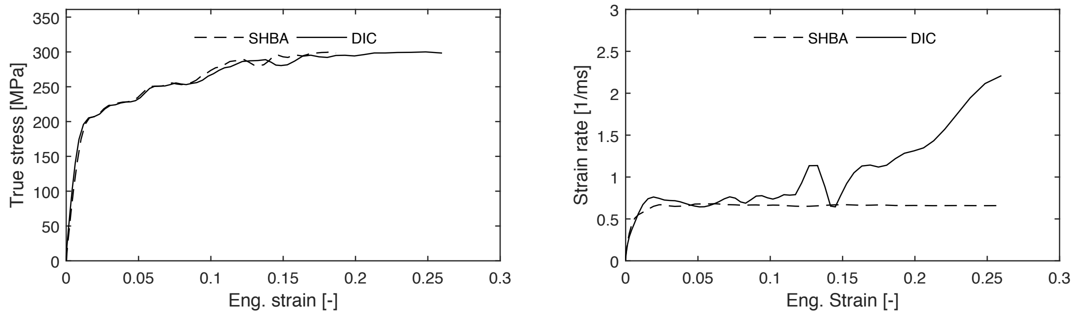

Figure 4-5 Stress-strain curve of a representative aluminium high-rate test (left) and strain rate signals based on SHBA and DIC (right).

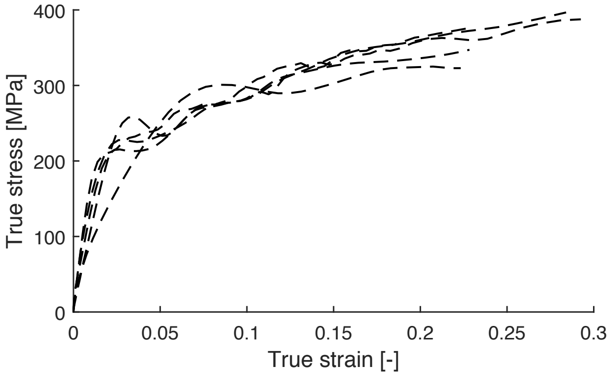

Figure 4-6 Stress-strain curves the aluminium high-rate tests at a strain rate of $800s^{-1}$.

Comparing the static and dynamic tests of the aluminium material, it was found that the yield stress increased from approximately $165MPa$ to $220MPa$. The ultimate stress did not change significantly. The strain to failure was reduced from approximately 42% in the static tests to 25% in the high-rate tests. Although restrictions from the short free length of the specimens are known, the results are taken for subsequent simulation. The influence of the strain rate could be approximated.

4.3 Summary of the chapter

In this chapter, the adherend properties were found for the CFRP material Hexply® IM7-8552 from the literature. Out-of-plane intralaminar properties were defined assuming a transverse isotropy. The interlaminar strength and fracture toughness could be found in recent publications. A positive rate effect can be assumed for the stiffness and strength properties of the CFRP. A rate effect on the fracture toughness could not be clearly identified. The aluminium properties could be characterised by quasi-static and high-rate tests. From the curves found in this section, the appropriate hardening for the aluminium material can be derived. This will be outlined in section 5.2.2.

5 Simulation of cohesive failure in bonded joints

For the simulation of bonded joints with FRP adherends, it is essential to capture the cohesive failure of the adhesive adequately. The results of chapter 3 are used in this chapter, firstly, to model the mechanical behaviour of the adhesive's cohesive behaviour including the cohesive failure for crash applications. A mixed-mode rate-dependent cohesive law is, therefore, presented and calibrated in section 5.1. Secondly, the results of chapter 4 are used to simulate a SLJ in quasi-static and high-rate loading conditions. This is done in section 5.2 and serves as a validation in a 2D simulation. Subsequently, the cohesive law is validated by a T-joint geometry in section 5.3 which served as the validation in the three-dimensional (3D) case. The results of this chapter are summarised in section 5.4.

5.1 Modelling of the adhesive

Different types of cohesive laws have been outlined in section 2.2.2. In this section a rate-dependent mixed-mode implementation is presented. The experimental findings of section 3 are used then to calibrate the cohesive law for the simulation of CFRP-CFRP and CFRP-aluminium SLJs in quasi-static and high-rate loading conditions.

5.1.1 Mixed-mode rate-dependent cohesive law

The following formulation of the cohesive law is based on the static mixed-mode trapezoidal cohesive law published by deMoura et al. [61]. It is defined in terms of a traction-separation relation and qualitatively shown in Fig. 5-1. The separation

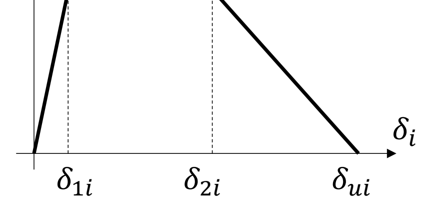

Figure 5-1 Trapezoidal cohesive law.

is generally defined in the three crack opening modes of fracture mechanics δ_I, δ_{II} and δ_{III}. The separation in normal direction is defined by

$$\delta_N = 0.5(\delta_I + |\delta_I|) \tag{5-1}$$

and in shear direction by

$$\delta_S = \sqrt{\delta_{II}^2 + \delta_{III}^2}. \tag{5-2}$$

The stiffness of the cohesive law in each mode can be calculated by

$$S_N = \frac{E_a}{T_{coh}} \qquad S_S = \frac{G}{T_{coh}} \tag{5-3}$$

where E_a and G denote the apparent Young's modulus and shear modulus of the adhesive bondline, respectively, and T_{coh} the thickness of the bondline. At the separation δ_{1i}, which can be calculated by

$$\delta_{1i} = \frac{\tau_{ui}}{S_i} \qquad (no\ sum\ in\ i) \tag{5-4}$$

the degradation of the cohesive stiffness begins. For eq. (5-4) as well as for subsequent equations no summation over equal indices is done. The degradation in the plateau level up to the separation δ_{2i} can be calculated by

$$d = 1 - \frac{\delta_{1i}}{\delta_i} \qquad for \qquad \delta_{1i} \leq \delta_i < \delta_{2i} \tag{5-5}$$

After the plateau, the softening of the cohesive law starts up to the ultimate separation δ_{ui} which is defined by the zero-crossing of the tractions. The area under the traction-separation curve corresponds to the fracture energy of the cohesive law J_{ci}, which corresponds to the maximum J-integral. J_{ci} in each mode $i = N{,}S$ can be calculated by [61]

$$J_{ci} = \frac{\tau_{ui}}{2}(\delta_{2i} - \delta_{1i} + \delta_{ui}) \tag{5-6}$$

The ultimate separation δ_{ui} can be calculated by rearranging eq. (5-6).

$$\delta_{ui} = \frac{2J_{ci}}{\tau_{ui}} + \delta_{1i} - \delta_{2i} \tag{5-7}$$

The degradation in the softening region is defined by

$$d = 1 - \frac{\delta_{1i}(\delta_{ui} - \delta_i)}{\delta_i(\delta_{ui} - \delta_{2i})} \qquad for \qquad \delta_{2i} \leq \delta_i < \delta_{ui}. \tag{5-8}$$

For combined loading conditions, the mixed-mode separation is defined by

$$\delta_m = \sqrt{\delta_N^2 + \delta_S^2} \tag{5-9}$$

and a mixed-mode ratio is defined by [36]

$$\beta = \frac{\delta_S}{\delta_N}. \tag{5-10}$$

A general interaction criterion is taken for the mixed-mode degradation initiation according to

$$\left(\frac{\tau_N}{\tau_{uN}}\right)^{\mu} + \left(\frac{\tau_S}{\tau_{uS}}\right)^{\mu} = 1. \tag{5-11}$$

Setting the exponent to $\mu = 2$ gives the well known quadratic interaction criterion [28, 61, 107]. Using eq. (5-11) with $\mu = 2$ together with eqs. (5-4), (5-9) and (5-10) yields

$$\delta_{1m} = \delta_{1N}\delta_{1S}\sqrt{\frac{1+\beta^2}{\delta_{1S}^2 + \beta^2\delta_{1N}}}. \tag{5-12}$$

which defines the mixed-mode initiation of the degradation. The mixed-mode separation for the beginning of softening yields

$$\delta_{2m} = \delta_{2N}\delta_{2S}\sqrt{\frac{1+\beta^2}{\delta_{2S}^2 + \beta^2\delta_{2N}}}. \tag{5-13}$$

For the mixed-mode fracture, a linear variation of the maximum J-integral in the single modes has been proposed for many adhesives [40, 60, 93].

$$\frac{J_N}{J_{cN}} + \frac{J_S}{J_{cS}} = 1 \tag{5-14}$$

The ultimate mixed-mode separation δ_{um} can be defined using the mixed-mode fracture energy.

$$J_{cm} = \frac{\tau_{um}}{2}(\delta_{2m} - \delta_{1m} + \delta_{um}) \tag{5-15}$$

Using eqs. (5-9) and (5-10) and inserting it together with eqs. (5-12) and (5-13) into eq. (5-15) and subsequently into eq. (5-14) yields

$$\delta_{um} = \frac{2J_{cN}J_{cS}(1+\beta^2)}{\delta_{1m}(S_N J_{cS} + \beta^2 S_S J_{cN})} - \delta_{2m} + \delta_{1m}. \tag{5-16}$$

Eqs. (5-5) and (5-8) can be used accordingly for the calculation of the degradation variable d in mixed-mode.

The cohesive tractions τ_i can be calculated by

$$\tau_i = (1-d)S_i\delta_i \tag{5-17}$$

If the separation becomes negative i.e. the loading in mode N is compressive, the normal traction is determined by

$$\tau_N = S_N\delta_I \qquad for \qquad \delta_I < 0 \tag{5-18}$$

The mixed-mode tractions can be determined by

$$\tau_m = \sqrt{\tau_N^2 + \tau_S^2} \tag{5-19}$$

In order to avoid healing effects the following condition is introduced.

$$d = max_{t' \le t}\left(d(t')\right). \tag{5-20}$$

For higher separations than the ultimate separation $\delta_{um} < \delta_i$, the degradation variable is set equal to $d = 1$.

The rate-dependency of the cohesive law is realised with a logarithmic interpolation of the cohesive tractions with the rate of mixed-mode separation $\dot{\delta}_m$.

$$\tau_i(\dot{\delta}_i) = \tau_i^k + \left(\frac{lg(\dot{\delta}_i) - lg(\dot{\delta}_i^k)}{lg(\dot{\delta}_i^{k+1}) - lg(\dot{\delta}_i^k)}\right)^{\alpha} (\tau_i^{k+1} - \tau_i^k) \tag{5-21}$$

In eq. (5-21), τ_i^k denotes the traction at the lower rate of separation k, τ_i^{k+1} denotes the traction at the higher rate of separation $k+1$, $\dot{\delta}_i^k$ denotes the kth rate of separation and $\dot{\delta}_i^{k+1}$ denotes the $(k+1)$th rate of separation, respectively. α is an exponent with $\alpha = 1$ for linear and $\alpha = 2$ for quadratic logarithmic interpolation. The degradation variable for rate-dependent loading d^k is defined for each given rate of separation k independently. Moreover, eq. (5-20) holds for each given rate of separation to avoid healing effects.

$$d^k = max_{t' \le t}\left(d^k(t')\right). \tag{5-22}$$

Additionally, the current rate of separation $\dot{\delta}_m$ is kept constant after initiation of the degradation.

5.1.2 Calibration of the cohesive law

The formulation of section 5.1.1 is implemented as explicit user material (VUMAT) in Abaqus/Explicit [25]. The cohesive behaviour of the adhesive Betamate™ 1480 V203 is calibrated in this section. Therefore, the cohesive law properties are firstly defined to fit the pure mode experiments quasi-statically and at high-rate loading of chapter 3. Then, the mixed-mode behaviour of the cohesive law is evaluated for the quasi-static loading by the experimental results of the scarf joint. Subsequently, the results of the intermediate-rate experiments are used for the calibration of rate-dependent interpolation.

In normal mode direction, butt joint and DCB specimen were performed in sections 3.1 and 3.2. The property determination technique [7] is used to calibrate the trapezoidal cohesive law. The stiffness S_N and ultimate strength τ_{uN} are defined according to the results of the butt joint tests. The ultimate strength τ_{uN} was set between the yielding and the mean maximum strength of the tests. The mean fracture energy is taken from the fracture mechanics tests i.e. the maximum J-integral of the DCB test results. In the normal direction, the difference between the energy absorbed in the butt joint tests and the fracture energy of the DCB tests was negligibly small. The DCB test showed however less scatter than the butt joint test. The separation where softening starts δ_{2i} is defined in a way, that the inclination of the softening part of the cohesive law corresponds to the inclination of softening in the fracture mechanics tests. In shear direction, the stiffness S_S and ultimate strength τ_{uS} are defined correspondingly to the lap shear test of section 3.1. The energy absorbed measured by the lap shear tests differed from the fracture energy measured by the ENF test. Both experiments had shortcomings. The mean maximum J-integral value from the ENF test results according to section 3.3 is however taken for the calibration of the cohesive law because it is the more conservative value and it fullfils well the linear variation of the fracture energy over the mixed-mode ratio. Table 5-1 lists the properties of the trapezoidal cohesive law. Fig. 5-2 shows the trapezoidal cohesive law together with the experimental results of the butt joint and the lap shear tests for a deformation rate $\dot{\delta} = 3\mu m/s$.

Table 5-1 Properties of the trapezoidal cohesive law of the adhesive for a deformation rate of $\dot{\delta} = 3\mu m/s$.

$S_N[N/mm^3]$	6156	$S_S[N/mm^3]$	801
$\tau_{uN}[MPa]$	38.0	$\tau_{uS}[MPa]$	31.0
$\delta_{2N}[mm]$	0.063	$\delta_{2S}[mm]$	0.233
$J_{cN}[mJ/mm^2]$	3.21	$J_{cS}[mJ/mm^2]$	9.45

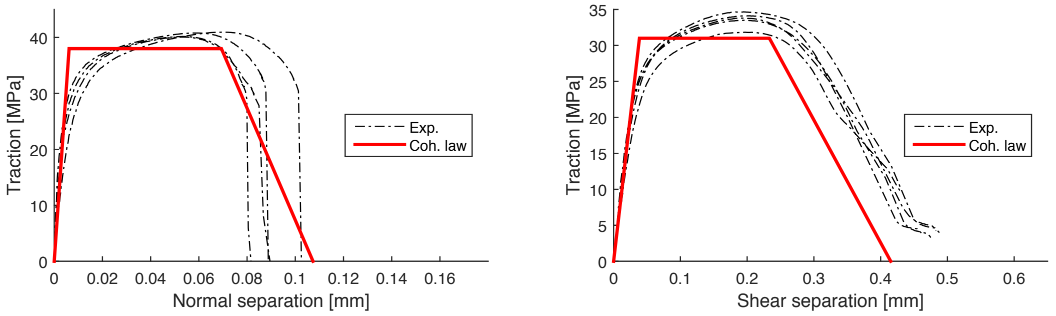

Figure 5-2 Trapezoidal cohesive law in normal direction (left) and in shear direction (right) for a deformation rate of $\dot{\delta} = 3\mu m/s$.

From the high-rate experiments, the stiffness S_N, S_S and the ultimate traction τ_{uN} and τ_{uS} are defined based on the butt joint test and lap shear test. The maximum J-integral could not be measured directly by high-rate experiments, since DCB and ENF tests were not performed. The fracture energy is, therefore, estimated using the ratio of the maximum J-integral to the energy absorbed per bonding area from the quasi-static tests. In normal direction, the ratio was 1.009 and in shear direction the ratio was 0.826. Table 5-2 lists the properties of the trapezoidal cohesive law at high-rate loading. Fig. 5-3 shows the trapezoidal cohesive law and the experimental results of the butt joint and the lap shear tests for a deformation rate of $\dot{\delta} = 3m/s$.

Table 5-2 Mechanical properties for the trapezoidal cohesive law of the adhesive for a deformation rate of $\dot{\delta} = 3m/s$. (*) indicates estimated values.

$S_N[N/mm^3]$	25044	$S_S[N/mm^3]$	2925
$\tau_{uN}[MPa]$	82.0	$\tau_{uS}[MPa]$	56.0
$\delta_{2N}[mm]$	0.027	$\delta_{2S}[mm]$	0.149
$J^*_{cN}[mJ/mm^2]$	3.75	$J^*_{cS}[mJ/mm^2]$	13.32

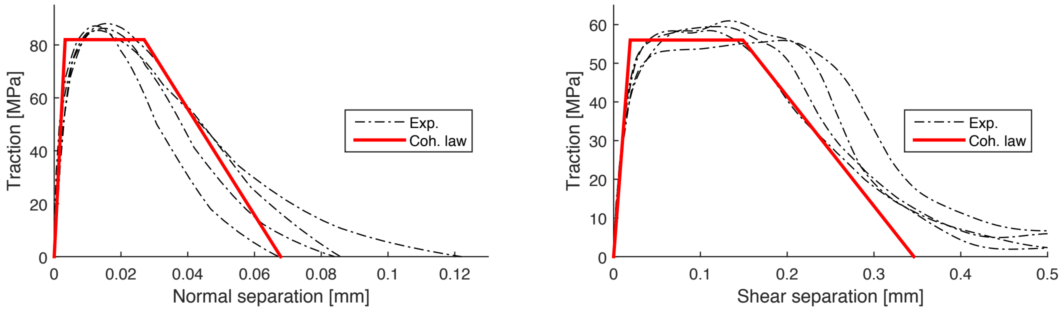

Figure 5-3 Trapezoidal cohesive law in normal direction (left) and in shear direction (right) for a deformation rate of $\dot{\delta} = 3m/s$.

The mixed-mode behaviour of the cohesive law is shown in Fig. 5-4 for the deformation rate $\dot{\delta} = 3.0\mu m/s$ (left) and $\dot{\delta} = 3.0m/s$ (right) for various loading ratios $\phi = \frac{180°}{\pi} arctan(\beta)$. $\phi = 0°$ is equivalent to $\beta = 0$ and corresponds to a pure normal loading. $\phi = 90°$ is equivalent to $\beta = \infty$ and corresponds to a pure shear loading. The mixed-mode tractions have been evaluated based on eq. 5-19 and the mixed-mode separations based on eq. 5-9.

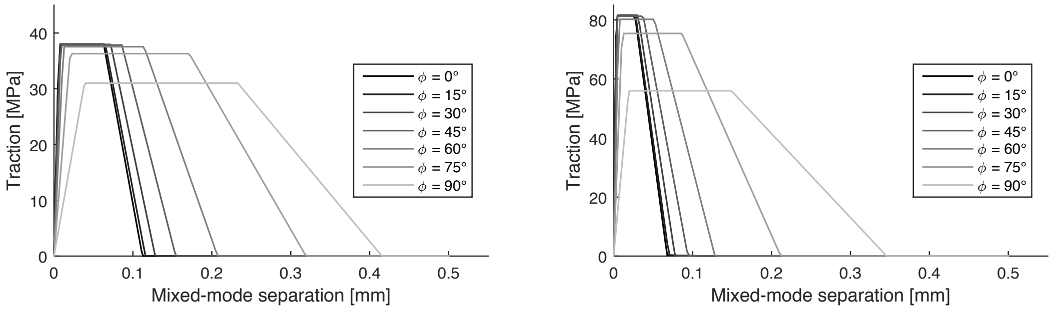

Figure 5-4 Mixed-mode behaviour of the cohesive law for $\dot{\delta} = 3\mu m/s$ (left) and $\dot{\delta} = 3m/s$ (right) for various loading ratios ϕ.

In Fig. 5-5 the results of the scarf joint tests of chapter 3.4 are shown together with the mixed-mode cohesive behaviour at $\phi = 15°$ for a deformation rate of $\dot{\delta} = 3\mu m/s$. It can be seen that the stiffness as well as the ultimate traction is higher than the experimental findings. The mean energy absorbed per bonding area was $8.65mJ/mm^2$. This value correlates well with the fracture energy $8.45mJ/mm^2$ of the cohesive law.

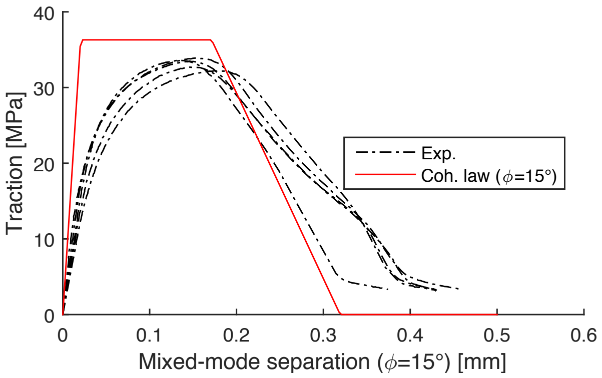

Figure 5-5 Comparison of the cohesive law at $\phi = 15°$ for $\dot{\delta} = 3\mu m/s$ with the experimental results of the scarf joint tests.

The cohesive law in pure mode loading was defined for the deformation rates $\dot{\delta} = 3\mu m/s$ and $\dot{\delta} = 3m/s$. The exponent α for the interpolation of the deformation rates is defined in the following. The experimental results of the butt joint tests are shown in Fig. 5-6. Additionally, the interpolated cohesive law for $\alpha = 1$ and

$\alpha = 2$ at a deformation rate of $\dot{\delta} = 0.2mm/s$ is shown. It can be seen that a better approximation of the stiffness S_N as well as the ultimate traction τ_{uN} is found for $\alpha = 2$. For subsequent simulations $\alpha = 2$ is used. Fig. 5-7 shows the cohesive law in normal direction and shear direction for quadratic interpolation $\alpha = 2$ for various rates of separation.

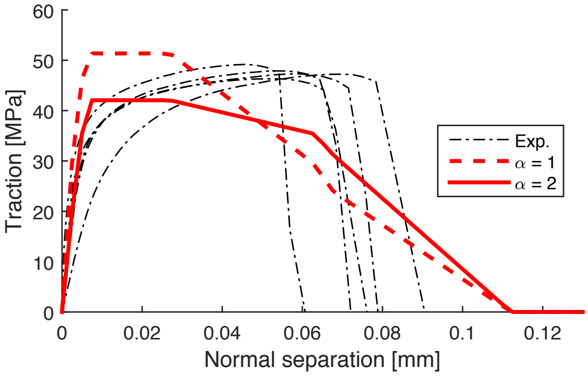

Figure 5-6 Cohesive laws in mode N for linear ($\alpha = 1$) and quadratic ($\alpha = 2$) logarithmic interpolation of the tractions compared to the butt joint experiments at the deformation rate $\dot{\delta} = 0.2mm/s$.

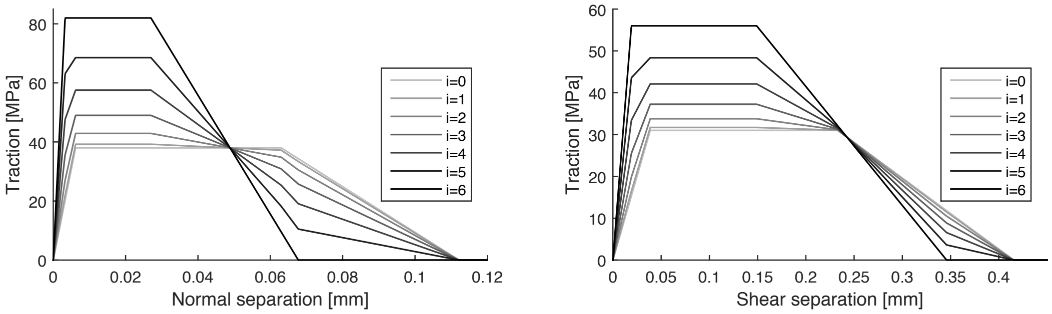

Figure 5-7 Cohesive laws for quadratic interpolation ($\alpha = 2$) in normal direction (left) and shear direction (right) for various deformation rates $\dot{\delta} = 3.0 \cdot 10^i \mu m/s$.

5.2 Testing and simulation of a single lap joint (SLJ)

The cohesive law is validated in this section by comparison of simulation and experiments of a SLJ geometry which is a validation in 2D on the coupon level. The adherend's material combinations for the SLJ are CFRP-CFRP and CFRP-aluminium. The different type of adherends make it possible to identify the influence of different surfaces and plastic deformation on the force-displacement curves as well as the influence of different thermal expansions in the adherends. All tests will be done at quasi-static and at high-rate loading conditions and are compared to simulations using the cohesive law presented and calibrated in section 5.1.

5.2.1 Specimen manufacturing and testing

The specimen geometries of the CFRP-CFRP and CFRP-aluminium SLJ are shown in Fig. 5-8 (left) and (right), respectively. The geometry differs from the standard geometry of a SLJ according to ASTM D1002 to reduce the displacement to failure because in the SHB set-up large displacements are difficult to achieve. Additionally, the dynamic force equilibrium is improved for short specimen. The CFRP adherends had a thickness of $1.0mm$ and were made of the UD-prepreg material IM7-8552. The layup was $[0]_8$ with the 0°-fibres running in loading direction. For the CFRP-aluminium SLJ, the metal adherend is an aluminium sheet of $2mm$ thickness. The adherends were bonded over an overlap length of $10mm$ with a bondline thickness of $0.3mm$. The width of the all SLJs was $8mm$. The specimen free length was $50mm$. The specimen were produced with a $20mm$ oversize at each end to enable a fixation of the adherends either in the electromechanical test frame for quasi-static testing or the SHB set-up for high-rate testing. Five specimen were tested in each case.

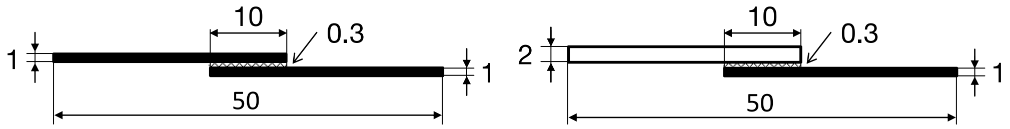

Figure 5-8 Specimen geometry of the CFRP-CFRP SLJ (left) and the CFRP-aluminium SLJ (right).

The plate for the CFRP adherends was manufactured in an autoclave according to the manufacturer's guideline [92]. The CFRP adherends for the SLJ were cut in a water cooled diamond saw. The aluminium adherends were cut from the aluminium sheet by water-jet cutting insuring sharp edges and no warping of the aluminium adherends. Before bonding, the adherends were cleaned with isopropanol. A custom made fixture was used to guarantee a bondline thickness of $0.3mm \pm 0.05mm$

during curing. The fixture is sketched and shown in Fig. 5-9. The SLJ specimen were cured for $30min$ at $180°C$ in an oven.

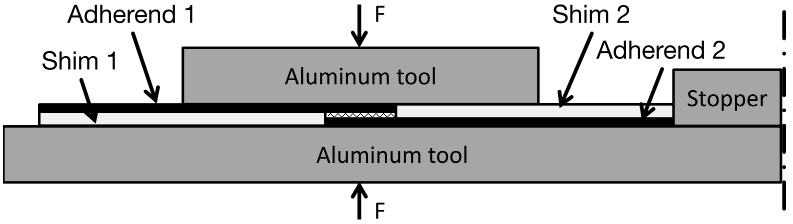

Figure 5-9 Sketch of the custom made fixture for curing the SLJ specimen with a constant bondline thickness.

After curing, shims of $20mm$ length were bonded on the edge of the adherends with the adhesive “UHU Endfest 300” (UHU GmbH, Bühl, Germany) at $70°C$ for $15min$. The shims were used to avoid any residual forces or moments due to the offset of the adherends. Then, the specimen were sanded in width direction on disc-type sander with a grain size of 250 to remove the poured out adhesive and to guaranty a constant specimen width. Afterwards, the spew fillets at the edge of the overlap were manually removed using a sharp knife. Care was taken not to cause damage to the edge of the bondline. A representative specimen of the CFRP-CFRP and CFRP-aluminium SLJ is shown in Fig. 5-10 (top) and (bottom), respectively. For the high-rate tests, the specimen were additionally bonded into an adapter with an outer thread to screw them into the SHB set-up.

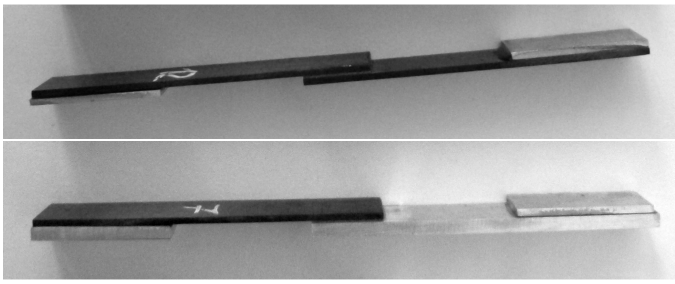

Figure 5-10 Representative CFRP-CFRP (top) and CFRP-aluminium (bottom) SLJ specimen for quasi-static testing.

The SLJ specimen were tested quasi-statically in the electromechanical test frame. The deformation of the specimen was measured visually by the videoextensometer. The markers for the measurement were attached as close as possible to the edge of the free length of the specimen. The specimen were fixed into the test frame by clamping claws. The testing speed was set to $0.2mm/min$. Fig. 5-11 shows pictures from the test set-up. The results from the quasi-static tests are shown in section 5.2.2 together with the results from simulation.

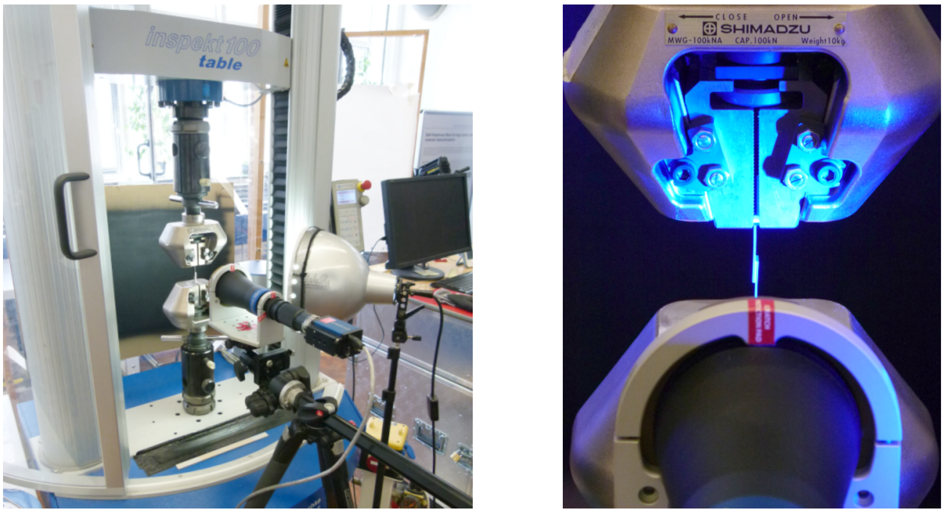

Figure 5-11 Set-up of the quasi-static testing of a SLJ.

The side view of the broken specimen as well as the fracture surface of a representative CFRP-CFRP and CFRP-aluminium specimen are shown in Figs. 5-12 and 5-13, respectively. It can be seen from the side view, that at the edge of the overlap the failure occurred close to the adherends. In the middle of the overlap the adhesive failed by cracks inclined by an angle of approximately 45°.

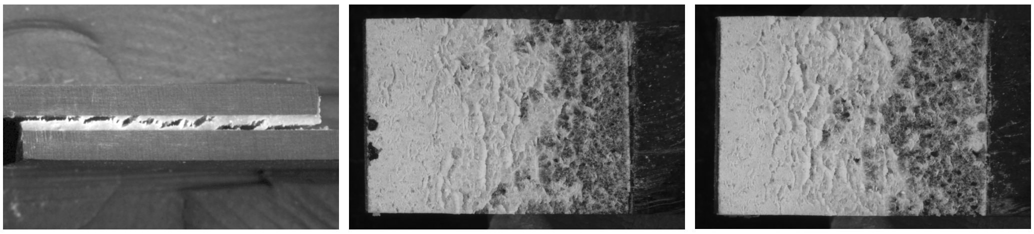

Figure 5-12 Side view of the broken CFRP-CFRP SLJ specimen (left) and fracture surfaces (middle and right).

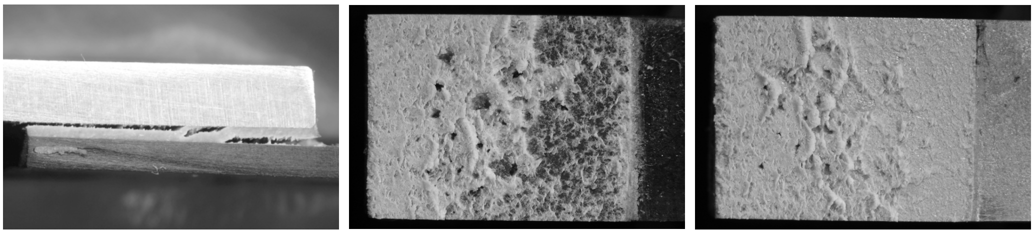

Figure 5-13 Side view of the broken CFRP-aluminium SLJ specimen (left) and fracture surfaces (middle and right).

It can be seen from the fracture surfaces, that the adhesive covers most of the bonding area for these specimens and cohesive failure of the bondline can be assumed. Not bonded spots are present at the edge of the overlap where the CFRP adherend is running out. A reason for these spots could be, that at the front side of the CFRP adherends either the surface roughness or diffusing gases during curing interacted with the adhesive causing voids. This can have an influence on the strength of the bond. In the middle of the bonding area some voids can be observed, too. Since the maximum stresses and the initial failure of the bond occur at the edge of the overlap, the voids in the middle are assumed to have no significant effect on the strength of the joint. A clear cohesive failure of the adhesive occurred in the CFRP-CFRP SLJ. On the aluminium surface, the failure occurred closer to the adherend surface than to the CFRP. Still, adhesive material can be seen on the aluminium. A cohesive failure is, therefore, assumed for the CFRP-aluminium SLJ as well.

The specimens for high-rate testing were glued into adapters with the adhesive “UHU Endfest 300” at $70°C$ for $15min$. In order to gain a dynamic force equilibrium a pulse shaping of the incident wave was applied for the SLJ testing in the tensile SHB set-up. An $0.5mm$ thin ethylene-propylene-diene-monomer (EPDM) rubber was positioned at the surface of the impact flange, which was hit by the $500mm$ U-type striker bar to generate the incident wave. The velocity of the striker was approximately $3.5m/s$. The rate of record of the strain signals was 10^6Hz. The filtered and shifted strain waves are shown in Fig. 5-14 (left), the forces at the incident and transmission bar end are shown in Fig. 5-14 (right). Comparing the forces F_{inc} and F_{tra}, a dynamic force equilibrium can be seen.

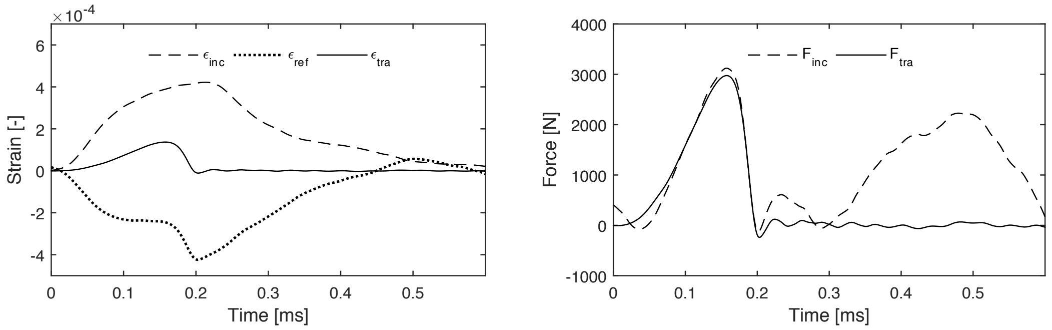

Figure 5-14 Filtered and shifted strain gauge signals (left) and force signals (right) of an high-rate CFRP-CFRP SLJ.

The specimen deformation was measured by the high-speed camera and subsequent DIC evaluation. The frame rate was set to 210000 fps at a resolution of 448 x 64 pixel. Two markers on each side of the specimen were applied. Fig. 5-15 shows the specimen from the high-speed camera initially and at the time of failure.

The force-displacement curve of the specimen is shown in Fig. 5-16 (left) using the outer markers on the specimen. It can be seen that the DIC measurement is in very good correlation with the curve of SHBA. Using the inner markers turned out to reduce the free length of the specimen and bear inaccuracies. Therefore, the SHBA measurement of the displacement was used for the evaluation of the specimen

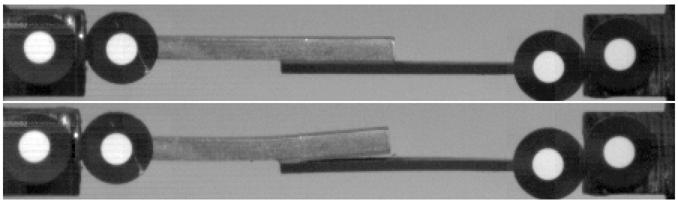

Figure 5-15 Side view of an CFRP-aluminium SLJ initially (top) and at the time of failure (bottom) for a CFRP-aluminium SLJ.

displacements in the high-rate SHB tests in the following. Fig. 5-16 (right) shows the rate of displacement of the specimen, which is approximately $2.0 m/s$. The results of all high-rate tests is shown in section 5.2.2 together with the simulation results.

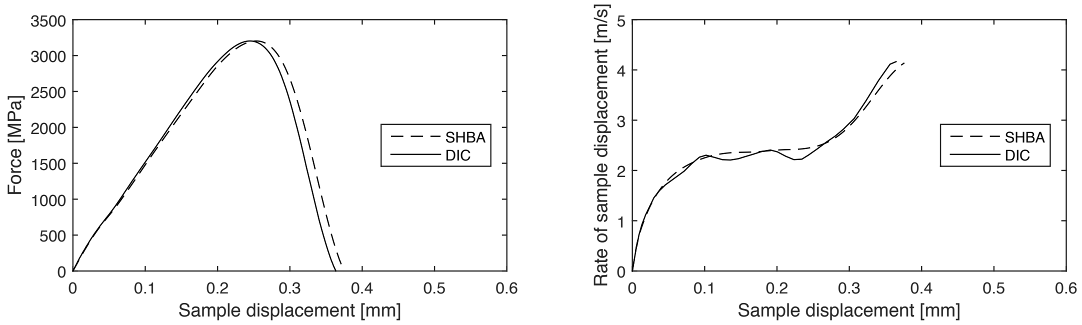

Figure 5-16 Force-displacement curve (left) and displacement rate signals (right) of a representative CFRP-CFRP SLJ comparing SHBA and DIC.

The fracture surface of a CFRP-CFRP SLJ showed a cohesive failure of the adhesive according to Fig. 5-17. Adhesive can be seen in this specimen occupying most parts of the bonding area. Voids at the edge of the overlap could be observed for all specimen similar to the quasi-static test results. These voids are assumed to significantly reduce the strength of the joint. The CFRP-aluminium SLJ showed a cohesive failure as shown in Fig. 5-18. A small amount of voids randomly distributed over the bonding area as well as delaminations in the CFRP were observed again reducing the joint strength.

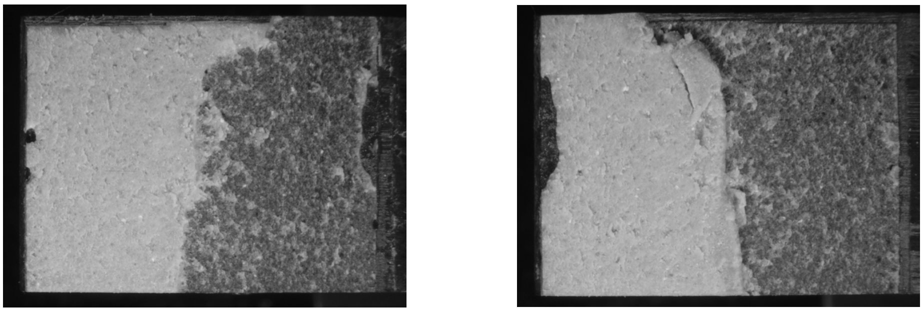

Figure 5-17 Fracture surfaces of a CFRP-CFRP SLJ.

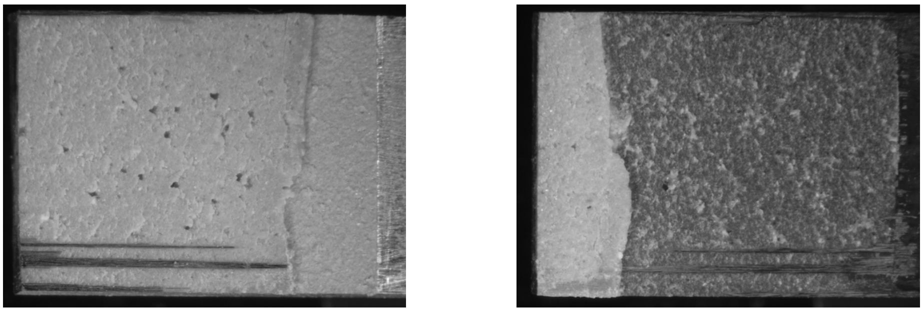

Figure 5-18 Fracture surfaces of a CFRP-aluminium SLJ.

5.2.2 Numerical evaluation

A 2D simulation of the SLJ was performed with the Abaqus/Explicit solver [25]. For the adherends, reduced integration linear plane stress elements with enhanced hourglass control (CPS4R) were used. At the overlap the mesh size was set to $0.1mm$, outside the overlap the mesh size was $0.5mm$. The adhesive was meshed with one element over the complete bondline thickness of $0.3mm$ and a mesh size of $0.1mm$ in the direction of the bondline. For the adhesive, 2D cohesive elements (COH2D4) were used. The boundary conditions were applied on reference points at each end of the models, that were connected via multi-point constraints (MPC) to the left and right edge of the model, respectively. Both ends of the model were simply supported, while a smooth step velocity boundary condition was applied in x-direction of one end. The mesh and boundary conditions for the CFRP-CFRP SLJ and the CFRP-aluminium SLJ are shown in Fig. 5-19.

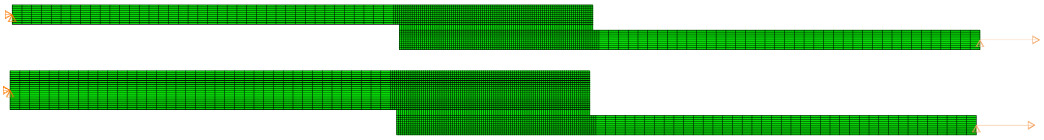

Figure 5-19 Geometry and mesh of the CFRP-CFRP SLJ (top) and the CFRP-aluminium SLJ (bottom).

For the quasi-static tests, the CFRP material was modelled as a linear elastic orthotropic material. The properties were set to the IM7-8552 data of table 4-1. The aluminium was modelled isotropically elastic-plastic. The Young's modulus was set to $68.9GPa$ and the Poisson ratio to 0.33 based on the data sheet of a comparable aluminium material [106]. A plasticity with isotropic hardening was defined as it was commercially available in Abaqus [25]. The plastic curve was given in tabular form as shown together with the experimental findings of section 4.2.1 in Fig. 5-20. The cohesive law of the bondline was implemented as an explicit user material VUMAT in Abaqus/Explicit according to section 5.1.1.

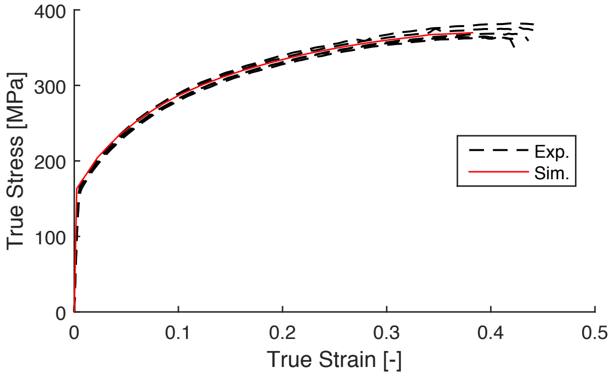

Figure 5-20 Definition of the quasi-static aluminium properties in the simulation compared to the experiments at a strain rate of $0.001 s^{-1}$.

For the simulation of the high-rate experiments, the same geometry, mesh and boundary conditions were used like for the quasi-static experiments. The velocity boundary condition was set to $2.0 m/s$. The CFRP was modelled with the same properties for high-rate loading than for quasi-static loading because the stiffness in fibre direction shows no significant rate-dependency for UD-CFRP materials [87]. For the transverse properties of the CFRP, the influence on the force-displacement curve of the SLJ was assumed negligible. The aluminium material properties were adapted to meet the experimental results of section 4.2.2. An isotropic elastic-plastic material with isotropic hardening is used again. The elastic material properties were set equal to the quasi-static properties with a Young's modulus of $68.9 GPa$ and a Poisson ratio of 0.33. The plasticity definition is tabularly defined and shown in Fig. 5-21. All adherends were modelled rate-independent. For the adhesive, the mixed-mode rate-dependent cohesive law outlined in section 5.1.2 was used.

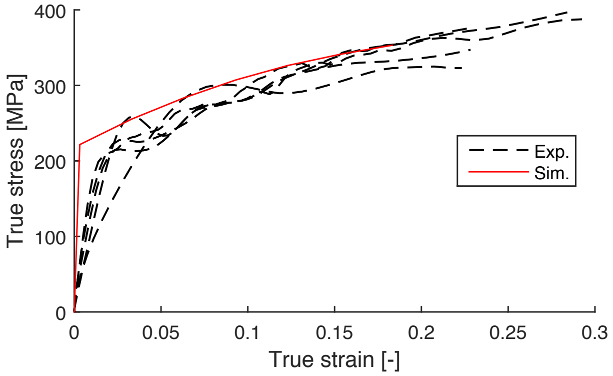

Figure 5-21 Definition of the high-rate aluminium properties in the simulation compared to the experiments at a strain rate of $800 s^{-1}$.

5.2.3 Results

In the experiments, a loading rate of $1.5\mu m/s$ was measured. The results of the simulation compared to the experimental curves of the quasi-static CFRP-CFRP SLJ experiments are shown in Fig. 5-22 (left). It can be seen that the stiffness of the simulation approximates well the stiffness of the experiments. When the adhesive starts to degrade, the force plateau in the simulation begins. The maximum force in the simulation is $2425N$. The mean maximum force in the experiments is $2079N$ with a standard deviation of $230N$. This means that the simulation overestimates the experimental curve by 17%. The CFRP-CFRP SLJ fails due to cohesive failure of the bondline which terminates the force plateau. The maximum displacement is well in the experimental scatter. The energy absorbed in the simulation is $741Nmm$. The experiments showed a mean energy absorbed of $625Nmm$ with a standard deviation of $142Nmm$. This means the simulation is 19% above the experimental results but within the standard deviation.

The simulation of the CFRP-aluminium SLJ compared to the experimental results can be seen in Fig. 5-22 (right). The initial stiffness of the simulation is well in the experimental scatter. At a load level of approximately $1300N$ the aluminium adherend starts to yield and at approximately the same load level the adhesive starts to degrade. The stress plateau in the simulation starts when the plastic deformation of the aluminium adherend is terminated and mainly the adhesive is responsible for the joint compliance. The maximum force in the simulation is $2350N$. In the experiments, a mean maximum force of $2301N$ with a standard deviation of $54N$ is measured. This means the simulation approximated the experimental results well with a 2% higher maximum force. The cohesive failure of the bondline terminates the force plateau. The displacement to failure is higher in the simulation than in the experiments. The energy absorbed in the simulation is $876Nmm$. In the experiments a mean energy absorbed of $646Nmm$ with a standard deviation of $31Nmm$ is measured. This means an error of 36% regarding the energy absorbed.

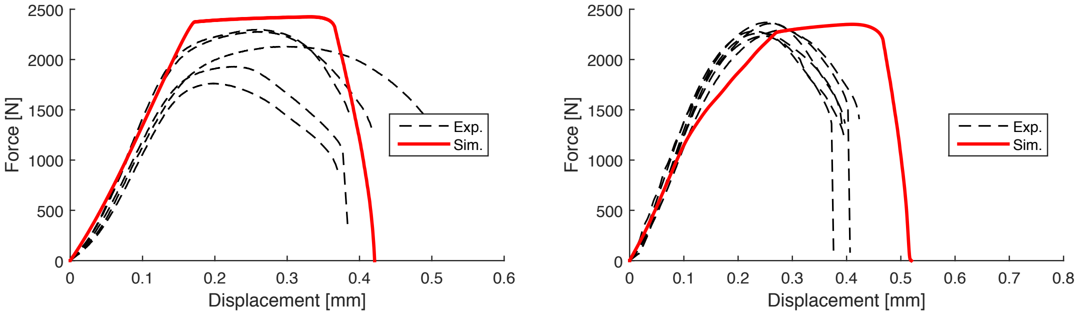

Figure 5-22 Force-displacement curve of the quasi-static experiments of the CFRP-CFRP SLJ (left) and the CFRP-aluminium SLJ (right) at a loading rate of $1.5\mu m/s$.

The results of the simulation with the CFRP-CFRP SLJ high-rate tests compared to the experiments can be seen in Fig. 5-23 (left). The stiffness of the simulation initially approximates the experimental findings. However, the joint stiffness increases during the simulation due to a rotation of the joint while the experiments showed an approximately linear increase of the force signal. With the start of degradation the adhesive layer the force plateau begins. The maximum force in the simulation is $4016N$. In the experiments a mean maximum force of $3427N$ with a standard deviation of $229N$ can be measured. This means the simulation is 17% higher than the experimental results. The displacement to failure of the simulation is well in the experimental scatter. The energy absorbed in the simulation was $1009Nmm$. The experiments resulted in a mean energy absorbed of $775Nmm$ with a standard deviation of $114Nmm$. This means the energy absorbed in the simulation is 30% over the experimental findings.

For the CFRP-aluminium SLJ high-rate tests, the force-displacement curve comparing simulation and experiments can be seen in Fig. 5-23 (right). The stiffness of the simulation is well in the scatter of the experiments. The yielding of the aluminium adherend as well as the start of degradation at the edge of the bondline starts at approximately $1500N$. The maximum force in the simulation is $3475N$ which is not a force plateau in this case. In the experiments a mean maximum force of $2934N$ with a standard deviation of $161N$ is measured. The simulation is 18% over the mean maximum force of the experiments. The displacement to failure is overestimated by the simulation. The energy absorbed in the simulation is $1282Nmm$. The experiments result in a mean energy absorbed of $812Nmm$ with a standard deviation of $146Nmm$. This means the simulation is 58% over the experimental findings.

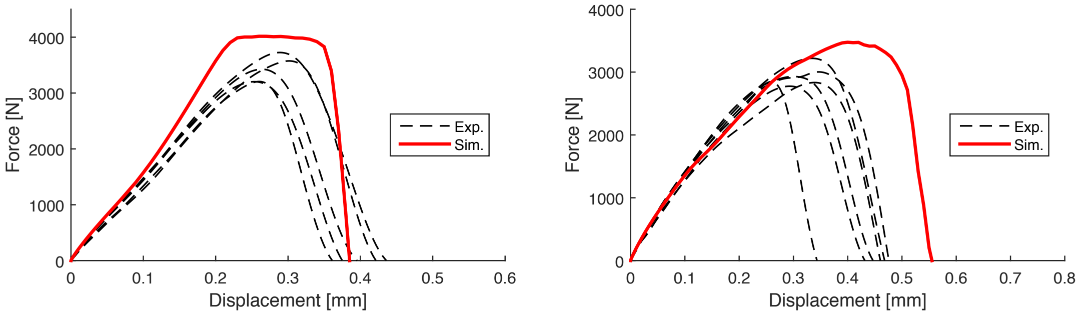

Figure 5-23 Force-displacement curve of the high-rate experiments of the CFRP-CFRP SLJ (left) and the CFRP-aluminium SLJ (right) at a loading rate of $2.0m/s$.

The stress distribution is evaluated for the high-rate tests only, since the maximum load level is significantly higher than in the quasi-static simulations. The stress distribution at the maximum loading of $4016N$ in the high-rate CFRP-CFRP SLJ is shown in Fig. 5-24. Table 5-3 lists the maximum compressive and tensile stresses in the adherends with the corresponding stress exposure. This is defined as the ratio between the current stress value divided by material strength as defined in table 4-1 [108]. It can be seen, that the transverse tensile stress occurring at the overlap edge lead to the highest stress exposure of 0.72. A failure of the adherends is therefore not assumed for the CFRP-CFRP SLJ. The stress distribution at the maximum loading of $3475N$ in the high-rate CFRP-aluminium SLJ is shown in Fig. 5-25. Table 5-4 lists the maximum compressive and tensile stresses in the adherends with the corresponding stress exposure. The transverse tensile stress leads to the highest stress exposure of 0.92 in the CFRP adherend, but still, no failure must be expected in the simulations. The maximum Mises stress in the aluminium adherend is $285.7MPa$ and is uncritical.

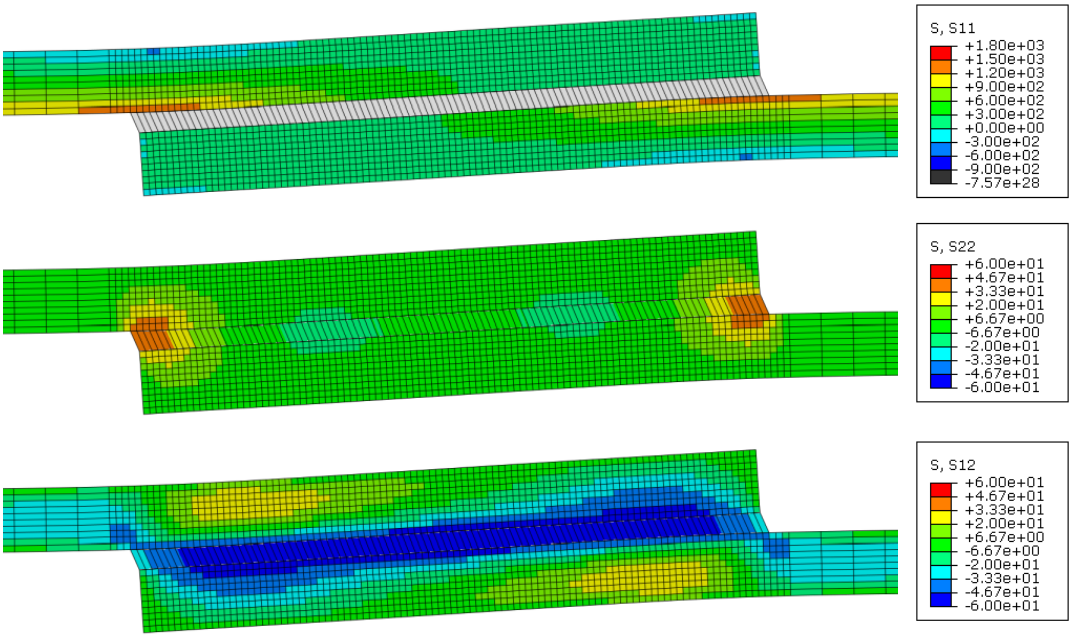

Figure 5-24 Stress distribution in the high-rate CFRP-CFRP SLJ at the maximum loading.

Table 5-3 Maximum stress (stress exposure) in the adherends of the high-rate CFRP-CFRP SLJ at the maximum load.

Direction	Compressive	Tensile
Fibre	-301.3MPa (0.30)	1428.4MPa (0.61)
Transverse	-7.6MPa (0.03)	44.8MPa (0.72)
Shear	-52.0MPa (0.52)	30.1MPa (0.30)

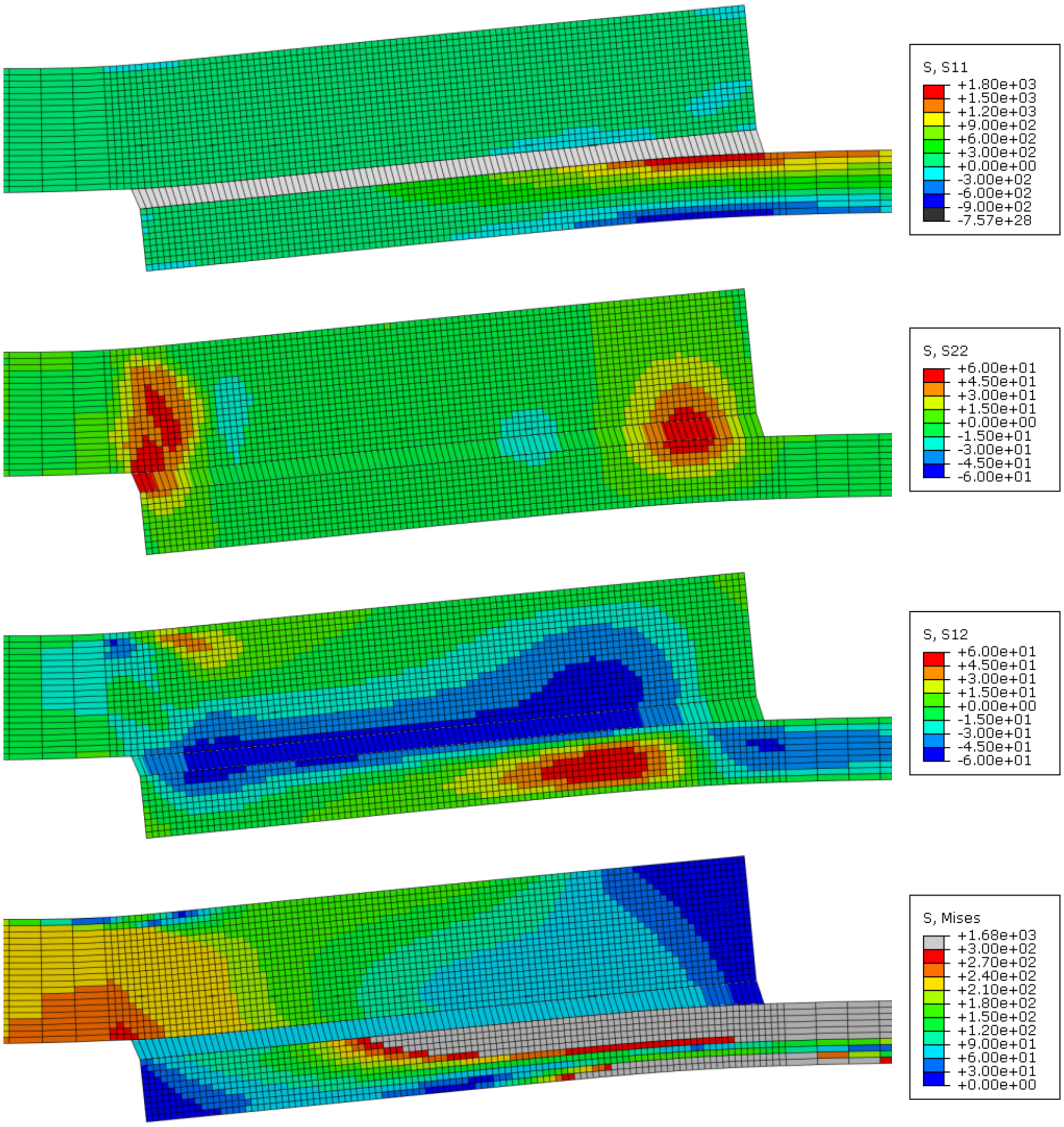

Figure 5-25 Stress distribution in the high-rate CFRP-aluminium SLJ at the maximum loading.

Table 5-4 Maximum stress (stress exposure) in the adherends of the high-rate CFRP-aluminium SLJ at the maximum load; (*) only for CFRP; (**) only for aluminium

Direction	Compressive	Tensile
Fibre*	-759.1MPa (0.75)	1703.0MPa (0.73)
Transverse*	-26.5MPa (0.10)	56.8MPa (0.92)
Shear*	-49.9MPa (0.50)	59.7MPa (0.60)
Mises**	285.7MPa (-)	

5.2.4 Discussion

The initial stiffness of the experiments was well in agreement with the simulation for the CFRP-CFRP SLJ and the CFRP-aluminium SLJ. Since the geometry of the SLJ was scaled down to meet the requirements for high-rate testing on the SHB set-up, the influence of the boundary conditions cannot be neglected. In Fig. 5-26 different sets of boundary conditions are investigated and plotted together with the experimental findings of the quasi-static CFRP-CFRP SLJ. The boundary conditions investigated are explained in the following:

1. Ref.: This is the simple support boundary condition on both sides of the SLJ as described in section section 5.2.2.
2. SF: One end of the SLJ is simply supported. The other end, where the velocity in x-direction is applied is free.
3. CR: One end of the SLJ is clamped. The other end, where the velocity in x-direction is applied is rotationally fixed but free to deform in y-direction.
4. CC: One end of the SLJ is clamped. The other end, where the velocity in x-direction is applied is fixed rotationally and in y-direction.

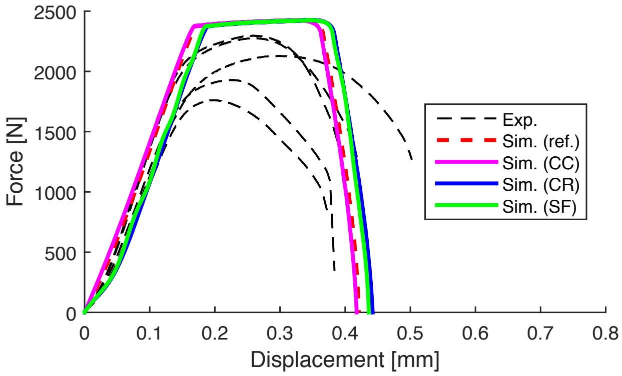

Figure 5-26 Force-displacement curve of the SLJ tests with varying the boundary conditions for the quasi-static CFRP-CFRP SLJ ($1.5\mu m/s$).

An influence of the boundary conditions on the initial stiffness of the simulation can be observed. The vertical fixation of both ends of the SLJ has the main influence since the results of the SF and CR variants and the SS and CC variants are pairwise similar. In the experiments, it could be observed that the adherends moved vertically in y-direction during the quasi-static tests, while in the high-rate experiments barely no vertical displacement in y-direction took place. The reason lies in the stiffness of the test set-up for the quasi-static tests which initially fixes the specimen well but provides a compliance at higher loads in y-direction during the test. In the high-rate test, the inertia of the test set-up inhibits a vertical displacement of the SLJ adherends. Concluding it must be stated that the stiffness of the SLJ experiments was satisfactory approximated by the simulation. An exact evaluation was not possible due to the imprecise initial support situation in the experiments.

In the CFRP-aluminium SLJ simulations according to Fig. 5-22, an influence of the aluminium yielding on the force-displacement curve could be observed. The experimental findings did, however, not show a yielding of the aluminium. It is, therefore, investigated whether the aluminium behaviour was correctly modelled. A purely elastic isotropic modelling of the aluminium material is done with a Young's modulus of $68.9MPa$ and a Poisson ratio of 0.33. Fig. 5-27 shows the force-displacement curve together with the results of section 5.2.2. A significant influence of the aluminium yielding can be seen for both loading rates. A good correlation between the simulation and the experiments is found with the new aluminium properties in the quasi-static case. The maximum force in the simulation is $2400N$ and the energy absorbed is $722Nmm$. For the high-rate tests, the purely elastic definition of the aluminium does not correlate with the experimental findings. The yielding of the aluminium material is, therefore, assumed to be satisfactorily approximated.

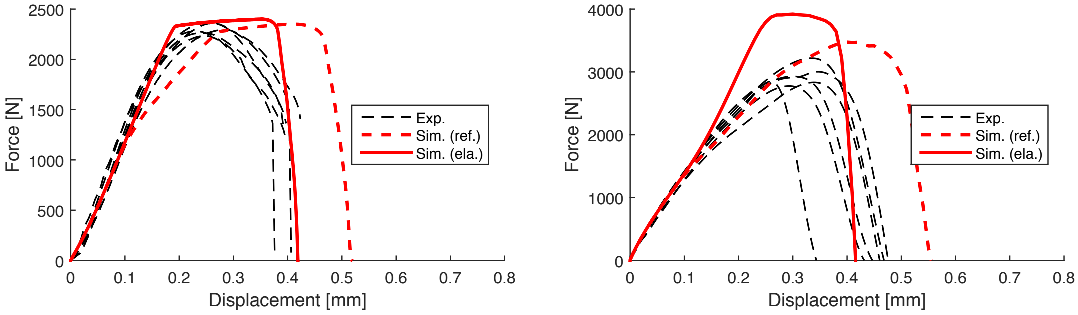

Figure 5-27 Force-displacement curve of CFRP-aluminium SLJ tests with purely elastic modelling of the aluminium material in the quasi-static case at $1.5\mu m/s$ (left) and the high-rate case at $2.0m/s$ (right).

The maximum force in the quasi-static SLJ experiments was overestimated with 17% by the simulation for the CFRP-CFRP SLJ and 4.3% in CFRP-aluminium SLJ with purely elastic properties of the aluminium. Additionally, the coefficient of variation was 11.0% in the quasi-static CFRP-CFRP SLJ experiments compared to 2.3% in the CFRP-aluminium SLJ experiments. Investigating the fracture surfaces of the quasi-static CFRP-CFRP SLJ, voids were found at the edge of the overlap for some specimen. Those voids were shown in Fig. 5-17. Taking out the specimen suffering under these voids, the correlation between experiments and simulation is improved significantly. The two remaining test results with the simulation are shown in Fig. 5-28. The error between simulation and experiments is then reduced to 6.0% regarding the maximum force.

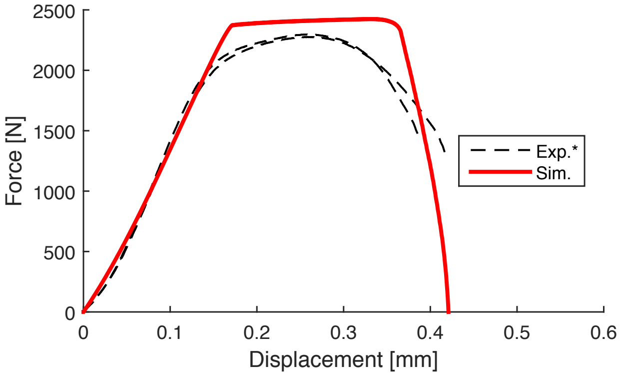

Figure 5-28 Comparison between the simulation of the CFRP-CFRP SLJ and the corresponding experiments that have low amount of voids at the quasi-static loading rate ($1.5\mu m/s$).

The strength in the SLJ simulations was generally overestimated as shown in Fig. 5-29. Various reasons for this can be found. Firstly, voids in the center of the bonding area have not been taken into account which can influence the maximum force. Secondly, a transverse contraction of the adherends could influence the stress state in the adhesive and its mechanical behaviour. The ultimate tractions were taken from butt joint tests and lap shear tests with steel adherends which have a higher stiffness in transverse direction of a factor 23 compared to the CFRP adherends and a factor of 3.0 compared to the aluminium adherends. In fact, the error between simulation and experiments in the CFRP-CFRP SLJ is slightly higher than in the CFRP-aluminium joints.

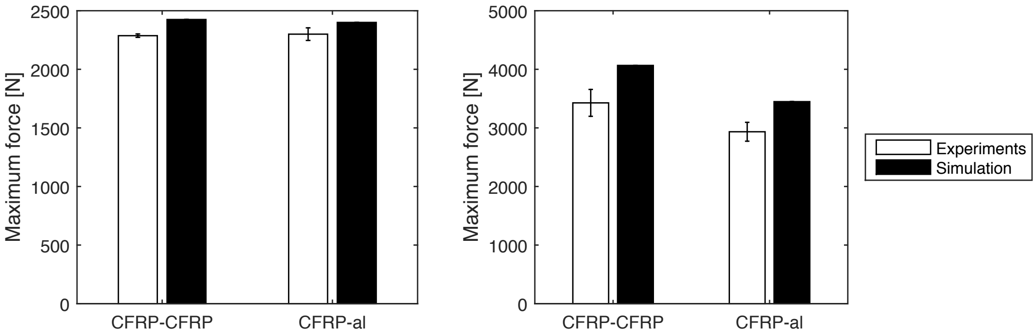

Figure 5-29 Comparison of the maximum forces of the simulation with experiments in the quasi-static case (left) and the high-rate case (right).

The sensitivity of the SLJ simulation to the cohesive law properties is investigated in Fig. 5-30. Fig. 5-30 (left) shows the influence of a variation of the ultimate traction τ_u by ±10%. Fig. 5-30 (right) shows the influence of a variation of the fracture energy J_c by ±10%. Table 5-5 shows the influence of the cohesive law properties τ_u and J_c on the strength and energy absorbed in the quasi-static CFRP-

CFRP SLJ simulations. It can be seen, that the ultimate traction τ_u is directly related to the maximum force of the SLJ simulation and J_c is directly related to the energy absorbed of the joint. Both influences are independent, i.e. τ_u does not influence the energy absorbed and J_c does not influence the maximum force. This is in contrast with [13, 14], who stated that the fracture energy of the adhesive has a significant influence on the strength of bonded joints. However, they used joints with relatively long overlaps, i.e. a low ratio of bondline thickness to overlap length.

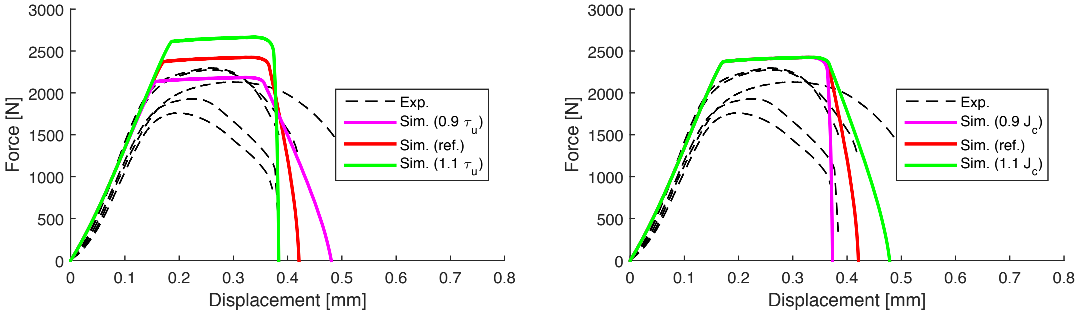

Figure 5-30 Sensitivity of the simulation on the cohesive law properties at the quasi-static loading rate ($1.5\mu m/s$): Ultimate traction τ_u (left) and J_c (right).

Table 5-5 Sensitivity of the simulation on the cohesive law properties τ_u and J_c.

τ_u	Max. force	Energy abs.	J_c	Max. force	Energy abs.
0.9	90.1%	100.1%	0.9	100.0%	90.3%
1.0	100.0%	100.0%	1.0	100.0%	100.0%
1.1	109.9%	100.0%	1.1	100.0%	110.0%

From the sensitivity study, it is discovered, that the ultimate tractions of the cohesive law bears some errors. This is confirmed by the mixed-mode loading experiments of section 3.4. In order to reduce the ultimate tractions of the cohesive law, the exponent of the mixed-mode interaction is varied from $\mu = 1.0$ to $\mu = 2.0$. The variation is simultaneously applied to the mixed-mode degradation initiation of eq. (5-11) and the start of softening of eq. (5-13). Fig. 5-31 shows the influence of the mixed-mode exponent on the mixed-mode cohesive law compared to the scarf joint experiments. The stiffness is unaffected by the modification, but the ultimate traction and ultimate separation are changed. To meet the experiments a value of $\mu = 1.4$ is used for simulation.

Fig. 5-32 shows the effect of the adjusted exponent $\mu = 1.4$ on the simulation of the quasi-static CFRP-CFRP SLJ and CFRP-aluminium SLJ compared to the experiments. The error for the CFRP-CFRP SLJ simulation reduces to 2.7% and

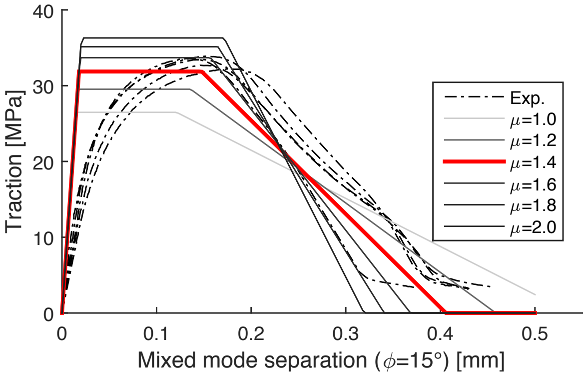

Figure 5-31 Variation of the mixed-mode exponent μ and experimental results of the combined loading test.

for the CFRP-aluminium SLJ to 0.7%. For the high-rate experiments according to Fig. 5-33, the error in the CFRP-CFRP SLJ reduces to 14% and in the CFRP-aluminium SLJ to 15%, respectively.

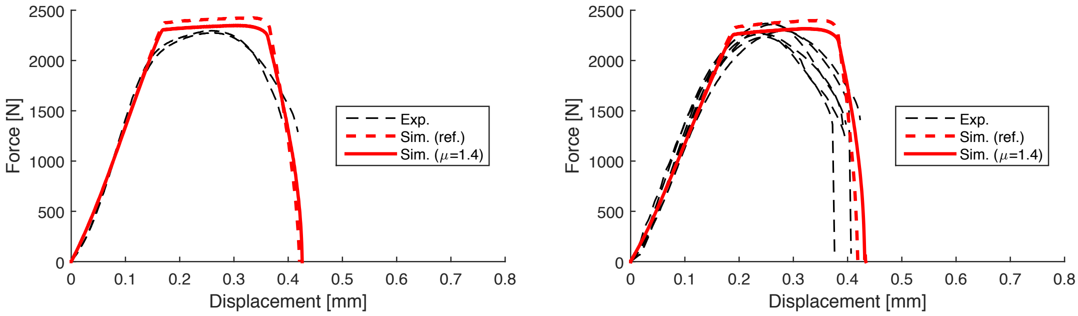

Figure 5-32 Simulation of the CFRP-CFRP SLJ (left) and the CFRP-aluminium SLJ (right) with mixed-mode exponent $\mu = 2.0$ and $\mu = 1.4$ compared to experiments at the quasi-static loading rate $(1.5\mu m/s)$.

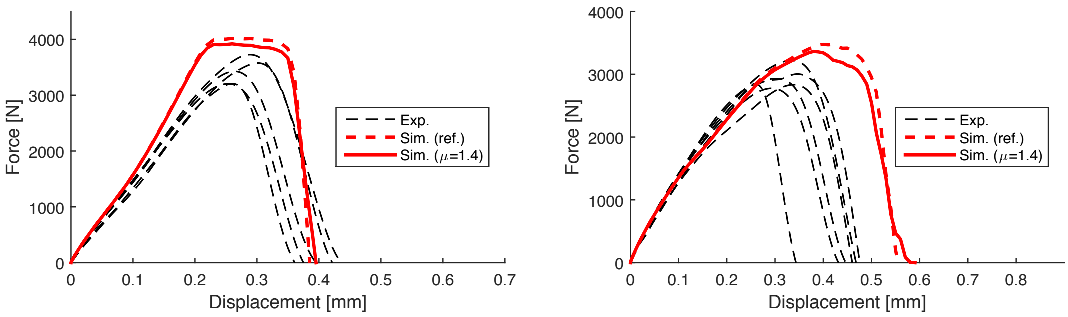

Figure 5-33 Simulation of the CFRP-CFRP SLJ (left) and the CFRP-aluminium SLJ (right) with mixed-mode exponent $\mu = 2.0$ and $\mu = 1.4$ compared to experiments at the high-rate loading $(2.0m/s)$.

While the static test correlate well with experimental findings, a higher error between simulations and experimental results was found in the high-rate tests. Generally, voids at the edge of the overlap and randomly distributed over the bonding area or partly delaminated joints are believed to reduce the joint strength in the experiments. Additionally, errors could be due to the highly different loading rates for the characterisation of the cohesive behaviour of the adhesive. Additional testing of the adhesive at intermediate loading rates could increase the accuracy of the simulations. Moreover, accurate testing methods to measure the fracture energy of adhesives at high loading rates are desired.

5.3 Testing and simulation of a T-joint sub-component

In this section, the cohesive behaviour of the adhesive is validated on a sub-component level. The testing of a T-joint is outlined in the first section 5.3.1. The numerical modelling and 3D simulation is described in section 5.3.2. Results will be presented and discussed in section 5.3.3.

5.3.1 Specimen geometry and testing

A representative T-joint sub-component is shown in Fig. 5-34. The geometry consisted of a $300mm$ long hat profile made out of $1.5mm$ sheet steel at the bottom of the joint. The hat profile was closed by a flat sheet steel, which was spot welded to the bottom of the hat profile. A CFRP-aluminium bond was realised in the T-joint subcomponent. The CFRP adherend consisted of an L-shaped profile with a wall thickness of $2mm$ and was bonded on top of the steel hat profile. The length of the CFRP L-profile was $190mm$, the height and width of the L-profile was $39mm$ and $70mm$, respectively. The layup of the CFRP laminate was $[+45/-45/-45/+45/0/90/90/0]_s$. The prepreg IM7-8552 was used for a single ply. The thickness of the bond between steel and CFRP as well as the adhesive material are assumed very thin and quasi-rigid. Another hat profile with a length

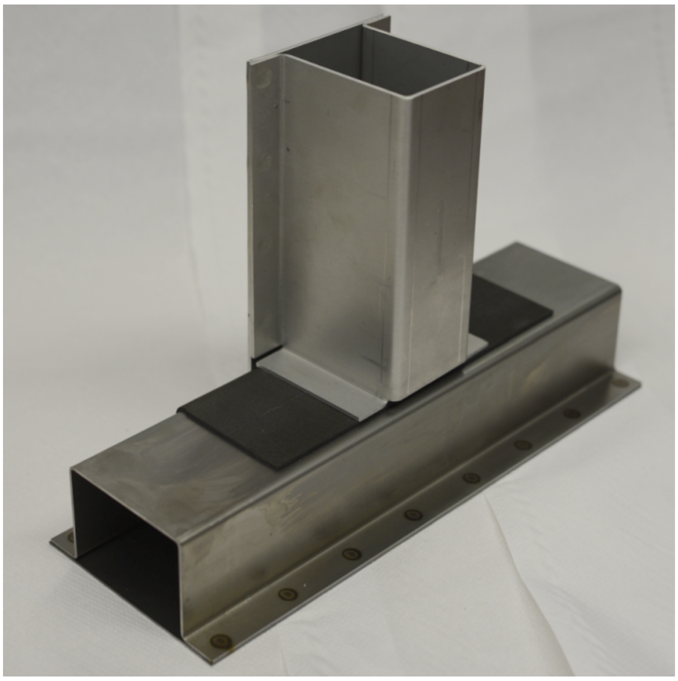

Figure 5-34 Assembly of the T-joint subcomponent.

of $150mm$ made out of a 6000 series aluminium with a thickness of $2mm$ was bonded by two flanges perpendicular to the CFRP L-profile. This hat profile was again closed by a flat sheet aluminium of the same type and thickness, which has been spot welded to the hat profile and bonded to the CFRP L-profile. The adhesive thickness between the CFRP-aluminium bond was $0.3mm$. The adhesive Betamate™ 1480 V203 was used for this bondline. The bonding area of the sheet aluminium to CFRP L-profile was $19.5x29mm^2$ and the two bonding areas between the aluminium hat profile and CFRP L-profile were $19.5x33mm^2$ each. All bonding areas were located in the middle of the corresponding aluminium flange. It is worth noticing at this point, that all adhesive bonds ended with a spew fillet. Spew fillets can have a significant influence on the strength of bonded joints [109, 110].

The T-joint was loaded by a solid steel impactor with a radius of $50mm$. The loading velocity for quasi-static testing was $10mm/min$ and for dynamic testing $1.2m/s$. The loading direction was parallel to the length axis of the steel hat profile. The impactor hit an aluminium plate attached to the side of the aluminium hat profile. In order to avoid a collapse of the aluminium hat profile, the inner part was stiffened with an expanding aluminium core. The steel hat profile was fixed with $30mm$ broad steel clamps at both ends to the support of the testing machine. On the side of the flat sheet aluminium and CFRP L-profile, a speckle pattern was sprayed to enable a DIC evaluation of the T-joint deformation. The T-joint sub-component was manufactured and tested in a drop tower at the "Lehrstuhl für Werkstoff und Fügetechnik" (LWF) at the University of Paderborn.

The forces were measured by a load cell in the impactor. The deformations in terms of displacements were measured at the impactor for the quasi-static tests. For the high-rate tests, a high-speed camera with subsequent evaluation of the pictures via DIC was used. Then, deformations were evaluated in terms of a relative rotation of both hat profiles. The force-displacement curve in the quasi-static experiments was recorded with a rate of $50Hz$ leading to 3600 data points up to failure. In the dynamic experiments, an acquisition rate of approximately $250000Hz$ was achieved with about 1000 data points up to failure. Four quasi-static tests and two dynamic experiments were performed.

5.3.2 Numerical evaluation

A 3D FE-model was build up according to the T-joint experiments. The steel material was modelled by an isotropic linear elastic material with a Young's modulus of $210GPa$ and a Poisson ratio of 0.3. The quasi-static properties of the aluminium and the CFRP were defined according to section 5.2.2. A composite layup for shells was used to define the orthotropic material behaviour of the CFRP. The shim of the three bonds was realised as shown in Fig. 5-35. The adhesive thickness followed the radius of the flanges of the aluminium hat profile so that the angle of the spew fillet reached 55°. The adhesive bondline of $0.3mm$ was modelled with the mixed-mode rate-dependent cohesive law of section 5.1.2. For the spew fillet, the cohesive law for the $0.3mm$ bondline was adapted to a stress-strain relation by

$$\epsilon_{F,i} = \frac{\delta_i}{T_F}. \tag{5-23}$$

where $\epsilon_{F,i}$ denotes the strain of the spew fillet in the loading directions $i = I{,}II{,}III$ and T_F denotes the thickness of the fillet defined by the nodal coordinates of the cohesive elements.

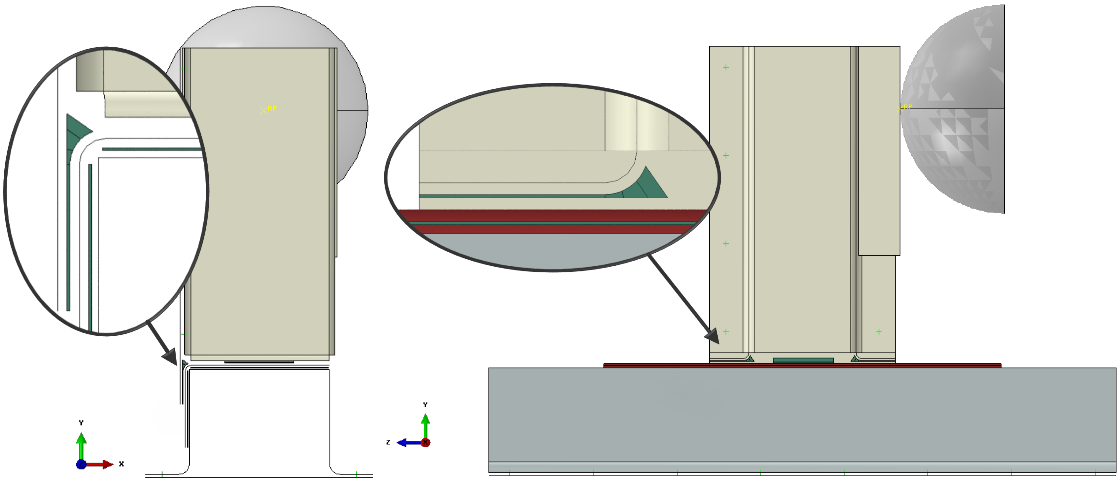

Figure 5-35 Modelling of the spew fillets and the adhesive bondlines.

The adhesive bondline between the sheet aluminium, the aluminium hat profile and the CFRP L-profile was modelled with one layer of cohesive elements (COH3D8) over the complete bondline and spew fillet thickness. A mesh size of $2.0mm$ was chosen for the $0.3mm$ bondline. For the spew fillet the mesh size was set to $1.0mm$ in the direction of the radius, while it was kept $2.0mm$ in transverse direction. The reason for this refinement was, that the radius of the spew fillet needed a higher resolution to be adequately represented. The mesh of the adhesive bond is shown in Fig. 5-36. The adhesive bond between the steel hat profile and the CFRP L-Profile was realised by the same elements and a mesh size of $4mm$.

All shell elements were modelled by quadrilateral reduced integration linear shell elements (S4R) with enhanced hourglass control. The mesh size for the CFRP L-profile, the sheet aluminium and the aluminium hat profile was set to $4mm$, while the radii in the CFRP L-profile and the aluminium hat profile were resolved with $1mm$ in the direction of the radius. The sheet steel and the steel hat profile were meshed with a size of $8mm$. The impactor was modelled as discrete rigid shells with

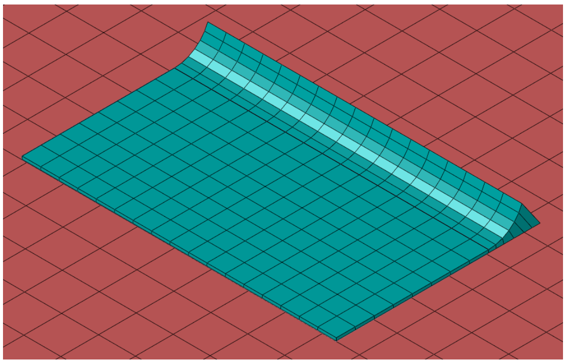

Figure 5-36 Mesh of the adhesive bondline.

a mesh size of $4mm$ with a mixed mesh of quadrilateral and triangular elements. The aluminium plate and the aluminium expander were modelled by linear reduced integration solid brick elements (C3D8R) with enhanced hourglass control and a mesh size of $4mm$ and $8mm$, respectively.

The spot welds were realised using the point-based fastener modelling in Abaqus/ Explicit. Thereby, mesh independent points on two surfaces were rigidly coupled in their translation and rotation by a distributed coupling constraint. The physical radius of the spot-welds was set to $5mm$. The cohesive elements representing the adhesive bondlines and the spew fillets were connected via surface tie-constraints to their adjacent surfaces. The aluminium expander was connected to all its adjacent surfaces and the aluminium plate was connected to the aluminium hat profile via surface tie constraints. The coupling of the impactor to the aluminium plate was realised via a frictionless penalty surface-to-surface contact. Both surfaces were initially in contact but a separation during the solution process was allowed. The support of the T-joint was modelled by fixing the nodes up to $30mm$ from the edges of the steel hat profile in all transverse directions. The load was applied by a smooth step velocity boundary condition of the reference point of the rigid impactor. A small amount of mass scaling was used to achieve a critical time-step of $1\mu s$ taking care not to change the mechanical response of the model. For the quasi-static loading a velocity of $0.1m/s$ and for dynamic loading a velocity of $1.2m/s$ was applied. The contact force was monitored between the impactor and the aluminium plate. The mesh and the boundary conditions of the T-joint model are shown in Fig. 5-37.

5.3.3 Results

The results of the quasi-static T-joint test compared to the simulation can be seen in Fig. 5-38. The stiffness of the simulation is well in the scatter of the experimental results. The maximum force in the simulation was $4804N$. The mean experimental

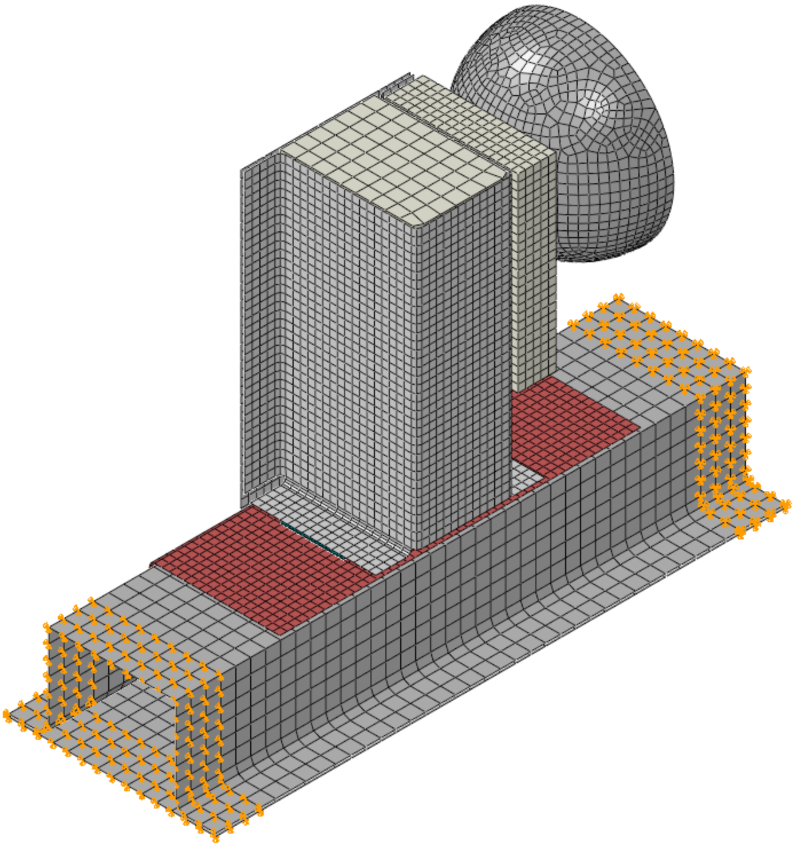

Figure 5-37 Mesh and boundary conditions of the T-joint model.

maximum force was 4725N with a standard deviation of 706N. The simulation is in very good agreement with the experiments with an error of 1.7%. The displacement to failure in the simulation is slightly higher than in the experiments. The experiments showed a mean energy absorbed of 15.7Nm with a standard deviation of 2.5Nm. The energy absorbed in the simulation was 13.6Nm and within the standard deviation of the experiments. The results show, that the simulation approximates well the quasi-static behaviour of the T-joint.

A comparison between simulation and the dynamic experiments is shown in Fig. 5-39. Large oscillations can be seen at the beginning of the experimental curves. These oscillations are assumed to come from inertia in the test set-up. Through the smooth step boundary condition, these oscillations could be suppressed in the simulations. It can be seen that the T-joint stiffness in the simulation approximates the stiffness in the experiments. The maximum load in the simulation is 6826N which is 17% lower than the mean maximum load of 8227N in the experiments. The rotation at failure of the simulation is comparable to the experiments.

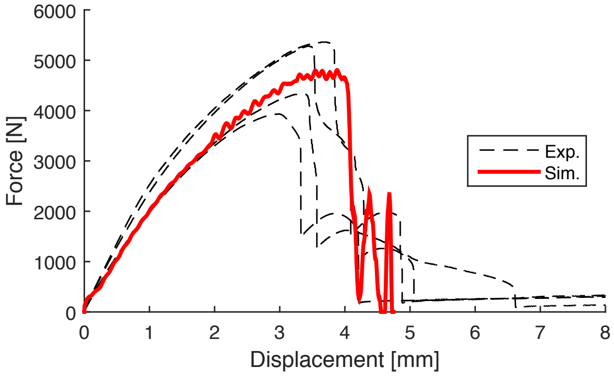

Figure 5-38 Force-displacement curve of the T-joint experiments and simulation for quasi-static loading ($10 mm/min$).

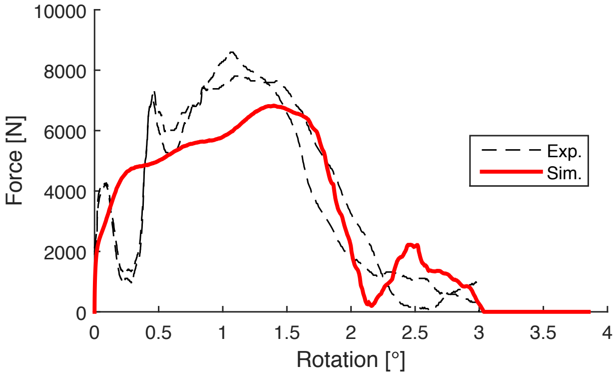

Figure 5-39 Force-rotation curve of the T-joint experiments and simulation for dynamic loading ($1.2 m/s$).

5.3.4 Discussion

It was found in the section 5.2.4 that the aluminium material properties bear errors especially for the quasi-static simulation. The sensitivity of the T-joint simulation to the aluminium properties are, therefore, investigated. Fig. 5-40 shows the influence of a purely elastic modelling of the aluminium on the results of the simulation. It can be seen that for the quasi-static simulation the maximum force is increased while for the dynamic simulation the maximum force remains approximately constant. Compared to the CFRP-aluminium SLJ, the influence of the aluminium material modelling is small in this case.

Figs. 5-41 and 5-42 show the influence of the cohesive law variation on the T-joint simulation results. The ultimate tractions as well as the fracture energy were varied by ±10%. Table 5-6 shows the percent change of the maximum force in the simulations. It can be seen, that both the ultimate tractions as well as the fracture energy of the cohesive law positively correlate with the maximum force of the T-joint simulation. However, the percent change of the maximum force is

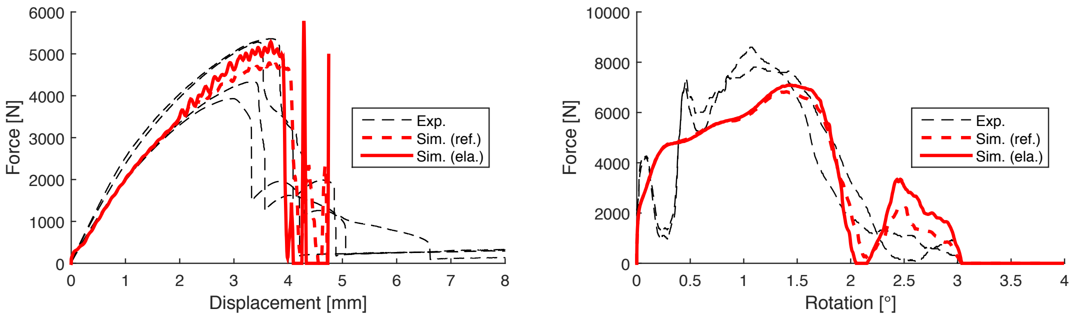

Figure 5-40 Influence of the aluminium material properties on the simulation of the T-joint for the quasi-static loading rate of $10mm/min$ (left) and the high-rate loading of $1.2m/s$ (right).

significantly decreased compared to the variation of the cohesive law. For the high-rate experiments, the error in the simulation can be due an uncertainty in the cohesive law.

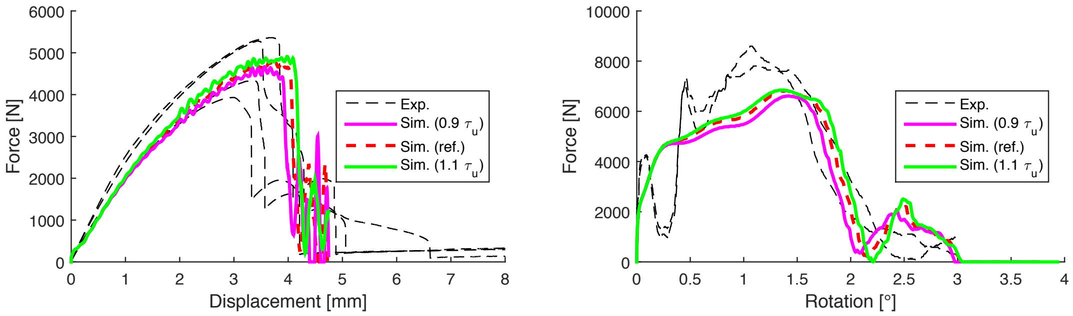

Figure 5-41 Influence of the ultimate traction of the cohesive law on the simulation results of the T-joint for the quasi-static loading rate of $10mm/min$ (left) and the high-rate loading of $1.2m/s$ (right).

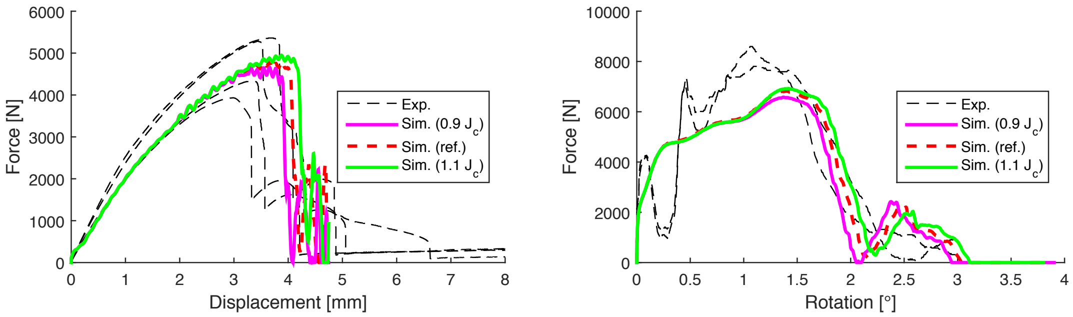

Figure 5-42 Influence of the fracture energy on the simulation results of the T-joint for the quasi-static loading rate of $10mm/min$ (left) and the high-rate loading of $1.2m/s$ (right).

The modelling of the spew fillet was reported to have a significant influence on the experimental and simulation results. To identify this contribution one simula-

Table 5-6 Sensitivity of the maximum force in the high-rate T-joint simulation on the cohesive law properties τ_u and J_c.

τ_u	Static	High-rate	J_c	Static	High-rate
0.9	97.16 %	96.9 %	100.0%	96.97 %	96.39 %
1.0	100.0 %	100.0 %	100.0%	100.0 %	100.0 %
1.1	102.15 %	100.4 %	100.0%	103.05 %	101.46 %

tion without spew fillet and one simulation with a 90° spew fillet were performed and compared to the experiments and reference simulation. Fig. 5-43 shows that the spew fillet dramatically changes the structural response. Since no information about the shape of the spew fillet was available, a significant uncertainty lies in the simulation at this point. Moreover, the mechanical behaviour of the spew fillet was estimated based on the experimental characterisation of the $0.3mm$ bondline.

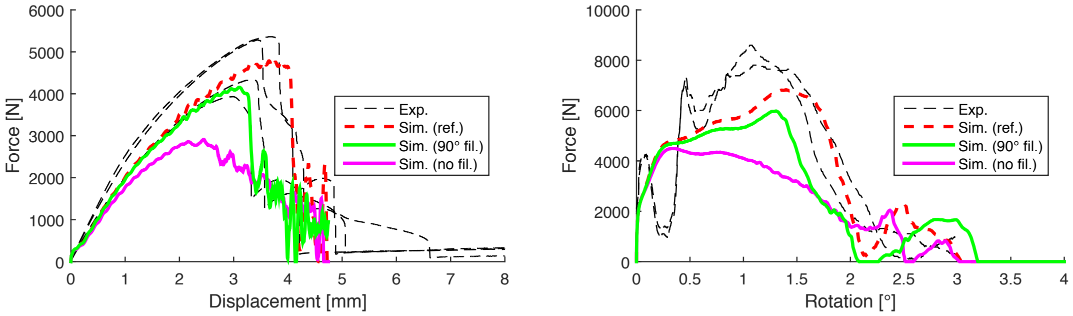

Figure 5-43 Influence of the spew fillet on the simulation results of the T-joint for the quasi-static loading rate of $10mm/min$ (left) and the high-rate loading of $1.2m/s$ (right).

For the dynamic experiments, the inertia effects in the experiments could influence the maximum force. The effect of the loading amplitude is, therefore, investigated. Fig. 5-44 shows the simulation results for a $2.0ms$, $3.0ms$, $5.0ms$ amplitude of the smooth step boundary condition and the reference simulation with $4ms$ compared to the experimental results. It can be seen, that the mechanical response of the simulation can change significantly, when inertia effects arouse. The exact representation of the experimental set-up is, however, difficult since the compliance of the boundary conditions are not known for the simulation.

5.4 Summary of the chapter

In this chapter the mixed-mode rate-dependent cohesive law for the adhesive Betamate™ 1480 V203 was formulated and calibrated based on the experimental findings of chapter 3. The stiffness and ultimate tractions in normal mode N and shear

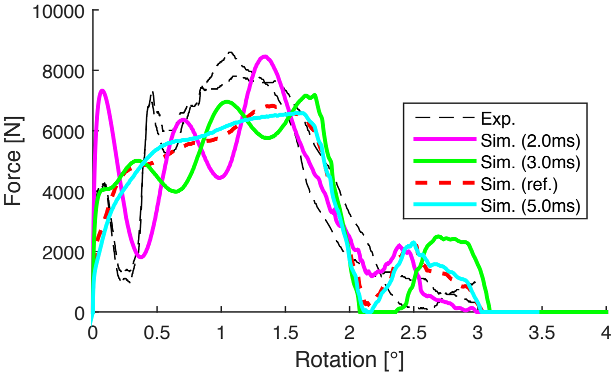

Figure 5-44 Influence of the loading amplitude on the simulation results of the T-joint for the high-rate loading of $1.2m/s$.

mode S were determined by butt joint and lap shear tests for quasi-static and high loading rates. The fracture energy was quasi-statically determined using the mean maximum J-integral value of the DCB and ENF tests according to Stigh et al. [55]. The high-rate fracture energies were extrapolated based on the energy absorbed of the butt joint and lap shear tests.

The mixed-mode behaviour of the adhesive bondline was validated for quasi-static loading rates with the combined loading test of section 3.4. While the fracture energy correlated well with a linear variation of the pure mode quantities, inaccuracies in the mixed-mode stiffness and ultimate tractions were found. The rate-dependent behaviour of the cohesive law was calibrated with the butt joint tests at intermediate loading rates. A quadratic logarithmic interpolation of the cohesive tractions with respect to the rate of deformation agreed well with the experiments.

The cohesive law was validated in a 2D simulation of CFRP-CFRP and CFRP-aluminium SLJ experiments. Both joint types were tested and simulated for quasi-static loading at $1.5\mu m/s$ and high-rate loading at $2.5m/s$. Cohesive failure of the adhesive was generally present in the experiments. The simulation results showed, that the stiffness in the quasi-static tests of both joint types was in good correlation with the experiments. In the CFRP-CFRP SLJ, the simulation overestimated the maximum force. Voids were however found on the fracture surface of the bond. Specimen with a significant amount of voids were taken out of the study and a better correlation was found. In the CFRP-aluminium joints, the aluminium yielding lead to an overestimation of the energy absorbed by the simulation. This could be overcome assuming a linear elastic material behaviour of the aluminium. By an adaptation of the mixed-mode interaction criterion of the cohesive law formulation, the simulations could be better correlated with the experimental results than using the standard quadratic mixed-mode interaction criterion.

In the high-rate SLJ simulations the initial stiffness correlated well with the experiments but the maximum force was overestimated. The reason for this error was assumed to be due to voids in the bondline of the specimen and additional small delaminations in the experiments, that could decrease the experimental maximum force. On the other hand, the cohesive law formulation and calibration could lead to the overprediction.

A validation of the cohesive law by a T-joint sub-component showed a good correlation with the experiments for the quasi-static loading rate. The dynamic simulations approximated the T-joint stiffness, but underestimated the maximum force in the experiments. A small sensitivity of the maximum force on the ultimate tractions and fracture energy of the cohesive law was found. The modelling of the spew fillet and inertia effects were however found to strongly influence simulation results.

The mixed-mode cohesive law formulated and calibrated in this chapter turned out to give accurate results for quasi-static loading conditions in 2D and 3D simulations. For high loading rates, an error in the range of +15% or -17% in the joint strength occurred, but it cannot be clearly traced back to an error in the cohesive law. Defects in the bonding area like voids or delaminations on the one hand, the spew fillets and inertia effects on the other hand make a proper conclusion difficult.

6 Simulation of delamination failure in bonded joints

In chapter 5, experiments and simulation methods have been outlined to represent cohesive failure of a bonded joint in quasi-static and high-rate loading conditions. The out-of-plane failure of the FRP adherend, which will be treated as a delamination failure in the following, is another relevant failure mode of bonded joints and can have a crucial influence on the mechanical response of a bonded joint. Since the delamination failure process in bonded joints takes place between the single plies of the laminated adherend, a high resolution of the model would be necessary which would make the simulation of a complete car structure difficult to solve in adequate time. The following contents were published by the author [111].

The prediction of delamination failure in bonded joints has been addressed by several works using numerical approaches. There have been 2D and 3D continuum models to study the stress distributions, stress intensity factors and energy release rates in pre-cracked bonded joints [112–114]. The models are very useful to study the locations of crack initiation in bonded joints, the criticality of existing cracks and crack sizes and the influence of joint design parameters. However, a high resolution of the mesh has been necessary and dynamic crack propagation has not been simulated in the studies. The models are, therefore, not suitable for crash simulations.

CZM has turned out to be a computational efficient technique to model the dynamic crack propagation along a predefined interface [32, 34, 115]. It has been applied to the simulation of delamination crack growth [29, 116] and to the modelling of cohesive failure in adhesive layers [12, 39]. An explicit formulation has been presented for the simulation of adhesive bondlines in crash structures with high numerical efficiency [17].

Delamination failure in bonded joints can occur by a kinking of an existing crack from the adhesive into the adherends or the delamination crack can develop directly in the adherends. Li et al. [117] studied the kinking of a crack into an adherend with random-oriented fibres. The adherends were modelled by continuum elements and the adhesive by one layer of cohesive elements over the complete bondline thickness. A CZ perpendicular to the bondline was introduced in the adherends to model the kinking of the crack. The CZ in the adherend was modelled $10mm$ long to keep the size of the simulation model small. When the adherend crack reached the end of the CZ the model was re-meshed.

Campilho et al. [118] studied the damage growth in single and double lap joints using CZs in the adherend for delamination failure, in the adherend/adhesive interface, within the adhesive and at the adhesive/patch interface of a repaired structure. The CZs were placed in a 2D plane strain continuum model. An additional CZ was introduced perpendicular to the bondline and the first delamination interface to account for a dynamic intra-ply failure of the first ply next to the adhesive. Modifying the strength properties of the cohesive laws, the location of failure was observed at different locations, while the fracture energies of adhesive and delamination were found to have a minor influence. In the case of delamination failure, the outer ply of the laminate adherend which is attached to the adhesive delaminated.

Neto et al. [119] set up a 2D model of a SLJ with laminated adherends. The adhesive bondline was modelled by one CZ over the complete bondline thickness. The dynamic crack growth in the delamination interface was modelled with a second CZ parallel and close to the adhesive bondline. For all CZs a triangular mixed-mode cohesive law was used. The simulation model was compared for a ductile and brittle adhesive and for various overlap length with analytical solutions and experiments. The failure mode of the numerical model correlated well with the experimental findings. For the brittle adhesive, delamination failure occurred for long overlap length which was non-conservatively approximated by the numerical model. For the ductile adhesive, cohesive failure of the adhesive occurred which was underestimated by the numerical model due to the simplified shape of the cohesive law.

The studies mentioned [117–119] use continuum elements for the adherends with CZs introduced for possible crack interfaces. This type of modelling still leads to high computational costs and modelling effort, if at all feasible on a full scale structure. In order to reduce the model size, the laminated adherends can be modelled by shell structures. Dávila et al. [120] introduced the concept of CZs for shell elements. This concept was applied to bonded composite joints by Rauh [47]. In the later work, the cohesive behaviour of the adhesive in a bonded tube specimen and in a double hat structure was modelled via one CZ over the complete bondline thickness. The laminate was split into two sub-laminates represented by shell elements and connected via a CZ representing the dynamic crack growth in the delamination interface. Using this modelling approach, the model size was significantly reduced. A further reduction to one shell element for the complete adherend and only one CZ for the complete adhesive bondline was, however, desired.

In this case, the delamination failure can be integrated either in the shell formulation of the adherend or into the CZ. Since conventional shell elements do not provide degrees of freedom in the thickness direction, the CZ is chosen. Then, the delamination failure can be integrated in two ways into the CZ. The cohesive law can be calibrated empirically by experiments failing by delamination. In [47], single lap shear experiments showing a mixture of delamination and cohesive failure of the adhesive have been used to inversely calibrate the cohesive law. The problem using this method is that an appropriate calibration for different joint geometries, loading conditions and loading rates is difficult to find and a high experimental effort can arouse.

In the following, a formulation for a cohesive element that models the cohesive behaviour of the adhesive and integrates the delamination failure is presented. This is a new approach compared to state-of-the-art simulation with conventional CZs that only model the cohesive behaviour of the adhesive. With the new formulation, the adherends can be modelled via conventional shell elements and the simulation model can be significantly reduced. This is illustrated in Fig. 6-1.

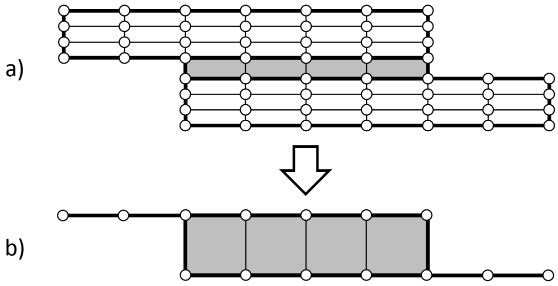

Figure 6-1 a) Conventional CZ model: The adherend is modelled by continuum elements with optional delamination interfaces for the simulation of dynamic crack growth in the adherend; b) Model reduction with one CZ over the complete adhesive thickness including delamination failure [111].

In section 6.1, the formulation of the element is presented. In section 6.2.1 and 6.2.2, a numerical study of a SLJ is carried out comparing the new element with the conventional modelling. The accuracy of the new element as well as its computational performance is investigated.

6.1 Element formulation

The formulation focuses on the 2D case with the cohesive element representing the complete bondline thickness of a bonded joint. Fig. 6-2 shows the degrees of freedom (DOFs) of the element which has two translational and one rotational DOF at each node, i.e. $\boldsymbol{d}_K = [v_K, w_K, \varphi_K]$. Since the element is connected to a beam-like structure in the 2D case, the displacements on each side of the adhesive bondline are determined with the help of a metric tensor $\Xi^{\pm}$.

$$\boldsymbol{u}^{\pm} = \Xi^{\pm}\boldsymbol{d} \tag{6-1}$$

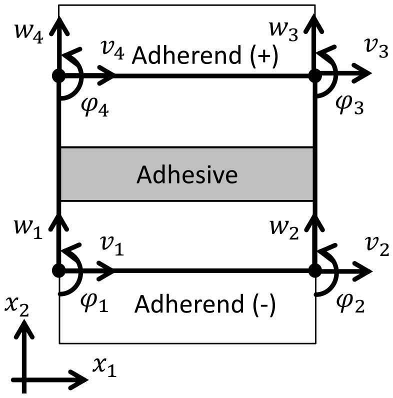

Figure 6-2 Degrees of freedom for the cohesive element [111].

According to [17], the metric tensor is defined by

$$\Xi_{ij}^{-} = \begin{bmatrix} 1 & 0 & -h^{-}/2 \\ 0 & 1 & 0 \end{bmatrix} \qquad \Xi_{ij}^{+} = \begin{bmatrix} 1 & 0 & h^{+}/2 \\ 0 & 1 & 0 \end{bmatrix} \tag{6-2}$$

where $h^{\pm}$ denotes the height of the beam elements on each side of the bond. The element internal force vector of eq. (2-31) has to be adapted accordingly.

$$\boldsymbol{f}_{int}^{(el)} \approx \int_{\Gamma_c} (\boldsymbol{N}^{\pm})^T (\boldsymbol{\Xi}^{\pm})^T \boldsymbol{\Theta}^T \boldsymbol{S} \boldsymbol{\Theta} \boldsymbol{\Xi}^{\pm} \boldsymbol{N}^{\pm} d\Gamma_c \boldsymbol{d} \tag{6-3}$$

The representation of delamination failure in the CZ is realised by the definition of the cohesive law of eq. (2-28). It is assumed that the joint's mechanical behaviour is dominated by the adhesive's cohesive behaviour initially while through thickness effects of the adherends are neglected for simplicity. Therefore, the initial cohesive behaviour is defined by the adhesive's cohesive law. It is additionally assumed, that the delamination behaviour influences the joint's mechanical behaviour as soon as the stress state in the adherends becomes critical and a delamination starts to grow. The adhesive's mechanical behaviour is modelled by a general formulation of a cohesive law.

$$\tau_i = (1 - d_i) K_i \delta_i \qquad (\textit{no sum in } i) \tag{6-4}$$

where d_i is a stiffness degradation variable and K_i is the stiffness of the cohesive law which is defined by eq. (5-3). The index i denotes the opening direction of the bondline with $i = N{,}S$ for normal and shear opening, respectively. The degradation variable d_i is generally given through any function of the separation δ_i here.

$$d_i = f(\delta_i) \tag{6-5}$$

In this way, an arbitrary shape of a cohesive law can be defined in shear and normal direction. If a compressive load is acting on the adhesive, the normal traction is determined by eq. (5-18). For mixed-mode loadings the linear interaction criterion according to eq. (5-14) is used. J_N and J_S are here the work absorbed in normal and shear direction [40].

$$J_N = \int_0^{\delta_N} \tau_N d\tilde{\delta}_N \qquad J_S = \int_0^{\delta_S} \tau_S d\tilde{\delta}_S \tag{6-6}$$

It has been discovered that the delamination failure in bonded joints is rather sensitive to the strength of the adhesive bondline and the delamination interface than to the fracture energies [118]. For delamination initiation, a quadratic stress based initiation criterion is chosen, which has been extensively applied to the modelling of delamination failure [28, 29].

$$\left(\frac{\sigma_{22}}{\sigma_{22}^0}\right)^2 + \left(\frac{\sigma_{12}}{\sigma_{12}^0}\right)^2 = 1 \tag{6-7}$$

Here, σ_{22} and σ_{12} are the through thickness tensile and shear stresses and σ_{22}^0 and σ_{12}^0 are the through thickness tensile and shear strength in the adherend, respectively. σ_{22}^0 and σ_{12}^0 also refer to the ILTS and the ILSS. The through thickness tensile and shear stresses are computed within the new cohesive element analytically. Therefore, the new cohesive element needs the materials, layup and orientation of its adherends as additional input parameters. The analytical calculation of σ_{22} and σ_{12} are described in the following.

In the 2D case, the adherend can be seen as a layered beam subjected to in-plane and transversal forces and surface tractions. The surface tractions are due to the adhesive stresses applied to the beam surface. In Fig. 6-3 an infinitesimal slice of the beam element is illustrated.

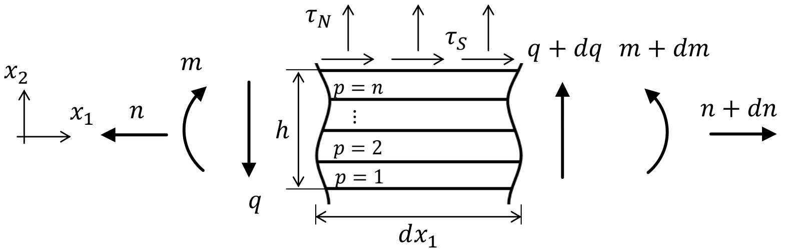

Figure 6-3 Infinitesimal section of the laminated beam subjected to surface tractions [111].

The balance of forces for the infinitesimal beam element yields

$$\frac{\partial n}{\partial x_1} = -\tau_S \qquad \frac{\partial q}{\partial x_1} = -\tau_N \qquad \frac{\partial m}{\partial x_1} = 0.5\tau_S h - q \tag{6-8}$$

where n, q and m are the normal load, shear load and moment load per width of the beam. h denotes the height of the beam and τ_S is the tangential and τ_N the normal surface traction, respectively. The through thickness stress distribution is calculated by [121]

$$\sigma_{12}(x_2) = \tau_S + \int_{x_2}^{h/2} \frac{\partial \sigma_{11}}{\partial x_1} d\tilde{x}_2 \tag{6-9}$$

$$\sigma_{22}(x_2) = \tau_N + \int_{x_2}^{h/2} \frac{\partial \sigma_{21}}{\partial x_1} d\tilde{x}_2 \tag{6-10}$$

where $d\sigma_{11}/dx_1$ and $d\sigma_{21}/dx_1$ are the normal and shear stress gradient of the beam in x_1-direction, respectively. Assuming a linear variation of the strain over the beam thickness, the normal stress gradient is approximated by

$$\frac{\partial \sigma_{11}}{\partial x_1} = E_p \left[\frac{\partial \epsilon^0}{\partial x_1} - \frac{\partial \kappa}{\partial x_1} x_2 \right] \tag{6-11}$$

where E_p is the Young's modulus of the p-th layer in the beam, ϵ^0 is the membrane strain and κ is the curvature of the beam. The gradient of the membrane strain and the curvature are computed from

$$\frac{\partial}{\partial x_1} \begin{bmatrix} \epsilon^0 \\ \kappa \end{bmatrix} = \begin{bmatrix} a & b \\ b & d \end{bmatrix} \frac{\partial}{\partial x_1} \begin{bmatrix} n \\ m \end{bmatrix} \tag{6-12}$$

where a, b and d are the components of the inverse stiffness matrix of a layered beam according to classical lamination theory [108]. The gradients dn/dx_1 and dm/dx_1 have been defined by eq. (6-8). The shear load per width q is determined by the evaluation of the nodal displacements of the cohesive element with the stiffness matrix of a linearly interpolated Timoshenko beam element [24].

$$q = \frac{1}{w} \left(\frac{\chi G A}{\Delta l_{12}} w_1 + \frac{\chi G A}{2} \varphi_1 - \frac{\chi G A}{\Delta l_{12}} w_2 + \frac{\chi G A}{2} \varphi_2 \right) \tag{6-13}$$

where w defines the width and χGA the transverse shear stiffness of the beam, respectively. Δl_{12} denotes the distance between two nodes parallel to the crack plane of the cohesive element. By integration of eq. (6-9), the through thickness shear stresses for a laminated beam can be determined.

To determine the through thickness tensile stresses $\sigma_{22}(x_2)$, eq. (6-9) is inserted into eq. (6-10) setting $\sigma_{21} = \sigma_{12}$. Subsequent derivation with respect to dx_1 gives

$$\sigma_{22}(x_2) = \tau_N + \int_{x_2}^{h/2} \int_{\tilde{x}_2}^{h/2} \frac{\partial^2 \sigma_{11}}{\partial x_1^2} d\tilde{x}_2 d\tilde{x}_2 \tag{6-14}$$

The second derivation of the membrane stresses σ_{11} with respect to dx_1 is given by

$$\frac{\partial^2 \sigma_{11}}{\partial x_1^2} = E_p \left[\frac{\partial^2 \epsilon^0}{\partial x_1^2} - \frac{\partial^2 \kappa}{\partial x_1^2} x_2 \right] \tag{6-15}$$

with

$$\frac{\partial^2}{\partial x_1^2} \begin{bmatrix} \epsilon^0 \\ \kappa \end{bmatrix} = \begin{bmatrix} a & b \\ b & d \end{bmatrix} \frac{\partial^2}{\partial x_1^2} \begin{bmatrix} n \\ m \end{bmatrix} . \tag{6-16}$$

Since the second derivation of the normal load n is equal to zero, the second derivation of the moment load yields

$$\frac{\partial^2 m}{\partial x_1^2} = -\frac{\partial q}{\partial x_1} = \tau_N \tag{6-17}$$

Inserting eq. (6-17) into eq. (6-16) and subsequently into eqs. (6-15) and (6-14), the through thickness tensile stresses $\sigma_{22}(x_2)$ for a laminated beam can be determined. $\sigma_{12}(x_2)$ and $\sigma_{22}(x_2)$ are used then in eq. (6-7) as a measure for delamination initiation in the first adherend. The calculations for the second adherend are done accordingly and checked for delamination initiation as well.

As soon as delamination initiation is detected in any of both adherends, a strategy to account for delamination crack propagation is defined adapting the mixed-mode fracture criterion from eq. (5-14).

$$\frac{J_N}{J_N^* + J_{Ic,del}} + \frac{J_S}{J_S^* + J_{IIc,del}} = 1 \tag{6-18}$$

Here J_N^* and J_S^* represent the work done by the adhesive at delamination initiation and $J_{Ic,del}$ and $J_{IIc,del}$ represent the fracture energy of the delamination in mode I and mode II.

The solution process of the boundary value problem is shown in Fig. 6-4. The problem is given as a FE mesh with initial and boundary conditions. Firstly, the mass matrix of the elements is calculated and added to the global mass matrix $\boldsymbol{M}$ of eq. (2-13). The mass matrix of an cohesive element has been defined in [17]. Then, the time integration according to eqs. (2-13) and (2-14) starts, where the displacement field of $\boldsymbol{d}_i$ is given from either the initial conditions or the previous time-step. The local displacement jump $\boldsymbol{\delta}$ is then calculated with eqs. (6-1), (2-19) and (2-20). Subsequently, the traction vector $\boldsymbol{\tau}$ cosisting of normal and shear tractions caused by the adhesive is calculated. For these tractions, the explicit element checks firstly, if the adhesive can bear the load according to eq. (5-14), and secondly, whether a delamination initiates according to eq. (6-7). If a delamination initiates, the mixed-mode failure criterion is adapted to eq. (6-18) for the next time-steps. If the mixed-mode failure criterion is fulfilled in any case, the tractions $\boldsymbol{\tau}$ are set to zero except for compressive loadings according to eq. (5-18). In the following, the spatial integration of eq. (6-3) is performed and added to the internal force vector. Then the global displacement field $\boldsymbol{d}_{i+1}$ is updated for the next time-step according to eqs. (2-13) and (2-14).

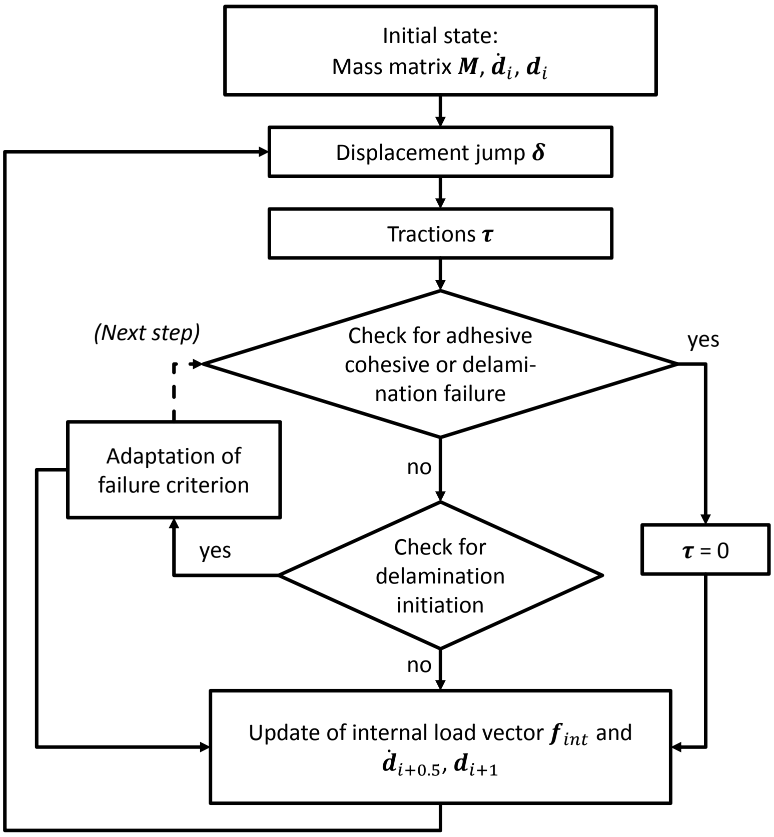

Figure 6-4 Solution process of the boundary value problem with the new CZ approach.

6.2 Numerical evaluation

6.2.1 Numerical model

In this section, the new cohesive element is evaluated in a 2D FE study of a SLJ. The commercial FE solver Abaqus/Explicit [25] is used. The cohesive element formulated in section 6.1 has been implemented as an explicit user element (VUEL) in Abaqus/Explicit. The geometry of the SLJ is shown in Fig. 6-5.

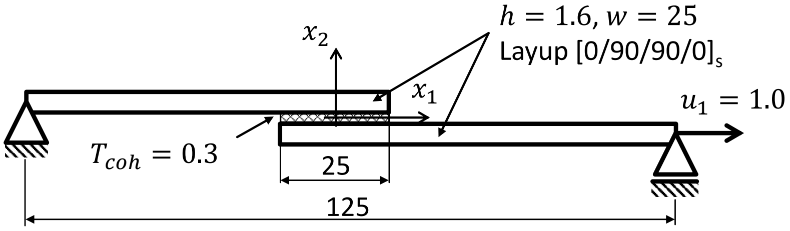

Figure 6-5 Geometry of the numerical model [111].

The SLJ has been modelled in two ways for comparison. The first model uses the conventional CZM of the literature [117–119]. Every ply of the adherend is modelled by reduced integration plane stress elements (CPS4R) with cohesive elements (COH2D4) in between each ply to model the delamination interfaces. The plane stress assumption has been chosen here, since the model is compared to a beam modelling of the adherend which implies a plane stress assumption as well. The adhesive is modelled with one layer of cohesive elements (COH2D4) over the complete bondline thickness. The mesh size is set to $0.1mm$ in the overlap and $0.5mm$ outside the overlap. A close-up of the overlap edge is shown in Fig. 6-6. This model is denoted as “detailed model” in the following.

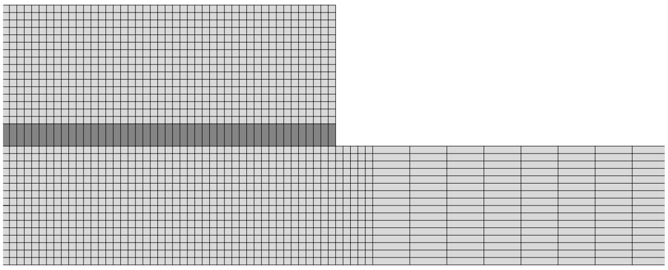

Figure 6-6 Mesh of the detailed model at the right edge of the overlap [111].

The second model is denoted the “reduced model”. It uses linear beam elements (B21) for the representation of the adherends. The adhesive is modelled by the new cohesive element according to section 6.1 representing the adhesive’s cohesive behaviour and the delamination failure. The mesh size in the overlap is set to $0.1mm$, i.e. equal to the detailed model (see Fig. 6-7).

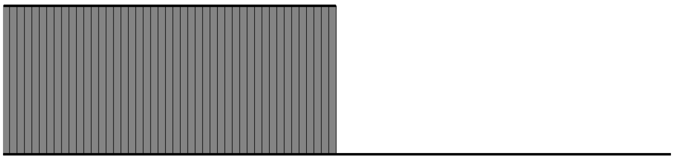

Figure 6-7 Mesh of the reduced model at the right edge of the overlap [111].

The material of a ply is defined orthotropic linear elastic with a Young's modulus of $E_{11} = 160{,}000 MPa$, $E_{22} = E_{33} = 10{,}000 MPa$, $G_{12} = G_{13} = 5{,}000 MPa$, $G_{23} = 3{,}500 MPa$ and a Poisson ratio of $\nu_{12} = \nu_{13} = 0.32$ and $\nu_{23} = 0.43$. The layup of the adherend is defined to be $[0/90/90/0]_s$ with an equal thickness of each ply, which gives a total thickness of $h_{lam} = 1.6mm$. Two variations of delamination properties are used in the numerical study according to table 6-1. In the detailed model, the values are used for the definition of a triangular mixed-mode cohesive law according to [36]. The initial stiffness of the triangular cohesive law is set to $10^6 N/mm^3$ [29].

Table 6-1 Delamination properties “DelStrong” and “DelWeak” [111].

	σ_{22}^0 $[MPa]$	$G_{Ic,del}$ $\left[\frac{mJ}{mm^2}\right]$	σ_{12}^0 $[MPa]$	$G_{IIc,del}$ $\left[\frac{mJ}{mm^2}\right]$
“DelStrong”	60	0.3	90	0.8
“DelWeak”	20	0.1	30	0.2

Typical quasi-static material properties for a toughened epoxy adhesive like it is used in the automotive industry are taken which can be seen in Fig. 6-8 [68]. The adhesive's normal and shear behaviour has been modelled as described in section 6.1 by eq. (6-4). The section and material properties of the beam elements in the reduced model were defined to have equal membrane and bending stiffness like the adherends in the detailed model. Additionally, the transverse shear stiffness is

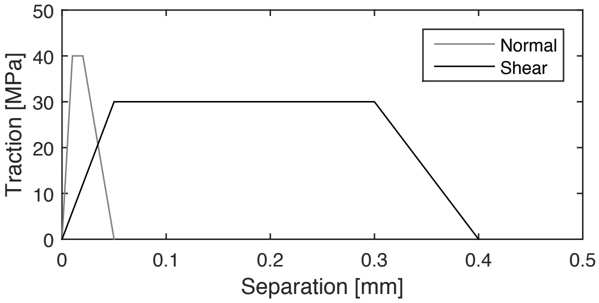

Figure 6-8 Cohesive law of the adhesive in normal and shear direction [111].

set to $\kappa_T GA = 142000N$, which approximates the transverse shear stiffness of the adherend in the detailed model sufficiently.

6.2.2 Results and discussion

The results of the SLJ simulation are shown in Fig. 6-9 for the delamination properties “DelStrong”. The detailed model as well as the reduced model fail by cohesive failure in the adhesive. The reduced model with the VUEL is in good agreement with the detailed model in terms of a force-displacement curve. The joint stiffness and strength correlate well.

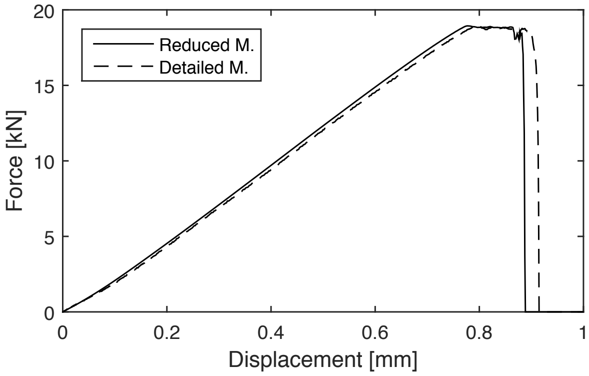

Figure 6-9 Force-displacement curve using the “DelStrong” delamination properties [111].

For the “DelWeak” delamination properties, the reduced model and the detailed model show a delamination failure. In the detailed model, the failure is located at the edge of the bonded region (see Fig. 6-10) which is the same location where the VUEL predicts the delamination initiation.

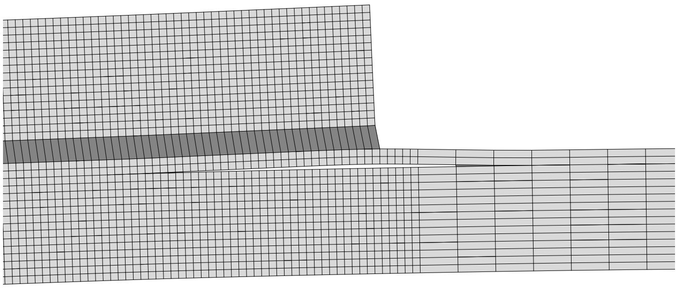

Figure 6-10 Location of delamination initiation in the detailed model [111].

The force-displacement curve is shown in Fig. 6-11. Again, the initial joint stiffness is well in agreement between both models. In terms of the maximum force, the reduced model gives a large underestimation with a maximum force of $4.92kN$, which is 43% of the maximum force of the detailed model of $11.57kN$. However, it has been found that the conventional CZM like in the detailed model is not necessarily conservative compared to experimental results. The over-prediction was up to 25% in [119]. Still, the new element gives a quite conservative approximation of the joint strength. In the following, the detailed and reduced model will be compared in terms of the through thickness stress computation, the convergence behaviour and the numerical efficiency in order to work out more clearly the value of the new cohesive element.

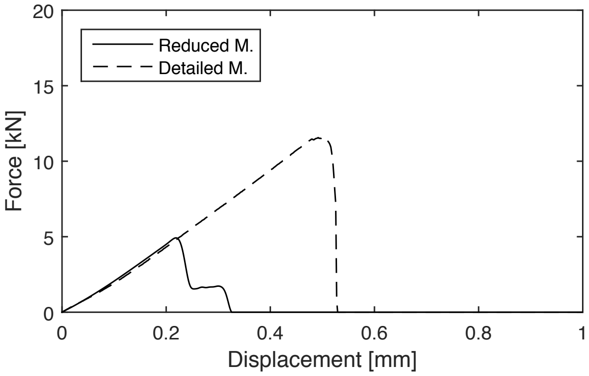

Figure 6-11 Force-displacement curve using the "DelWeak" delamination properties [111].

The through thickness stress distribution calculated by the VUEL and measured in the detailed model are compared at a distance of $0.5mm$ away from the overlap edge. The stresses could not be evaluated directly at the overlap edge since numerical singularities occured in the detailed model as shown in Fig. 6-12. The stress distribution was evaluated at a joint load of $3.21kN$, because this is the load level where the first damage occurred to one of the delamination elements in the detailed model.

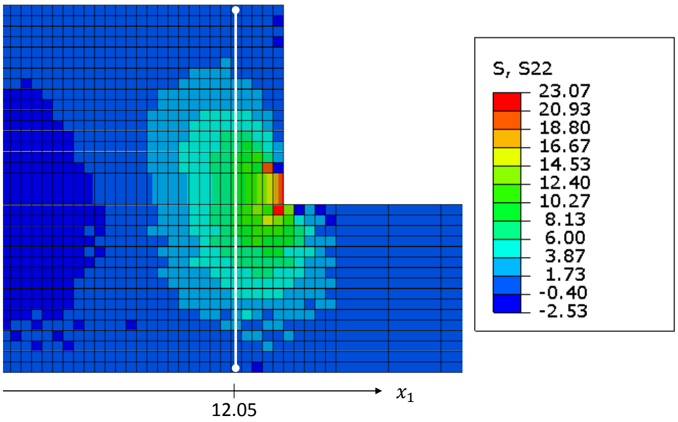

Figure 6-12 Tensile stresses in x_2-direction at the overlap edge at a load level of $3.21kN$ and position of the through thickness stress evaluation (white line) [111].

It can be seen in Fig. 6-13 that the shear stress in the adhesive (from thickness $-0.15mm$ to $+0.15mm$) is well in agreement between the VUEL calculation and the detailed model. The through thickness stress in the adherends are qualitatively approximated by the analytical predictions in the VUEL. At the top and bottom side of the joint, the shear stresses vanish, which is in accordance with the detailed model and the mechanical balance of forces.

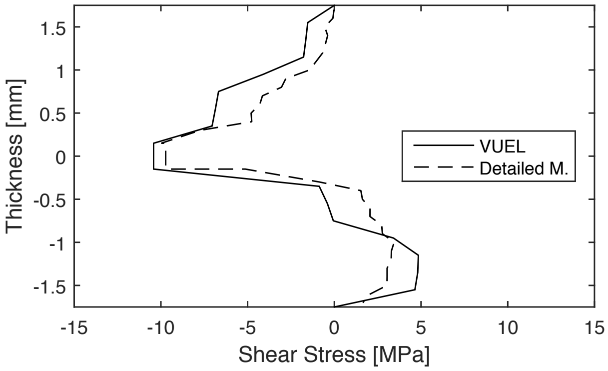

Figure 6-13 Comparison of the through thickness shear stresses for a joint load of $3.21kN$ [111].

The through thickness tensile stresses are shown in Fig. 6-14. Here, the tensile stresses of the adhesive bondline (from thickness $-0.15mm$ to $+0.15mm$) differ from the stresses in the detailed model. The deviations can be due to the fact that the detailed model has a compliance in thickness direction while the analytical approach assumes a transverse rigidity of the beams. Towards the top and bottom side of the joint the tensile stresses vanish, which is again in accordance with the detailed model and the mechanical balance of forces.

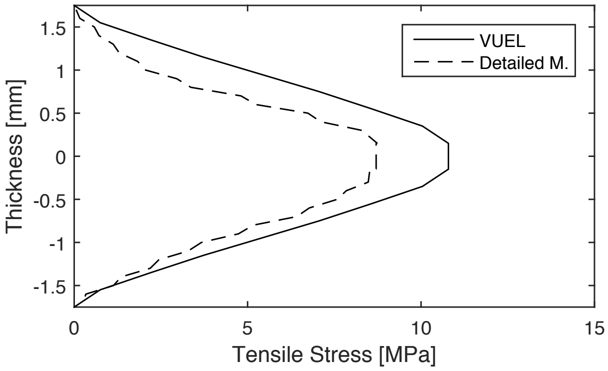

Figure 6-14 Comparison of the through thickness tensile stresses for a joint load of $3.21kN$ [111].

In the reduced model, delamination initiation according to eq. (6-7) was detected at a load level of $3.57kN$, which approximated the delamination initiation in the detailed model by 11%. The error can be traced back on the one hand to the singularities in the detailed model and on the other hand to the error in the through thickness tensile stress computation of the new cohesive element. The large error in the prediction of the joint strength when delamination occurs must be, therefore, due to the dynamic delamination propagation process in the adherend.

Now, the convergence behaviour of both models is investigated. Both models are discretised by a mesh-size from $0.02mm$ to $1mm$. The convergence of the reduced model is shown in Fig. 6-15. The joint strength has been normalised using the joint strength value at a mesh size of $0.1mm$. A good convergence behaviour is found for the reduced model using the new cohesive element. For a mesh size of at least $0.1mm$, i.e. 250 elements in the overlap, the results do not improve more than 2.3% while a bigger mesh size increases the joint strength. Fig. 6-16 shows that the detailed model shows convergence difficulties. The joint strength is again normalised by the joint strength at a mesh size of $0.1mm$. In the detailed model, it can vary between $+9.1\%$ and -11.1%. This shows that the reduced model improves the convergence behaviour of the numerical model.

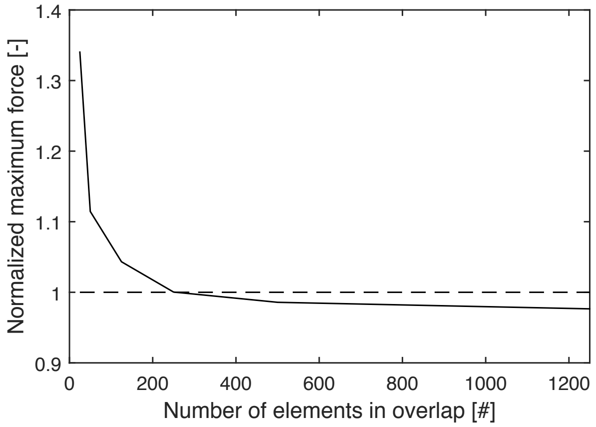

Figure 6-15 Convergence study of the reduced model [111].

The computational efficiency of the VUEL is estimated in terms of the critical time-step and the degrees of freedom (DOFs) needed in the model. The critical time-step for the detailed model is given by the smallest critical time-step in either the outer ply in the adherend, the delamination interface or the adhesive bondline. Table 6-2 shows the approximate critical time-steps according to eq. (2-15). For the element length l_{el}, the length in thickness direction has been used to avoid effects from the mesh size parallel to the bondline. For the interface elements representing delamination, an interface stiffness of $K = 10^6 N/mm^3$ has been chosen [29]. The minimum critical time-step for the detailed model is then $4.0E^{-5}ms$ due to the modelling of these interface layers. For the presented VUEL, the critical time-

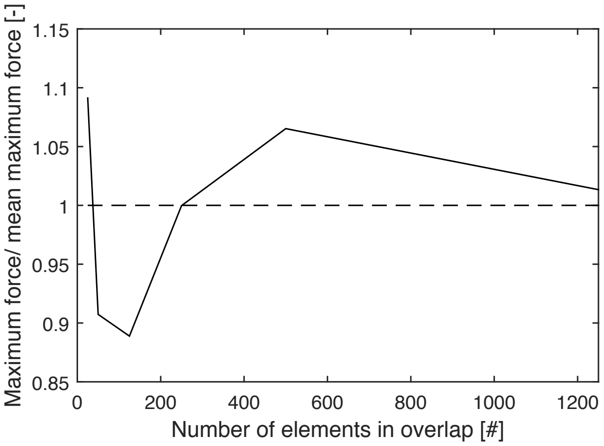

Figure 6-16 Convergence study of the detailed model [111].

Table 6-2 Estimation of the minimum critical time-step in thickness direction [111].

	l_{el} $[mm]$	E $[MPa]$	ρ $[g/mm^3]$	Δt_{crit} [ms]
Single Layer	0.2	10,000	$1.6E^{-3}$	$8.0E^{-5}$
Delamination	1	10^6	$1.6E^{-3}$	$4.0E^{-5}$
Bondline	0.3	1,200	$1.6E^{-3}$	$3.5E^{-4}$

step is defined by the critical time-step of the adhesive bondline since the plies of the laminate and delamination interfaces are substituted from the model. This is $3.5E^{-4}ms$ for the reduced model. This means an increase of a factor of 8.75 in the reduced model compared to the detailed model.

The DOFs saved by the VUEL depend on the mesh size and the overlap length of the joint. The following consideration normalises the savings in DOFs by only counting DOFs in thickness direction for the 2D case. The reduced model uses 3 DOFs for a beam node and 3 DOFs for the VUEL element for each side of the adherend. This gives in total 12 DOFs in thickness direction for the reduced model. The detailed model has $4n$ DOFs for n plies and $4(n-1)$ DOFs for the delamination interfaces modelled on each side of the bondline plus 4 DOFs for the adhesive modelled. This gives in total $16n-4$ DOFs needed in thickness direction, where n is number of plies modelled. For $n = 8$ layers in the layup, 128 DOFs are needed in the detailed model compared to 12 DOFs in the reduced model. On the other hand, the analytical calculations within the presented VUEL increase the computational time. The savings due to the increase of the critical time-step and the reduction of DOFs are much more significant.

The value of the new CZ model including delamination failure is the adequate prediction of delamination initiation, the good convergence behaviour and a large reduction of computational cost. However, delamination propagation leads to a large under-prediction of the joint strength. Therefore, the mixed-mode fracture criterion according to eq. (6-18) is adapted. It can be visually deduced from Fig. 6-10, that after delamination initiation the compliance in thickness direction increases significantly while the compliance in load direction is less affected by the delamination crack because it is still possible that shear loads can be transferred over the overlap region. The mixed-mode fracture criterion is, therefore, adapted to

$$\frac{J_N}{J_N^* + J_{Ic,del}} + \frac{J_S}{J_S^0} = 1. \tag{6-19}$$

This means, that the fracture energy in shear direction is not changed after delamination initiation providing a higher capacity for shear deformation. The results of the numerical model with the "DelWeak" properties for delamination can be seen in Fig. 6-17. The maximum force of the reduced model is then $7.38kN$, which is 64% of the maximum force of the detailed model and improves the accuracy of the VUEL when delamination failure occurs.

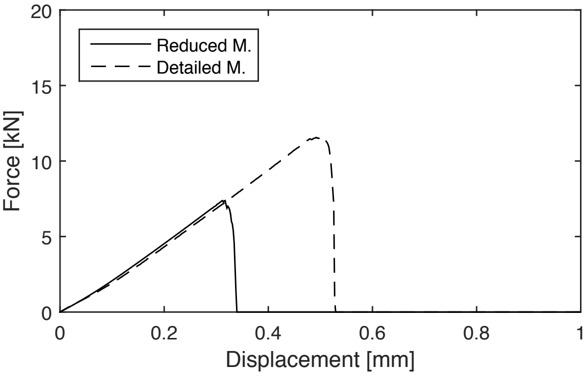

Figure 6-17 Force-displacement curve for the "DelWeak" delamination properties with the mixed-mode fracture criterion of eq. (6-19) [111].

6.3 Summary of the Chapter

A new explicit cohesive element combining cohesive failure in the adhesive and delamination failure of bonded joints with laminated adherends has been formulated and implemented. For a SLJ geometry, a numerical study was carried out to validate the newly proposed cohesive element with a conventional CZM. The results have shown, that the model with the new cohesive element is well in agreement with the conventional model when the bonded joint fails due to cohesive failure in the adhesive.

In the case of delamination failure, delamination initiation is well approximated. The joint strength is however largely underestimated by the new cohesive element compared to the conventional modelling. Other works have shown, that the conventional approach is not necessarily conservative compared to experimental results. Additionally, convergence difficulties have been observed in this study. The reason for the underestimation comes from the modelling of the crack propagation in the delamination interface. With an adaptation of the mixed-mode failure criterion after delamination initiation, the discrepancy in the joint strength predicted by the new cohesive element could be reduced.

With the new modelling approach, the convergence behaviour is improved and the computational performance is significantly increased by an increase in the critical time-step and a decrease of DOFs for the joint model. Due to its computational efficiency, the presented explicit cohesive element provides an opportunity to predict cohesive failure of the adhesive and delamination failure in bonded joints with laminated adherends in full scale crash simulations. Because of the local formulation, the modelling technique can be applied to any geometry of a bonded joint.

7 Conclusion and outlook

Methods for the characterisation of an adhesive for CZM and for the simulation of cohesive and delamination failure in composite bonded joints have been presented in this thesis. A step beyond the state-of-the-art has been made, but many challenges remain in the field of bonded joining with fibre reinforced adherends for crash applications. Some of them are outlined in the following.

7.1 Characterisation of the adhesive

The characterisation of the adhesive has been done for quasi-static, intermediate-rate and high-rate loading conditions. The quasi-static and intermediate-rate experiments were performed on an electromechanical testing machine and the high-rate experiments were performed on a tensile split-Hopkinson bar set-up. Through the tests, the adhesive bondline could be characterised for a wide range of loading rates. But also other findings came up by the evaluation of the experiments.

It was found out in the quasi-static tests, that the stress-deformation relation of a butt joint test approximates the mode I traction-separation relation of DCB test in terms of the bondline strength and fracture energy. For the lap shear test and the ENF test, the correlation between the stress-deformation curve and the traction-separation relation was not as good as in mode I. The reason can be the high sensitivity of the results on the determination of the crack front in the ENF tests on the one hand. On the other hand, the length of the ENF specimen was short and could cause the fracture process zone to grow under the loading point. Increasing the ENF specimen size could reduce the error. On the other hand the lap shear test does not allow a pure shear loading at the crack front, because peel stresses at the edge of the overlap are present. For better correlation of lap shear test and ENF test results an adaptation of the experiments and further research on the data reduction will be necessary.

The mixed-mode quasi-static behaviour has been tested by a scarf joint. It was found, that the fracture energy correlated with a linear variation of the fracture energy of the pure mode experiments. Joint strength and stiffness were decreased compared to the pure mode experiments. In this thesis, one type of scarf joint and therefore one mixed-mode ratio was tested. To get deeper insight in the mixed-mode behaviour of an adhesive bondline, several inclination angles should be tested.

Intermediate-rate experiments in normal mode showed a positive rate effect on the strength of the bondline. A statistically significant quantitative prediction of the rate-effect on the stiffness and energy absorbed could not be made due to large standard deviations in the experimental results. To achieve better results for intermediate-rate loading, special servo-hydraulic testing machines are assumed to provide better results. Moreover, it would be desired to tests at several loading rates as well as in shear mode direction.

It was found in this thesis that the measurement of the bondline deformations by digital image correlation significantly improves the accuracy in high-rate tests with a tensile split-Hopkinson bar set-up compared to a classical evaluation of deformations by the strain gauge signals. Therefore, good results were found for butt joint and lap shear tests. High-rate test results for mixed-mode conditions have not been performed in this work. Additionally, the prediction of the fracture energy of the bondline should be compared to fracture mechanics tests, which are currently available for intermediate-rate loading but rare for high-rate loading in the literature.

7.2 Simulation of cohesive failure in composite bonded joints

The results of the adhesive characterisation have been used to calibrate a cohesive law. A rate-dependent mixed-mode cohesive law based on a mixed-mode trapezoidal law available in the literature has been therefore implemented. The pure mode stiffness and ultimate traction has been calibrated by the butt joint and lap shear test results for quasi-static and high-rate loading. The fracture energy in pure mode has been taken from the quasi-static DCB and ENF test results and extrapolated for high-rate loading. The cohesive zone approach was successfully applied to the quasi-static and high-rate simulation of a single lap joint in 2D and a T-joint subcomponent in 3D. This showed that the modelling approach is suitable for efficient use in full scale crash simulations.

By validation of the mixed-mode behaviour with the combined loading tests, it was found, that the cohesive law overestimated the stiffness and strength of the bondline. By an adaptation of the mixed-mode interaction criterion, the error in the mixed-mode ultimate tractions could be compensated. Moreover, the non-linear behaviour of the bondline was not adequately represented by the cohesive law. If the ratio of adherend stiffness to bondline stiffness is small and the overlap length is sufficiently long, the influence of the cohesive law shape is small. For other cases, an improved non-linear mixed-mode formulation would increase the accuracy of the cohesive law. An example of such a cohesive law has been published by Anyfantis and Tsouvalis [122].

The representation of intermediate-rate loading has been realised using a quadratic logarithmic interpolation of the tractions. The interpolation has been defined by the butt joint experiments in normal mode. Further experiments for the interpolation strategy e.g. at several loading rates and for shear mode and mixed-mode loading would be desired to refine the calibration of the cohesive law.

The simulation of cohesive failure in bonded joints in 2D and 3D was well correlated with the experimental findings by single lap joints and a T-joint subcomponent for quasi-static loading conditions. For the high-rate experiments, the simulation differed from the experimental findings. The single lap joint experiments were overpredicted by the simulation. Voids in the bonding area were found on the fracture surfaces that could be responsible for the error. The simulation of a T-joint substructure lead to a conservative approximation of the experimental results. The influence of the spew fillet, inertia of the test set-up and the boundary conditions were found to strongly influence the simulation results. Modified experiments with less void content and clearer specifications are therefore necessary to better validate the cohesive failure at high-rate loading.

7.3 Simulation of delamination failure in composite bonded joints

A new cohesive zone approach combining cohesive failure of the adhesive and delamination failure has been developed in this thesis. The approach makes it possible to simulate delamination failure in bonded joints with high numerically efficiency. It can be applied to full scale crash simulations and standardised tests provide sufficient input data for the calibration of the new cohesive zone approach. The convergence of the new approach improves the convergence behaviour of the conventional approach. It has been found, that the accuracy of the new cohesive zone approach is high when cohesive failure in the adhesive occurs. When delamination failure occurs, the delamination initiation is well approximated. Inaccuracies have been found in the prediction of delamination propagation and therefore in the prediction of the joint strength.

The new cohesive zone approach has been implemented for the 2D case and validated numerically. For an application in the industrial environment, it is necessary to further develop the approach for 3D shell structures. In the new cohesive zone approach, a transverse rigidity of the adherends and a linear variation of strains over the adherend thickness has been assumed. The accuracy of the new cohesive zone approach could be improved by accounting for the adherend compliance in thickness direction and using shear flexible theories for the adherend through thickness stress calculation. Additionally, the new approach has not been validated by experiments in this thesis. Since the numerical reference model showed significant drawbacks, experiments for the validation of the new cohesive zone approach would be desired for future works.

Bibliography

[1] EU, "Emission performance standards for new passenger cars as part of the Community's integrated approach to reduce CO 2 emissions from light-duty vehicles: Regulation (EC) No 443/2009."

[2] S. Keller, P. Collopy, and P. Componation, "What is wrong with space system cost models? A survey and assessment of cost estimating approaches," *Acta Astronautica*, vol. 93, pp. 345–351, 2014.

[3] A. Jacob, "Carbon fibre and cars – 2013 in review," *Reinforced Plastics*, vol. 58, no. 1, pp. 18–19, 2014.

[4] G. Marsh, "Greater role for composites in wind energy," *Reinforced Plastics*, vol. 58, no. 1, pp. 20–24, 2014.

[5] B. Jahn and D. Karl. (2012) Composites-Marktbericht 2012: Der globale CFK-Markt. [Online]. Available: http://www.carbon-composites.eu/sites/carbon-composites.eu/files/anhaenge/12/11/06/composites_marktbericht_2012_-_deutsch.pdf

[6] M. standard, "Light Fixed- and Rotary-Wing Aircraft Crash Resistance," Washington, 1988.

[7] L. F. M. da Silva and R. D. S. G. Campilho, Eds., *Advances in Numerical Modeling of Adhesive Joints*, ser. SpringerBriefs in Applied Sciences and Technology. Berlin, Heidelberg: Springer Berlin Heidelberg, 2012.

[8] A. J. Kinloch, *Adhesion and Adhesives: Science and Technology.* Dordrecht: Springer Netherlands, 1987.

[9] R. D. Adams, J. Comyn, and W. C. Wake, *Structural adhesive joints in engineering*, 2nd ed. London and New York: Chapman & Hall, 1997.

[10] R. D. Adams, *Adhesive bonding: Science, technology and applications.* Boca Raton, FL and Cambridge: CRC Press and Woodhead Pub., 2005.

[11] L. F. M. da Silva, A. Öchsner, and R. D. Adams, *Handbook of adhesion technology*, ser. Springer reference. Berlin and London: Springer, 2011.

[12] R. D. S. G. Campilho, M. D. Banea, J. A. B. P. Neto, and L. F. M. da Silva, "Modelling adhesive joints with cohesive zone models: effect of the cohesive law shape of the adhesive layer," *International Journal of Adhesion and Adhesives*, vol. 44, pp. 48–56, 2013.

[13] M. S. Kafkalidis and M. D. Thouless, "The effects of geometry and material properties on the fracture of single lap-shear joints," *International Journal of Solids and Structures*, vol. 39, no. 17, pp. 4367–4383, 2002.

[14] L. F. da Silva, Rodrigues, T. N. S. S., Figueiredo, M. A. V., de Moura, M. F. S. F., and Chousal, J. A. G., “Effect of Adhesive Type and Thickness on the Lap Shear Strength,” *The Journal of Adhesion*, vol. 82, no. 11, pp. 1091–1115, 2006.

[15] L. F. da Silva, das Neves, Paulo J.C., R. D. Adams, and J. K. Spelt, “Analytical models of adhesively bonded joints—Part I: Literature survey,” *International Journal of Adhesion and Adhesives*, vol. 29, no. 3, pp. 319–330, 2009.

[16] R. A. Sauer, “A survey of computational models for adhesion,” *The Journal of Adhesion*, vol. 92, no. 2, pp. 81–120, 2015.

[17] T. Carlberger, K. S. Alfredsson, and U. Stigh, “Explicit FE-formulation of interphase elements for adhesive joints,” *International Journal for Computational Methods in Engineering Science and Mechanics*, vol. 9, no. 5, pp. 288–299, 2008.

[18] A. Puck, *Festigkeitsanalyse von Faser-Matrix-Laminaten: Modelle für die Praxis.* München and Wien: Hanser, 1996.

[19] H. Schürmann, *Konstruieren mit Faser-Kunststoff-Verbunden*, ser. VDI. Berlin and Heidelberg and New York: Springer, 2005.

[20] J. C. Brewer and P. A. Lagace, “Quadratic Stress Criterion for Initiation of Delamination,” *Journal of Composite Materials*, vol. 22, no. 12, pp. 1141–1155, 1988.

[21] Y. Mi, M. A. Crisfield, Davies, G. A. O., and H. B. Hellweg, “Progressive Delamination Using Interface Elements,” *Journal of Composite Materials*, vol. 32, no. 14, pp. 1246–1272, 1998.

[22] M. L. Benzeggagh and M. Kenane, “Measurement of mixed-mode delamination fracture toughness of unidirectional glass/epoxy composites with mixed-mode bending apparatus,” *Composites Science and Technology*, vol. 56, no. 4, pp. 439–449, 1996.

[23] K.-J. Bathe, *Finite Element Procedures.* Upper Saddle River / New Jersey / USA: Prentice-Hall, 1996.

[24] O. C. Zienkiewicz, R. L. Taylor, and J. Z. Zhu, *The finite element method*, 6th ed. Oxford: Elsevier Butterworth-Heinemann, 2005.

[25] D. Hibbitt, B. Karlsson, and E. P. Sorensen, “Abaqus,” Providence, Rhode Island, USA, 2013.

[26] G. I. Barenblatt, “The mathematical theory of equilibrium cracks in brittle fracture,” *Advances in applied mechanics*, vol. 7, no. 1, pp. 55–129, 1962.

[27] D. S. Dugdale, “Yielding of steel sheets containing slits,” *Journal of the Mechanics and Physics of Solids*, vol. 8, no. 2, pp. 100–104, 1960.

[28] A. Turon, P. P. Camanho, J. Costa, and C. G. Dávila, “A damage model for the simulation of delamination in advanced composites under variable-mode loading,” *Mechanics of Materials*, vol. 38, no. 11, pp. 1072–1089, 2006.

[29] P. P. Camanho, C. G. Dávila, and M. F. de Moura, “Numerical simulation of mixed-mode progressive delamination in composite materials,” *Journal of Composite Materials*, vol. 37, no. 16, pp. 1415–1438, 2003.

[30] A. Hillerborg, M. Modéer, and P.-E. Petersson, “Analysis of crack formation and crack growth in concrete by means of fracture mechanics and finite elements,” *Cement and Concrete Research*, vol. 6, no. 6, pp. 773–781, 1976.

[31] A. Needleman, “A Continuum Model for Void Nucleation by Inclusion Debonding,” *Journal of Applied Mechanics*, vol. 54, no. 3, p. 525, 1987.

[32] V. Tvergaard and J. W. Hutchinson, “The relation between crack growth resistance and fracture process parameters in elastic-plastic solids,” *Journal of the Mechanics and Physics of Solids*, vol. 40, no. 6, pp. 1377–1397, 1992.

[33] A. Needleman, “Micromechanical modelling of interfacial decohesion,” *Ultramicroscopy*, vol. 40, no. 3, pp. 203–214, 1992.

[34] M. Ortiz and A. Pandolfi, “Finite-deformation irreversible cohesive elements for three-dimensional crack-propagation analysis,” *International Journal for Numerical Methods in Engineering*, vol. 1999, no. 44, pp. 1267–1282, 1999.

[35] O. Allix and A. Corigliano, “Modeling and simulation of crack propagation in mixed-modes interlaminar fracture specimens,” *International Journal of Fracture*, vol. 77, no. 2, pp. 111–140, 1996.

[36] S. T. Pinho, L. Iannucci, and P. Robinson, “Formulation and implementation of decohesion elements in an explicit finite element code,” *Composites Part A: Applied Science and Manufacturing*, vol. 37, no. 5, pp. 778–789, 2006.

[37] G. Alfano, “On the influence of the shape of the interface law on the application of cohesive-zone models,” *Composites Science and Technology*, vol. 66, no. 6, pp. 723–730, 2006.

[38] Q. D. Yang, M. D. Thouless, and S. M. Ward, “Numerical simulations of adhesively-bonded beams failing with extensive plastic deformation,” *Journal of the Mechanics and Physics of Solids*, vol. 47, no. 6, pp. 1337–1353, 1999.

[39] Q. D. Yang, M. D. Thouless, and S. Ward, "Elastic-plastic mode-II fracture of adhesive joints," *International Journal of Solids and Structures*, vol. 38, no. 18, pp. 3251–3262, 2001.

[40] Q. D. Yang and M. D. Thouless, "Mixed-mode fracture analyses of plastically-deforming adhesive joints," *International Journal of Fracture*, vol. 110, no. 2, pp. 175–187, 2001.

[41] R. D. S. G. Campilho, M. D. Banea, J. A. B. P. Neto, and L. F. M. da Silva, "Modelling of single-lap joints using cohesive zone models: Effect of the cohesive parameters on the output of the simulations," *The Journal of Adhesion*, vol. 88, no. 4-6, pp. 513–533, 2012.

[42] R. D. S. G. Campilho, de Moura, M. F. S. F., and J. J. M. S. Domingues, "Using a cohesive damage model to predict the tensile behaviour of CFRP single-strap repairs," *International Journal of Solids and Structures*, vol. 45, no. 5, pp. 1497–1512, 2008.

[43] C. Su, Y. Wei, and L. Anand, "An elastic–plastic interface constitutive model: application to adhesive joints," *International Journal of Plasticity*, vol. 20, no. 12, pp. 2063–2081, 2004.

[44] S. H. Marzi, O. Hesebeck, M. Brede, and F. Kleiner, "A rate-dependent, elasto-plastic cohesive zone mixed-mode model for crash analysis of adhesively bonded joints," in *7th European LS-DYNA conference*, 2009.

[45] A. Matzenmiller, S. Gerlach, and M. Fiolka, "A critical analysis of interface constitutive models for the simulation of delamination in composites and failure of adhesive bonds," *Journal of Mechanics of Materials and Structures*, vol. 5, no. 2, pp. 185–211, 2010.

[46] M. Musto and G. Alfano, "A novel rate-dependent cohesive-zone model combining damage and visco-elasticity," *Computers & Structures*, vol. 118, pp. 126–133, 2013.

[47] A. Rauh, *Prognose des Versagensverhaltens von CFK-Klebverbindungen unter Crashbelastung*, 1st ed. München: Dr. Hut, 2015.

[48] A. Rauh, R. Hinterhölzl, and K. Drechsler, "Application of the time-temperature superposition principle to the mechanical characterization of elastomeric adhesives for crash simulation purposes," *The European Physical Journal Special Topics*, vol. 206, no. 1, pp. 15–24, 2012.

[49] L. F. M. da Silva, *Testing adhesive joints: Best practices.* Weinheim: Wiley-VCH, 2012.

[50] R. D. Adams and J. Coppendale, "The stress-strain behaviour of axially-loaded butt joints," *The Journal of Adhesion*, vol. 10, no. 1, pp. 49–62, 1979.

[51] T. Andersson and U. Stigh, "The stress–elongation relation for an adhesive layer loaded in peel using equilibrium of energetic forces," *International Journal of Solids and Structures*, vol. 41, no. 2, pp. 413–434, 2004.

[52] R. D. Adams, J. Coppendale, and N. A. Peppiatt, "Stress analysis of axisymmetric butt joints loaded in torsion and tension," *The Journal of Strain Analysis for Engineering Design*, vol. 13, no. 1, pp. 1–10, 1978.

[53] M. Brede, O. Hesebeck, S. Marzi, M. May, and H. Voß, "Berechnung nach dem kohäsivzonenmodell (teil 2)," *Adhäsion KLEBEN & DICHTEN*, vol. 57, no. 9, pp. 40–45, 2013.

[54] B. F. Sørensen, "Cohesive law and notch sensitivity of adhesive joints," *Acta Materialia*, vol. 50, no. 5, pp. 1053–1061, 2002.

[55] U. Stigh, K. S. Alfredsson, T. Andersson, A. Biel, T. Carlberger, and K. Salomonsson, "Some aspects of cohesive models and modelling with special application to strength of adhesive layers," *International Journal of Fracture*, vol. 165, no. 2, pp. 149–162, 2010.

[56] K. Leffler, K. S. Alfredsson, and U. Stigh, "Shear behaviour of adhesive layers," *International Journal of Solids and Structures*, vol. 44, no. 2, pp. 530–545, 2007.

[57] C. Sato and K. Ikegami, "Strength of adhesively-bonded butt joints of tubes subjected to combined high-rate loads," *The Journal of Adhesion*, vol. 70, no. 1-2, pp. 57–73, 1999.

[58] R. Mahnken and M. Schlimmer, "Simulation of strength difference in elasto-plasticity for adhesive materials," *International Journal for Numerical Methods in Engineering*, vol. 63, no. 10, pp. 1461–1477, 2005.

[59] D. J. Pohlit, "Dynamic mixed-mode fracture of bonded composite joints for automotive crashworthiness," Ph.D. dissertation, Virginia Polytechnic State University, Blacksburg (Virginia), 2007.

[60] F. J. P. Chaves, "Fracture mechanics applied to the design of adhesively bonded joints," Ph.D. dissertation, Universidade do Porto, Porto, 2013.

[61] M. F. de Moura, J. P. M. Gonçalves, J. A. G. Chousal, and R. D. S. G. Campilho, "Cohesive and continuum mixed-mode damage models applied to the simulation of the mechanical behaviour of bonded joints," *International Journal of Adhesion and Adhesives*, vol. 28, no. 8, pp. 419–426, 2008.

[62] J. L. Högberg, B. F. Sørensen, and U. Stigh, “Constitutive behaviour of mixed mode loaded adhesive layer,” *International Journal of Solids and Structures*, vol. 44, no. 25-26, pp. 8335–8354, 2007.

[63] Zwick. (2016) Static and dynamic materials testing machines. Ulm, Germany. [Online]. Available: https://www.zwick.de

[64] S. Nemat-Nasser, Ed., *Introduction to High Strain Rate Testing: In: Mechanical testing and evaluation*, [11. ed.], 1. print ed., ser. ASM handbook. Materials Park, Ohio: ASM International, 2000, vol. / prepared under the direction of the ASM International Handbook Committee ; Vol. 8.

[65] H. Koerber, “Mechanical response of advanced composites under high strain rates,” Ph.D. dissertation, Universidade do Porto, Porto, 2010.

[66] G. T. I. Gray, Ed., *Classic split-Hopkinson pressure bar technique: In: Mechanical testing and evaluation*, [11. ed.], 1. print ed., ser. ASM handbook. Materials Park, Ohio: ASM International, 2000, vol. / prepared under the direction of the ASM International Handbook Committee ; Vol. 8.

[67] H. Kolsky, “An investigation of the mechanical properties of materials at very high rates of loading,” *Proceedings of the Physical Society. Section B*, vol. 62, no. 11, pp. 676–700, 1949.

[68] J. Neumayer, P. Kuhn, H. Koerber, and R. Hinterhölzl, “Experimental determination of the tensile and shear behaviour of adhesives under impact loading,” *The Journal of Adhesion*, vol. 92, no. 7-9, 2016.

[69] R. D. Adams and J. A. Harris, “A critical assessment of the block impact test for measuring the impact strength of adhesive bonds,” *International Journal of Adhesion and Adhesives*, vol. 16, no. 2, pp. 61–71, 1996.

[70] T. Yokoyama, “Experimental determination of impact tensile properties of adhesive butt joints with the split hopkinson bar,” *The Journal of Strain Analysis for Engineering Design*, vol. 38, no. 3, pp. 233–245, 2003.

[71] C. Keisler and J. L. Lataillade, “The effect of substrate roughness characteristics on wettability and on the mechanical properties of adhesive j oints loaded at high strain rates,” *Journal of Adhesion Science and Technology*, vol. 9, no. 4, pp. 395–411, 1995.

[72] V. Srivastava, A. Shukla, and V. Parameswaran, “Experimental evaluation of the dynamic shear strength of adhesive-bonded lap joints,” *Journal of testing and evaluation*, vol. 28, no. 6, pp. 438–442, 2000.

[73] M. Adamvalli and V. Parameswaran, “Dynamic strength of adhesive single lap joints at high temperature,” *International Journal of Adhesion and Ad-*

hesives, vol. 28, no. 6, pp. 321–327, 2008.

[74] X. Chen and Y. Li, “An experimental technique on the dynamic strength of adhesively bonded single lap joints,” *Journal of Adhesion Science and Technology*, vol. 24, no. 2, pp. 291–304, 2010.

[75] O. Sen, S. A. Tekalur, and C. Jilek, “The determination of dynamic strength of single lap joints using the split hopkinson pressure bar,” *International Journal of Adhesion and Adhesives*, vol. 31, no. 6, pp. 541–549, 2011.

[76] H. R. Sankar, M. Adamvalli, P. P. Kulkarni, and V. Parameswaran, “Dynamic strength of single lap joints with similar and dissimilar adherends,” *International Journal of Adhesion and Adhesives*, vol. 56, pp. 46–52, 2015.

[77] T. Yokoyama and H. Shimizu, “Evaluation of impact shear strength of adhesive joints with the split hopkinson bar,” *JSME International Journal Series A*, vol. 41, no. 4, pp. 503–509, 1998.

[78] K. Kihara, H. Isono, H. Yamabe, and T. Sugibayashi, “A study and evaluation of the shear strength of adhesive layers subjected to impact loads,” *International Journal of Adhesion and Adhesives*, vol. 23, no. 4, pp. 253–259, 2003.

[79] S. L. Raykhere, P. Kumar, R. K. Singh, and V. Parameswaran, “Dynamic shear strength of adhesive joints made of metallic and composite adherents,” *Materials & Design*, vol. 31, no. 4, pp. 2102–2109, 2010.

[80] M. A. Martínez, I. S. Chocron, J. Rodríguez, V. Sánchez–Gálvez, and L. A. Sastre, “Confined compression of elastic adhesives at high rates of strain,” *International Journal of Adhesion and Adhesives*, vol. 18, no. 6, pp. 375–383, 1998.

[81] P. Wang and L. R. Xu, “Convex interfacial joints with least stress singularities in dissimilar materials,” *Mechanics of Materials*, vol. 38, no. 11, pp. 1001–1011, 2006.

[82] T. Yokoyama and K. Nakai, “Determination of the impact tensile strength of structural adhesive butt joints with a modified split hopkinson pressure bar,” *International Journal of Adhesion and Adhesives*, vol. 56, pp. 13–23, 2015.

[83] H. Zhao, X. Duan, M. Ma, L. Lu, Z. Cai, P. C. Wang, and J. D. Fickes, “Dynamic characteristics of adhesive bonded high strength steel joints,” *Science and Technology of Welding and Joining*, vol. 15, no. 6, pp. 486–490, 2010.

[84] G. Challita, R. Othman, P. Casari, and K. Khalil, “Experimental investigation of the shear dynamic behavior of double-lap adhesively bonded joints on a wide range of strain rates,” *International Journal of Adhesion and Adhe-*

sives, vol. 31, no. 3, pp. 146–153, 2011.

[85] Y. Li and K. T. Ramesh, “An optical technique for measurement of material properties in the tension kolsky bar,” *International Journal of Impact Engineering*, vol. 34, no. 4, pp. 784–798, 2007.

[86] A. Gilat, T. E. Schmidt, and A. L. Walker, “Full field strain measurement in compression and tensile split hopkinson bar experiments,” *Experimental Mechanics*, vol. 49, no. 2, pp. 291–302, 2009.

[87] H. Koerber, J. Xavier, and P. P. Camanho, “High strain rate characterisation of unidirectional carbon-epoxy im7-8552 in transverse compression and in-plane shear using digital image correlation,” *Mechanics of Materials*, vol. 42, no. 11, pp. 1004–1019, 2010.

[88] G. C. Jacob, J. M. Starbuck, J. F. Fellers, S. Simunovic, and R. G. Boeman, “The effect of loading rate on the fracture toughness of fiber reinforced polymer composites,” *Journal of Applied Polymer Science*, vol. 96, no. 3, pp. 899–904, 2005.

[89] DOW. (2016) Betamate 1480 V203: Product Data. [Online]. Available: http://www.dow.com/en-us/markets-and-solutions/products/betamate/betamate1480v203

[90] J. R. Rice, “A path independent integral and the approximate analysis of strain concentration by notches and cracks,” *Journal of Applied Mechanics*, vol. 35, no. 2, p. 379, 1968.

[91] P. Olsson and U. Stigh, “On the determination of the constitutive properties of thin interphase layers ? an exact inverse solution,” *International Journal of Fracture*, vol. 41, no. 4, pp. R71–R76, 1989.

[92] Hexcel. (2016) Hexply 8552 Epoxy Matrix: Product Data. [Online]. Available: http://www.hexcel.com/Resources/DataSheets/Prepreg-Data-Sheets/8552_us.pdf

[93] J. W. Hutchinson and Z. Suo, “Mixed mode cracking in layered materials,” *Advances in applied mechanics*, vol. 29, no. 63, p. 191, 1992.

[94] L. Goglio, L. Peroni, M. Peroni, and M. Rossetto, “High strain-rate compression and tension behaviour of an epoxy bi-component adhesive,” *International Journal of Adhesion and Adhesives*, vol. 28, no. 7, pp. 329–339, 2008.

[95] T. Iwamoto, T. Nagai, and T. Sawa, “Experimental and computational investigations on strain rate sensitivity and deformation behavior of bulk materials made of epoxy resin structural adhesive,” *International Journal of Solids and Structures*, vol. 47, no. 2, pp. 175–185, 2010.

[96] T. Sugaya, T. Obuchi, and C. Sato, “Influences of loading rates on stress-strain relations of cured bulks of brittle and ductile adhesives,” *Journal of Solid Mechanics and Materials Engineering*, vol. 5, no. 12, pp. 921–928, 2011.

[97] S. Hayashida, T. Sugaya, S. Kuramoto, C. Sato, A. Mihara, and T. Onuma, “Impact strength of joints bonded with high-strength pressure-sensitive adhesive,” *International Journal of Adhesion and Adhesives*, vol. 56, pp. 61–72, 2015.

[98] F. Kadioglu and R. D. Adams, “Flexible adhesives for automotive application under impact loading,” *International Journal of Adhesion and Adhesives*, vol. 56, pp. 73–78, 2015.

[99] S. Marzi, A. Biel, and O. Hesebeck, “3d optical displacement measurements on dynamically loaded adhesively bonded t-peel specimens,” *International Journal of Adhesion and Adhesives*, vol. 56, pp. 41–45, 2015.

[100] R. Gerlach, C. Kettenbeil, and N. Petrinic, “A new split hopkinson tensile bar design,” *International Journal of Impact Engineering*, vol. 50, pp. 63–67, 2012.

[101] K. Marlett, “Hexcel 8552 IM7 Unidirectional Prepreg 190 gsm & 35%RC Qualification Material Property Data Report,” *CAM-RP-2009-015*, pp. 1–238, 2011.

[102] A. Makeev, G. Seon, Y. Nikishkov, and E. Lee, “Methods for assessment of interlaminar tensile strength of composite materials,” *Journal of Composite Materials*, vol. 49, no. 7, pp. 783–794, 2015.

[103] A. Makeev, G. Seon, and E. Lee, “Failure Predictions for Carbon/Epoxy Tape Laminates with Wavy Plies,” *Journal of Composite Materials*, vol. 44, no. 1, pp. 95–112, 2010.

[104] A. Makeev, “Interlaminar shear fatigue behavior of glass/epoxy and carbon/epoxy composites,” *Composites Science and Technology*, vol. 80, pp. 93–100, 2013.

[105] P. P. Camanho, P. Maimí, and C. G. Dávila, “Prediction of size effects in notched laminates using continuum damage mechanics,” *Composites Science and Technology*, vol. 67, no. 13, pp. 2715–2727, 2007.

[106] ASM. (2016) Aluminum 6061-T4; 6061-T451. [Online]. Available: http://asm.matweb.com/search/SpecificMaterial.asp?bassnum=MA6061T4

[107] P. P. Camanho and C. G. Dávila, “Mixed-mode decohesion finite elements for the simulation of delamination in composite materials,” *NASA/TM-2002-211737*, no. 1, 2002.

[108] R. M. Jones, *Mechanics of composite materials*, 2nd ed. Philadelphia, PA: Taylor & Francis, 1999.

[109] R. D. Adams, R. W. Atkins, J. A. Harris, and A. J. Kinloch, "Stress Analysis and Failure Properties of Carbon-Fibre-Reinforced-Plastic/Steel Double-Lap Joints," *The Journal of Adhesion*, vol. 20, no. 1, pp. 29–53, 1986.

[110] L. Grant, R. D. Adams, and L. F. da Silva, "Experimental and numerical analysis of single-lap joints for the automotive industry," *International Journal of Adhesion and Adhesives*, vol. 29, no. 4, pp. 405–413, 2009.

[111] J. Neumayer, H. Koerber, and R. Hinterhoelzl, "An explicit cohesive element combining cohesive failure of the adhesive and delamination failure in composite bonded joints," *Composite Structures*, vol. 146, pp. 75–83, 2016.

[112] N. Choupani, "Characterization of fracture in adhesively bonded double-lap joints," *International Journal of Adhesion and Adhesives*, vol. 29, no. 8, pp. 761–773, 2009.

[113] S. K. Panigrahi and B. Pradhan, "Through-the-width delamination damage propagation characteristics in single-lap laminated FRP composite joints," *International Journal of Adhesion and Adhesives*, vol. 29, no. 2, pp. 114–124, 2009.

[114] R. A. Esmaeel and F. Taheri, "Influence of adherend's delamination on the response of single lap and socket tubular adhesively bonded joints subjected to torsion," *Composite Structures*, vol. 93, no. 7, pp. 1765–1774, 2011.

[115] A. Needleman, "An analysis of tensile decohesion along an interface," *Journal of the Mechanics and Physics of Solids*, vol. 38, no. 3, pp. 289–324, 1990.

[116] G. Alfano and M. A. Crisfield, "Finite element interface models for the delamination analysis of laminated composites: mechanical and computational issues," *International Journal for Numerical Methods in Engineering*, vol. 50, no. 7, pp. 1701–1736, 2001.

[117] S. Li, M. D. Thouless, A. M. Waas, J. A. Schroeder, and P. D. Zavattieri, "Competing failure mechanisms in mixed-mode fracture of an adhesively bonded polymer-matrix composite," *International Journal of Adhesion and Adhesives*, vol. 26, no. 8, pp. 609–616, 2006.

[118] R. D. S. G. Campilho, de Moura, M. F. S. F., and J. J. M. S. Domingues, "Modelling single and double-lap repairs on composite materials," *Composites Science and Technology*, vol. 65, no. 13, pp. 1948–1958, 2005.

[119] J. A. B. P. Neto, R. D. S. G. Campilho, and L. F. da Silva, "Parametric study of adhesive joints with composites," *International Journal of Adhesion and*

Adhesives, vol. 37, pp. 96–101, 2012.

[120] C. G. Dávila, P. P. Camanho, and A. Turon, “Cohesive elements for shells,” *NASA/TP-2007-214869*, 2007.

[121] R. Parnes, *Solid mechanics in engineering.* Chichester and New York: Wiley, 2001.

[122] K. N. Anyfantis and N. G. Tsouvalis, “A novel traction–separation law for the prediction of the mixed mode response of ductile adhesive joints,” *International Journal of Solids and Structures*, vol. 49, no. 1, pp. 213–226, 2012.

A Publications

Journal papers

[P1] D. Heim, M. Hartmann, J. Neumayer, C. Klotz, Ö. Ahmet-Tsaus, S. Zaremba, and K. Drechsler, “Novel method for determination of critical fiber length in short fiber carbon/carbon composites by double lap joint”, *Composites: Part B*, 54, p. 365–370, 2013.

[P2] J. Neumayer, P. Kuhn, H. Koerber, and R. Hinterhölzl, “Experimental determination of the tensile and shear behaviour of adhesives under impact loading”, *The Journal of Adhesion*, (in press), 2016.

[P3] J. Neumayer, H. Koerber, and R. Hinterhölzl, “An explicit cohesive element combining cohesive failure of the adhesive and delamination failure in composite bonded joints”, *Composite Structures*, (in press), 2016.

Conferences

[C1] J. Neumayer, R. Hinterhölzl, and K. Drechsler, ”Auslegung und Berechnung von CFK-Klebeverbindungen”, in *13. Workshop des ak-adp: Faserverbundkunststoffe und Plasma-Klebeverbindungen für flexible Oberflächen* , 2012.

[C2] J. Neumayer, H. Koerber, R. Hinterhölzl, and K. Drechsler, ”Auslegung und Berechnung von CFK-Klebeverbindungen”, in *Fakultäts-Seminar “Mobilität” an der TU München* , 2012.

[C3] J. Neumayer, and H. Koerber, ”Determination of a cohesive law in mode I and mode II for a ductile adhesive interface by fracture mechanics and strength tests”, in *International Conference on Experimental Mechanics 16*, 2014.

[C4] J. Neumayer, M. Reil, H. Koerber, and R. Hinterhölzl, ”A combined cohesive zone model for delamination and adhesive failure of a composite bonded joint”, in *World Conference on Computational Mechanics XI*, 2014.

[C5] J. Neumayer, M. Reil, H. Koerber, and R. Hinterhölzl, ”Simulation of bonded joints with laminated adherends for crash applications”, in *Arbeitsgruppe “Engineering” des Carbon Composite e.V.*, 2014.

[C6] J. Neumayer, P. Kuhn, H. Koerber,and R. Hinterhölzl, "Experimental determination of the tensile and shear behaviour of adhesives under impact loading", in *3rd international conference on structural adhesive bonding* , 2015.

B Supervised student theses

During my employment at *Institute for Carbon Composites –Lehrstuhl für Carbon Composites* – I supervised the following student theses:

[S1] B. Fleischmann, ”Finite Elemente Berechnung von laminierten Schalen”, Student thesis, 2012.

[S2] A. Ickes, ”Methodenentwicklung zur Abbildung von interlaminarem Versagen in CFK-Klebstoff-Verbindungen für die FE-Berechnung im Automobilbau”, Diploma thesis, 2012.

[S3] M. Steinhuber, ”Simulation eines Edge Delamination Test”, Diploma thesis, 2012.

[S4] M. Reil, ”Finite Elemente Simulation von Versuchen am Split-Hopkinson-Pressure-Bar zur Charakterisierung von Delaminationen im Schubmodus”, Bachelor thesis, 2012.

[S5] P. Dörner, ”Modeling of Adhesive Material Behavior with Bilinear Cohesive Elements”, Student thesis, 2013.

[S6] F. Kozak, ”Effektive Simulation von CFK-Klebstoffverbindungen”, Diploma thesis, 2013.

[S7] M. M. Schwankl, ”Investigation of Material Health Monitoring Systems for Robust In-Service Use in Composite Structures”, Diploma thesis, 2013.

[S8] T. Yugov, ”Finite Elemente Berechnung von laminierten Strukturen mithilfe von 8-knotigen Kontinuumselementen”, Diploma thesis, 2013.

[S9] M. Wolf, ”Konzeption einer Crashstruktur für Kraftfahrzeugtüren aus carbonfaserverstärktem Kunststoff”, Master thesis, 2013.

[S10] P. M. Huber, ”Neuartige Konzepte zum Rissstopp in Klebungen durch Modifikation der CFK-Oberfläche für das Secondary-Bonding”, Diploma thesis, 2014.

[S11] J. C. Körbelin, ”Implementierung eines viskoelastischen Degradationsmodells zur Beschreibung des Materialverhaltens von Klebstoffen”, Student thesis, 2014.

[S12] M. Reil, ”Implementierung eines kombinierten Kohäsivzonenansatzes für Klebstoff und Delaminationsversagen bei Klebeverbindungen mit laminierten Fügepartnern”, Bachelor thesis, 2015.

[S13] L. A. Seefried, ”Prinzipuntersuchung von CFK/Metall-Mischbaukonzepten für Fahrzeugbodengruppen”, Master thesis, 2015.

[S14] K. Lerch, ”Analyse von Querschubspannungen bei laminierten Strukturen mit Randlasten”, Internal report, 2015.

Parts of the following theses contributed to the underlying doctoral thesis: [S5], [S6], [S11], [S12], [S14]